

# Droplet Production of Biological non-Newtonian Fluids and Bioassay Applications in a Microfluidic Network

by

Merve Marcali

A thesis  
presented to the University of Waterloo  
in fulfillment of the  
thesis requirement for the degree of  
Doctor of Philosophy  
in  
Mechanical and Mechatronics Engineering

Waterloo, Ontario, Canada, 2020

© Merve Marcali 2020

## Examining Committee Membership

The following served on the Examining Committee for this thesis. The decision of the Examining Committee is by majority vote.

External Examiner: Francis Lin  
Professor, Dept. of Physics & Astronomy, University of Manitoba

Supervisor(s): Carolyn Ren  
Professor, Dept. of Mechanical & Mechatronics Engineering  
University of Waterloo

Marc G. Aucoin  
Professor, Dept. of Chemical Engineering, University of Waterloo

Internal Member: Xianguo Li  
Professor, Dept. of Mechanical & Mechatronics Engineering  
University of Waterloo

Internal-External Member: Maud Gorbet  
Professor, Dept. of System Design Engineering, University of Waterloo

Internal-External Member: Roderick Slavcev  
Professor, School of Pharmacy, University of Waterloo

### **Author's Declaration**

I hereby declare that I am the sole author of this thesis. This is a true copy of the thesis, including any required final revisions, as accepted by my examiners.

I understand that my thesis may be made electronically available to the public.

## Abstract

Droplet-based microfluidics has been developed over the last two decades and presented as a promising platform for biochemical assay. This promise relies on the system's ability to quantify the reagents accurately with high throughput. In addition, since each droplet act as a micro-reactor, faster reaction time and reduced reagent consumption can be achieved. Most of these biochemical assays require biological samples to be handled, which is non-Newtonian in nature. However, there is little information on droplet formation dynamics of biological non-Newtonian fluids. Therefore, this thesis investigates the formation dynamics of the droplet of red blood cells as a non-Newtonian fluid. Then, a bio-assay to quantify the viruses in red blood cell solution is developed by using droplet based microfluidic system to show the system's sensitivity and precision.

The first part of the thesis focuses on the droplet formation of biological non-Newtonian fluids in a T-junction generator under the squeezing regime. In this regime, droplet formation with Newtonian fluids depends on T-junction geometry; however, the formation depends on the aspect ratio and width ratio of the channel, the flow rate ratio of fluids, and the viscosity ratio of the phases in the presence of the shear-thinning biological non-Newtonian fluids such as red blood cells. In addition, we analyze the impact of the red blood cell concentration on the formation cycle. In the first part, we presented the experimental data of the red blood cell droplet evolution through the analysis of high-speed videos. During this analysis, we tracked several operational parameters such as droplet volume, the spacing between droplets, generation frequency by varying the flow conditions of fluids, and the geometrical designs of the T-junction. Our analysis reveals that unlike other non-Newtonian fluids, where the fourth stage exists (stretching stage), the formation cycle consists of only three stages: lag, filling and necking stages. Based on the detailed analysis of each stage, a mathematical model is developed to predict the final volume of the red blood cell droplets in the second part, which can be utilized in sensitive biochemical assay applications for future studies.

In the second part, we analyzed the three stages of single cycle of the droplet formation and developed a mathematical model that describes the performance of the T-junction generators for biological non-Newtonian fluids (i.e., red blood cells - (RBCs)). The model integrated with a detailed analysis of the geometrical shape of the droplet during the formation process and combined with analysis of a force balance and a Laplace pressure balance to define the penetration depth and the critical neck thickness of the droplet. This analysis captures the influence of the governing dimensionless parameters (i.e., channel width and height, flow rate ratios, and fluid viscosities). The performance of the model was validated by comparing the operational parameters (droplet volume, the spacing between

the droplets and the generation frequency) with the experimental data across the range of these dimensionless parameters. The model matches well with the experimental results as data falls within 20% of the predicted values of the droplet volume.

The third part of this study focuses on the development of the biochemical assay using a droplet-based microfluidic system. This study presents Influenza A virus/virus-like particles (VLPs) quantification by running hemagglutination assay (HA Assay) in a droplet-based microfluidic system. VLPs are genetically engineered non-infectious particles, which have proteins to mimic the original virus but lack of genetic material to infect host organisms. Therefore, VLPs are good candidates for vaccine production. To determine the final dosage of VLPs in the vaccine, HA assay is done using 96-well plates. In this assay, diluted particles mixed with the target RBCs and the aggregation takes 4 hours to finalize. Although this method is a common procedure, longer reaction time, cross-contamination and human errors are the major drawbacks of this system. To eliminate these disadvantages, a droplet-based HA assay was developed. In this study, it was shown that the reaction time dropped to 4-10 seconds due to small diffusion length in droplets, the cross-contamination was prevented due to the compartmentalization nature of droplets, and the aggregation reaction was detected by the image analysis to eliminate human error.

## Acknowledgements

First and foremost, I would like to express my gratitude to my advisors, Dr. Carolyn Ren and Dr. Marc G. Aucoin for their support, patience, and encouragement. With their guidance, I improve my critical discussion skills, an academic knowledge, and become a capable researcher.

I owe a gratitude to my committee members Dr. Francis Lin, Dr. Maud Gorbet, Dr. Roderick Slavcec and Dr. Xianguo Li for improving my thesis with their invaluable feed-backs.

I would like to thank lab mates Megan Logan, Scott Joseph Boegel, Dr. Emma Dare, Matt Courtney, Weijia Cui, Dr. Pei Zhao, Dr. Xiaoming Chen and Dr. Anna Thu Nyugen who make suggestions during my presentations in group meetings. I would like to specifically thank to my other lab members Mark Bruder, Madhuja Chakraborty, Eduardo Ramirez who help me to prepare biological samples for the quantification assay project.

I am greatly thankful for the support of my dearest friends who are far away but at the same time so close to me Ercan Savci, Ozan Celik, and Meltem Erdem. It is their endless friendship, moral support and inspirational advice that I will never ever forget throughout my life. I am so lucky to have you in my life.

I extend my deepest heartfelt thanks to my little family members Burak Tekcan and Toros and my parents Esin and Mehmet Marcali, my brother Berke as well as Burak's parents Rukiye and Cemalettin Tekcan, and my brother-in-law Goktug for their faithful support and confidence in me. I would always be indebted to them.

Funding for this research was provided in part by the Natural Sciences and Engineering Research Council of Canada (NSERC).

# Table of Contents

List of Figures	xi
List of Tables	xxiii
Nomenclature	xxiv
List of Symbols	xxvi
<b>1 Introduction</b>	<b>1</b>
1.1 Research Background . . . . .	1
1.2 Thesis Outline . . . . .	2
<b>2 Literature Review</b>	<b>4</b>
2.1 Fundamentals of Droplet-Based Microfluidics . . . . .	4
2.1.1 Forces and Dimensionless Numbers . . . . .	4
2.1.2 Effect of Fluid Properties . . . . .	6
2.2 Droplet Generation Regimes and Methods . . . . .	9
2.2.1 Generation Regimes . . . . .	10
2.2.2 Generation Methods - Passive Methods . . . . .	12
2.2.3 Generation Methods - Active Methods . . . . .	14
2.2.4 Comparison of Droplet Generators . . . . .	15
2.3 Droplet Motion in a Microfluidic Channel . . . . .	16

2.3.1	Fluid Motion in a Droplet . . . . .	16
2.3.2	Hydrodynamic Resistance of Droplets in Microchannel (Pressure Drop)	16
2.3.3	Droplet Velocity in Microchannel . . . . .	19
2.4	Passive Manipulation of Droplets in Microchannels . . . . .	21
2.4.1	Mixing in Droplets . . . . .	22
2.4.2	Splitting of Droplets . . . . .	22
2.4.3	Coalescence/Merging of Droplets . . . . .	22
2.4.4	Sorting of Droplets . . . . .	23
2.5	Characteristics of Blood Cells . . . . .	25
2.5.1	Components of Blood . . . . .	25
2.5.2	Red Blood Cell Morphology . . . . .	26
2.6	Influenza A Virus and Virus-Like Particles . . . . .	26
2.6.1	Influenza A Virus . . . . .	26
2.6.2	Influenza A Virus Vaccine . . . . .	27
2.6.3	Virus-Like Particle (VLP) . . . . .	29
2.7	Virus Quantification Methods . . . . .	29
2.7.1	Antibody Dependant Methods . . . . .	30
2.7.2	Antibody Independent Methods . . . . .	31
2.7.3	Infectivity Measurement . . . . .	33
<b>3</b>	<b>Material and Methods</b>	<b>35</b>
3.1	Microfluidic Chip Fabrication . . . . .	35
3.2	Experimental Setup of the Microfluidic System . . . . .	38
<b>4</b>	<b>Experimental Analysis of Droplet Formation of Red Blood Cells in a T-junction</b>	<b>40</b>
4.1	Overview of Previous Works . . . . .	40
4.2	Introduction and Objective of the Project . . . . .	44



4.3	Design of Experiment . . . . .	45
4.3.1	Material And Methods . . . . .	45
4.3.2	Experimental Setup . . . . .	49
4.3.3	Experimental Procedure . . . . .	50
4.3.4	Video Analysis . . . . .	51
4.4	Results and Discussions . . . . .	53
4.4.1	Dynamics of Red Blood Cell Droplet Formation . . . . .	53
4.4.2	Scaling of Operational Parameters . . . . .	61
4.5	Conclusion . . . . .	62
<b>5</b>	<b>Mathematical Modeling of Droplet Formation of Red Blood Cells in a T-junction</b>	<b>66</b>
5.1	Introduction and Objective of the Project . . . . .	66
5.1.1	Lag Stage . . . . .	68
5.1.2	Filling Stage . . . . .	69
5.1.3	Necking Stage . . . . .	71
5.1.4	Calculation of $b_{fill}^*$ and $2r_{pinch}^*$ . . . . .	75
5.1.5	Validation of the Mathematical Model . . . . .	78
5.2	Conclusion . . . . .	83
<b>6</b>	<b>Development of Hemagglutination Assay in Microdroplets to Quantify Influenza Virus</b>	<b>85</b>
6.1	Overview of Previous Works . . . . .	85
6.2	Introduction and Objective of the Project . . . . .	87
6.3	Design of Experiment . . . . .	88
6.3.1	Materials and Methods . . . . .	88
6.3.2	Experimental Setup . . . . .	91
6.3.3	Experimental Procedure . . . . .	91
6.3.4	Image Analysis . . . . .	92

6.4	Results and Discussions . . . . .	93
6.4.1	Effect of Red Blood Cell Concentration on Reaction . . . . .	95
6.4.2	Effect of Mixing Ratio on Reaction . . . . .	96
6.4.3	Effect of Droplet Size on Reaction . . . . .	97
6.4.4	Effect of Red Blood Cell Freshness on Reaction . . . . .	98
6.4.5	Effect of Type of Virus-Like Particle Stock on Reaction . . . . .	99
6.4.6	Performance of the Quantification System . . . . .	103
6.5	Conclusion . . . . .	104
<b>7</b>	<b>Contributions to the Field and Recommendation for Future Studies</b>	<b>105</b>
7.1	Contributions to the Field . . . . .	105
7.2	Recommendations for Future Work . . . . .	106
	<b>References</b>	<b>108</b>
	<b>APPENDICES</b>	<b>121</b>
<b>A</b>	<b>Image and Video Analysis Codes</b>	<b>122</b>
A.1	Extraction of Frames from Videos - Matlab Code . . . . .	122
A.2	Converting Gray Scale Image into Binary Image - Matlab Code . . . . .	122
A.3	Channel Height Calculation - Matlab Code . . . . .	123
	<b>APPENDICES</b>	<b>124</b>
<b>B</b>	<b>Fluid Property Measurements</b>	<b>125</b>
B.1	Flow Sensor Calibration for Oil Viscosity Measurements . . . . .	125
B.2	Viscosity Measurements of Red Blood Cells . . . . .	125
B.3	Interfacial Tension Measurement of Fluids . . . . .	126

# List of Figures

2.1	Schematic of the molecular transport of the surfactant molecules to the interface of two fluids. On the left, oil droplets are encapsulated in the water phase. Head parts of the surfactant molecules face outward and on the right, water droplets are encapsulated in the oil phase. Head and tail parts of the surfactant molecules align corresponding to the material of the phase [88]. . . . .	8
2.2	Schematic of the contact angle of a droplet on a solid surface with three surface tension values at equilibrium wetting condition. $\theta_{eq}$ is the contact angle, $\gamma_{sl}$ is the solid-liquid interfacial tension, $\gamma_{sg}$ is the solid-gas interfacial tension, and $\gamma_{lg}$ is the liquid-gas interfacial tension. . . . .	8
2.3	List of microfluidic droplet generators a) passive droplet generation methods that include i) flow focusing, ii) cross-flow, iii) co-flow designs b) active droplet generation methods that include iv) external forces and v) internal forces. . . . .	10
2.4	Microscopic images of five droplet generation regimes in the three major droplet generator designs. Droplets can be generated in all regimes in co-flow and flow-focusing designs (left and right images, respectively). However, tip-streaming and tip-multi breaking regimes cannot be achieved in cross-flow design (middle image) [14]. . . . .	12
2.5	Schematic of passive microfluidic droplet generators: a) co-flowing, b) cross-flowing and c) flow focusing [16]. . . . .	15

2.6	Schematic of the vortices in the droplet and the continuous phase for two different cases ( $(\eta_d) \ll (\eta_\varphi)$ or $(\eta_d) \gg (\eta_\varphi)$ ). The top figure indicates the case where the viscosity of the carrier oil is much larger than the fluid viscosity in the droplets. The bottom figure illustrates the case where the viscosity of the continuous phase is lower than the fluid viscosity in the droplets. In the latter case, the number of vortices is higher than the former case in droplets [32]. . . . .	17
2.7	a) The sketch illustrates the curvature of both ends of the droplets and the pressure drop along a microchannel b) Cross-section view of the droplet showing the lubrication layer (thin film) and the gutter region (the gaps between the droplet and four channel corners), which makes the droplet resistance complex c) A schematic diagram illustrates no flow of the lubrication layer is present d) A schematic diagram showing the lubrication layer bypasses the droplet [32]. . . . .	18
2.8	Schematics of the pressure drop along a microchannel containing a droplet train. In the case of (a) where inviscid droplets ( $\eta \ll 1$ ) were generated, pressure remains constant along the body part of the droplet. However in the case (b) where viscous droplets ( $\eta \sim 1$ ) were generated, pressure drops along the body part of the droplet [8]. . . . .	19
2.9	a) Schematic of isolated droplets where droplets do not confine the channel and float. b) Schematic of slug/plug like droplets that confine the channel cross-section. c) Schematic of lubrication layer/oil phase between the isolated droplets and the channel walls. d) Schematic of the lubrication layer with the gutter formation between the edges of the rectangular channel and the slug/plug like droplet. The gutter region causes back flow of the oil phase to the opposite direction of droplet flow which changes the entire flow field in the microfluidic channel [8]. . . . .	20
2.10	The top figure illustrates the mixing in droplets. Vortices in the droplets changes as the angle of the serpentine channel changes. Smooth turns (i) maintain the symmetry in the vortices and cause slow mixing. However, sharp turns (ii) break the symmetry and lead to faster mixing. The bottom figure is the microscope image of mixing of two different food dyes in droplets [12]. . . . .	23

2.11	A microscope image of droplet splitting using a bifurcation design in the channel. A larger droplet came to the T-junction at the top of the figure and was split into two daughter droplets. Then, these two droplets were split into four at the second T-junction. This procedure continued until the last T-junction in the design [63]. . . . .	24
2.12	Microscope images of two different passive droplet coalescence/merging methods a) droplets merged at the exit of the expanded part of the channel b) the previously formed droplet was held by the pillars, and the following droplet merged with the previous droplet [10]. . . . .	24
2.13	Passive sorting of droplets. a) Schematic of overall microfluidic channel design for droplet separation. b) Microscope image showing the separation of the larger droplets from the small droplets c) Enlarged view of the separation channel [71]. . . . .	25
2.14	Schematic of Influenza A Virus. The virus contains Hemagglutinin (HA) and Neuraminidase (NA) proteins at the surface, RNA at the core and Matrix Proteins at the interface. . . . .	27
2.15	Schematic of Influenza virus infection cycle in the a host cell. The cycle starts with attachment of the Influenza virus with the sialic acid receptors of the host cell. Once the attachment is complete, the virus enters into the cell with endocytosis. Then, the virus release its RNA. The released RNA enters into the nucleus of the host cell to start replication of itself. Then, the surface proteins of the virus and the viral RNA are exported to the cell membrane to form a new virus. Finally, the new virus emerges from the host cell. . . . .	28
2.16	Schematic of Influenza A Virus (Left) and Influenza Virus-Like Particle (Right). The fundamental difference between Influenza virus and Influenza VLP is that the VLP does not contain RNA. . . . .	29
2.17	List of Influenza virus quantification methods. The quantification methods are categorized under three main branches, which are antibody dependent methods, antibody independent methods and measures of measures of infectivity. . . . .	30
2.18	Schematic of hemagglutination reaction in 96-well plate. The top row indicates no reaction where the red blood cells precipitates at the bottom of the well in the absence of the virus. The bottom row shows that reaction occurs, where the viruses attach to the red blood cells and form a lattice. This results in a homogeneous color in the well [30]. . . . .	32

2.19	Photograph of the hemagglutination reaction in 96-well plate for various red blood cell (RBC) concentrations. The concentration of the 10% washed RBCs were diluted by phosphate buffer saline (PBS, 1X, pH=7.4). The cell concentration was adjusted to 10% in the top two rows, 5% in the 3rd and 4th rows, 2% for the 5th and 6th rows and 1% in the bottom two rows. . .	32
3.1	Schematics of photo-lithography steps for transferring CAD design (desired microfluidic device design) onto the silicon wafer. a) Spinning of the 1st photoresist, b) Soft-baking the photoresist, c) UV exposure (without a mask) to harden the photoresist, d) Post-baking the photoresist, e) Spinning a second layer of photoresist, f) Soft-baking step for the second resist, g) UV exposure with the mask to transfer microfluidic chip pattern, h) Post-baking for the second photoresist, i) Development of the exposed photoresist pattern, j) The final pattern transferred onto the Si wafer. . . . .	37
3.2	Schematic of PDMS casting steps and bonding. a) Developed photoresist on the silicon wafer, b) PDMS was poured on the silicon wafer and baked to cure the polymer, c) The cured PDMS was peeled off of the silicon wafer, d) The detached PDMS was punched from the inlets and outlets, e) A glass substrate and PDMS were exposed to oxygen plasma to activate the surfaces for bonding f) PDMS was bonded onto the glass slide. . . . .	38
3.3	Experimental setup. Fluids were pumped into the microfluidic device using the pressure pump system (top left). The pressure pump creates air pressure that pumps the desired fluids from the reservoir (bottom left) to the microfluidic chip. A flow sensor is connected in between the reservoir and the microfluidic chip to measure the flow rate of fluids. The flow is recorded using a high speed camera or a CCD camera. Images were acquired using the microscope (right). . . . .	39
4.1	Microscope image of the generated droplets of red blood cells in a T-junction generator. Parameters affecting the droplet formation: $P_c$ , $Q_c$ , $w_c$ are the continuous phase pressure, flow rate, and channel width, respectively. $P_d$ , $Q_d$ , $w_d$ are the dispersed phase pressure, flow rate, and channel width, respectively. $L_d$ is the length of the droplet, $L_c$ is the length of the oil phase between droplets, $u_d$ is the droplet speed, $V_d$ is the droplet volume, $\lambda$ is the spacing length between the droplets. $Q_m$ and $w_m$ are the main channel flow rate and channel width, respectively. . . . .	42

4.2	Schematic of the overall microfluidic device design. The design consists of one dispersed phase, one continuous phase and a main channel. To generate droplets, a T-junction generator was used. At the junction, we used two dispersed phase channel widths. The left side of the enlarged figure represents a wider dispersed phase channel width, and the right side of the enlarged figure represents a narrow dispersed phase channel width. . . . .	48
4.3	Schematic of the equivalent electrical circuit of the microfluidic chip design. The circuit was utilized to calculate the hydrodynamics resistances of the channels and the channel height. In this case, the dispersed phase channel was plugged to prevent incoming flow into the channel. Then, silicone oil was flushed into the device from the continuous phase through the outlet, and flow rate of the silicone oil was measured using a flow sensor. Finally, hydrodynamic resistances of the two serially connected channels ( $R_c$ and $R_m$ ) were calculated using the flow rate data and Equations 4.10, 4.12 which also give channel height information. . . . .	50
4.4	Sequence of image processing for a single droplet image. First, a video of the droplet formation was recorded using a high-speed camera. Then, each frame of the recorded video was cropped to be analyzed. The cropped images were filtered to eliminate noise using median and Weiner filters. The filtered images were sharpened to highlight the boundary of the droplets. Then, the sharpened images were converted into binary images (Black and white image). The edge of the droplet was defined by using edge detection function to differentiate the droplet from the dispersed phase and enclosed object (droplet) was labelled with white color. Finally, the droplets were labelled in different colors to eliminate double processing in case two droplets are captured in a single frame. By doing this only the droplet closer to the junction was analyzed. . . . .	52
4.5	Microscopic images of a single formation cycle of red blood cells droplets in a T-junction generator under the squeezing regime. The cycle consists of three stages: lag, filling and necking stages. After these three stages, a detachment of the droplet occurs. . . . .	54

4.6	High-speed camera images of an individual droplet formation cycle for six different cases. Droplet formation with non-Newtonian fluid (red blood cell solution) consists of three stages: lag, filling, and necking stages. Each case was differentiated from case A in terms of channel dimensions and fluid properties (detailed parameters of each case were given under each figure). Droplet volume, spacing between droplets and generation frequency were different in each case showing the impact of the listed parameters on a formation cycle. . . . .	55
4.7	a) Schematic of the critical points of the three stages of a droplet formation cycle in the T-junction with analyzed dimensionless variables ( $L_{lag}$ , $b_{fill}$ , $b_{pinch}$ , $V_{fill}$ , $2r_n$ , $2r_{pinch}$ ), and b) Evolution of droplets with respect to time for six representative cases and the dynamic changes of the dimensionless variables (Droplet volume ( $V_d^*$ , circle), penetration depth ( $b_{fill}^*$ , square), and neck thickness ( $2r_n^*$ , triangle)) over time. . . . .	57
4.8	Bar plot of the duration of the lag stage for all experimental cases. Duration of lag stage was governed by the width ratio ( $\wedge$ ) of the channels and other dimensionless parameters ( $h^*$ and $\eta$ ) became less effective. As the width ratio decreased ( $\wedge= 1$ to $0.5$ ), the lag duration increased due to the receding of the dispersed phase into the channel. . . . .	58
4.9	Bar plot of the duration of the filling stage for all experimental cases. Duration of the filling stage was mostly governed by the width ratio ( $\wedge$ ) of the channels and other dimensionless parameters ( $h^*$ and $\eta$ ) had limited impact on the duration. As the width ratio was decreased, the duration of the filling stage increased. However, as the oil viscosity or the aspect ratio was decreased, the duration of this stage decreased. . . . .	59
4.10	Bar plot of the duration of the necking stage for all experimental cases. Duration of this stage was only governed by the oil viscosity (or the viscosity ratio of fluids: $\eta$ ) and as the oil viscosity was reduced, the necking duration was shorten due to the shear thinning property of the red blood cells. Other dimensionless parameters ( $h^*$ , $\wedge$ ) had no impact on the duration of this stage.	60



4.11	Bar plots showing the dependence of the four dimensionless variables ( $b_{fill}^*$ , $V_{fill}^*$ , $2r_{pinch}^*$ , $t_{total}^*$ ) to the dimensionless parameters ( $h^*$ , $\Lambda$ , $\eta$ ) for twelve cases a) Dimensionless penetration depth ( $b_{fill}^*$ ) at the end of the filling stage was dependent only to the aspect ratio ( $h^*$ ) b) Similar to the penetration depth, dimensionless droplet volume at the end of the filling stage ( $V_{fill}^*$ ) was dependent to the aspect ratio ( $h^*$ ) c) Dimensionless neck thickness right before the pinch-off point ( $2r_{pinch}^*$ ) was dependent only to the aspect ratio ( $h^*$ ) d) Dimensionless total duration of a droplet formation cycle ( $t_{total}^*$ ) was dependent to all dimensionless parameters ( $h^*$ , $\Lambda$ , $\eta$ ). . . . .	62
4.12	Scaling analysis of the dimensionless operational parameters (final droplet volume ( $V_d^*$ ), spacing between droplets ( $\lambda$ ) and droplet generation frequency ( $f^*$ )) over a range of flow rate ratios ( $\varphi$ ) for six representative cases, a) Dimensionless final droplet volumes over flow rate ratios. Final droplet volumes were linearly proportional to the flow rate ratios for all cases, b) Dimensionless generation frequencies over flow rate ratios. The data exhibit a non-linear trend with respect to the flow rate ratios, c) Dimensionless spacing between droplets over flow rate ratios. Spacing between droplets were inversely proportional to the flow rate ratio. . . . .	63
5.1	Schematic of a 2-D view of the characteristic shape of the droplet a) Top view b) Cross-section view. Channel width of the dispersed phase is indicated as $w_d$ , channel width of the continuous phase $w_c$ , $h$ is the channel height, $2r_n$ is the neck thickness of the emerging droplet, $R_n$ is the radius of the back half of the droplet, $b$ is the penetration depth (or the radius of the front half of the droplet), and $w_{gap}$ is the gap between the droplet and the far channel wall where silicone oil bypasses. . . . .	69
5.2	Schematic of the droplet interface during the lag stage (top figure). Microscopic images of red blood cell droplets before and after the detachment for two different channel width ratios (bottom image). For the designs where width ratio ( $\Lambda=1$ ), no receding of the interface was observed, and the interface stayed right at the junction entrance after the previous droplet detached as indicated with the black dashed lines. However, in case width ratio ( $\Lambda=0.5$ ), the dispersed phase receded back and the lag distance ( $L_{lag}$ ) became observable. . . . .	70

5.3	Schematic of 2D-shape of the droplet at the end of the filling stage for two cases a) For cases $w_d \leq b_{fill}$ , the back half of the droplet is a quarter-circle with a diameter equal to $b_{fill}$ and the radius of the front half of the droplet also is $b_{fill}$ b) For cases $w_d > b_{fill}$ , the back half of the droplet is not equal to a quarter circle and the radius of the circular segment equals to the dispersed phase channel width ( $w_d$ ). Therefore, the volume contribution of this stage to the final droplet volume is calculated by utilizing these two different geometrical shapes. . . . .	72
5.4	Schematic of 2D-shapes of the droplets at the end of the filling and necking stages. The subtraction of the two geometrical shapes (b-a) help to calculate the volume contributions of the oil phase to the droplet pinch-off a) Left top image indicates the end of the filling stage. Red area represents the control volume of the oil phase ( $V_{c_{fill}}^*$ ) that contributes to necking of the droplet. Bottom left figure illustrates a detailed view of the control volume which is the sum of two distinct geometrical regions (red and purple areas) b) Right top image indicates the end of the necking stage. Red area represents the control volume of the oil phase ( $V_{c_{pinch}}^*$ ) that contributes to necking of the droplet. Bottom right figure represents the detailed view of the control volume that was the sum of two geometrical shapes (red and purple areas). . . . .	73
5.5	a) Sequence of microscopic images of the droplet collapsing during the necking stage. At the beginning of the necking stage, the back half of the droplet had a quarter circle shape. Then, as the droplet elongated due to the shear thinning property of the red blood cells and the pinning of the continuous phase at a distance $w_d$ , a quarter-circle converted to a circular-segment and red dashed area changed over time. The volume change in the red dashed area contributed to the collapsing rate of the droplet b) To analyze the volume change, geometrical relations between variables were constructed. The schematic represents the geometrical shape and the required variables to calculate the volume of the oil phase at this stage. Elongation length was indicated as $a$ , $d$ was the distance from the pinning point to the farthest penetration distance of the droplet. . . . .	76
5.6	Comparison of experimentally measured penetration depth with the theoretical penetration depth using Equation 5.18. a) The experimental data of six cases under different capillary numbers were fitted to the model developed during the force balance analysis. b) Parity plot of the penetration depth for all cases under the same flow rate ratio ( $\varphi \sim 0.04$ ). The solid line represents the perfect parity, and the dashed lines are $\pm 10\%$ . . . . .	79

5.7	Parity plot of the critical neck thickness for all experiments under the flow rate ratio: $\varphi \sim 0.04$ . The experimental neck thickness data fell within $\pm 15\%$ of the theoretical neck thickness data using Equation 5.7. . . . .	80
5.8	Parity plots for model validation for three major dimensionless operational parameters (final droplet volume ( $V_d^*$ ), droplet generation frequency ( $f^*$ ), spacing between droplets ( $\lambda^*$ ) a) Experimental droplet volume data fell within $\pm 20\%$ of the calculated data b) Experimental droplet generation frequency data fell within $\pm 15\%$ of the expected values c) Experimental data of the spacing between droplets fell within $\pm 25\%$ of the expected values.	82
6.1	a) Schematic of the microfluidic device design. From point A, the virus stock was applied to the system. From point B, the red blood cell solution was applied. Silicone oil was used as a continuous phase (Point C). Droplets were generated at the T-junction (Point Y). Reagents in the droplets were mixed in the serpentine channels and the reaction was recorded from point Y through the end of the last serpentine channel. b) Equivalent electrical circuit of the microfluidic channel. The circuit analysis was done to design the microfluidic device robust enough to eliminate droplet size variations during formation and to achieve sufficient mixing in droplets. . . . .	90
6.2	Images of the experimental setup and the microfluidic chip (on the left). Image of the microfluidic chip after the experiment was completed, see generated droplets inside the tubing that was connected to the outlet of the channel (on the right). . . . .	92
6.3	Illustration of the image analysis sequence and microscope images of droplets from different locations of the microfluidic channel. Videos of the droplet formation and reaction were recorded. Then each frame was extracted from the videos to be analyzed. Four regions of interests (ROI: 7s, 26s, 43s, 77s - red dashed rectangles) were selected. Then, the droplets passing those regions were analyzed by converting the images into binary images (black and white) to count the agglutinated red blood cells (clumps). The area of black region in the droplets indicated the agglutinated red blood cells. By measuring the clump size change over time in droplets passing through ROI, the end of the reaction was determined. Then, the reaction time was calculated. . . . .	93

6.4	Schematic of the microfluidic device and microscope images of droplets in certain sections of the channel a) Two-phases flew in parallel through the Y-junction and droplets were generated at the T-junction (blue dashed rectangle) b, c) Mixing of reagents started at the dense turns and the reaction in droplet was complete as the agglutinated red blood cells (clumps) were formed in the mixing region (yellow and orange rectangles). . . . .	94
6.5	Agglutinated red blood cells (RBC) size ( $\mu\text{m}$ ) measurement in droplets over time. The red line indicates the presence of agglutination in droplets (undiluted stock of known HA activity) in one chip (Chip 1); the blue line represents no reaction in droplets ( $12^{\text{th}}$ dilution of stock of known HA activity) in another chip (Chip 2). The applied pressures were the same ( $P_{oil}=300$ mBar, $P_{RBC}=290$ mBar, $P_{HA}=290$ mBar) for both experiments. $N=20$ droplets were recorded for each chip (Chip 1 and 2) in a single run. . . . .	95
6.6	Effect of RBC concentration on hemagglutination reaction in microdroplets. The red line shows non-diluted red blood cell concentration in Chip 3, the blue line shows 50% RBC concentration in Chip 4, and the green line shows 10% RBC concentration in Chip 5. Flow conditions were kept the same for all three experiments ( $P_{oil}=300$ mBar, $P_{RBC}=290$ mBar, $P_{HA}=290$ mBar. Reaction ended after 43 s for lower concentrations of RBCs due to the excess virus stock per cell. However, the reaction ended after 60 s in undiluted RBC sample. Right graph represents the system linearity of a quantification assay where $R^2=0.94$ . $N=20$ droplets were recorded for each chip (Chip 3, 4 and 5) in a single run. . . . .	96
6.7	Photograph of hemagglutination reaction in 96-well plate for various RBC concentrations (from 1% to 10%). Reaction became undetectable in higher RBC concentration by naked-eye in 96-well plate. . . . .	97
6.8	Effect of different mixing ratio of the reagents on the reaction. The flow conditions were kept the same for all experiments ( $P_{oil}=300$ mBar, $P_{RBC}=290$ mBar, $P_{HA}=290$ mBar and droplets were generated in similar sizes). Blue line indicates the larger virus fraction sample where the reaction ended after 32 s (Chip 1) and red line indicates the droplet encapsulated the equal volume of reagents where the reaction ended after 60 s (Chip 6). $N=20$ droplets were recorded for each chip (Chip 1 and 6) in a single run. . . . .	98

6.9	The effect of droplet size on the reaction. The red line represents the larger droplet ( $P_{oil}=300$ mBar and $P_{HA}, P_{RBC}=290$ mBar) - Chip 7. The blue line represents the smaller droplet ( $P_{oil}= 310$ mBar $P_{RBC}, P_{HA}= 290$ mBar) - Chip 8. Reaction ended in a similar time for both cases. However, a smaller clump size was measured in small droplets due to number of cells encapsulated in droplets.N=20 droplets were recorded for each chip (Chip 7 and 8) in a single run. . . . .	99
6.10	Effect of red blood cell freshness on the reaction. Green-red lines indicate the fresh red blood cell samples (1st day of red blood cell collection - Chip 9 and 10) in different droplet sizes. Blue-purple lines indicate the non-fresh red blood cell sample (6th day of the red blood cell collection - Chip 10 and 11) in different sizes of droplets. Reaction ended in 60 s for all cases but the clumps size was bigger in fresh samples.N=20 droplets were recorded for each chip (Chip 9, 10, 11 and 12) in a single run. ( $P_{oil}=300$ mBar and $P_{HA}, P_{RBC}=290$ mBar). . . . .	100
6.11	HA activity of the three different preparations with 3 replicates in 96-well plates. Three different VLPs were analyzed. Asterisk (**) indicates freshly prepared material, while the HA-NA-M1 VLP was prepared eight months earlier and stored at 4° C. GAG-GFP-HA was another construct of the Virus Like Particle. Highest HA activity was measured in freshly prepared HA-NA-M1** virus stock. . . . .	101
6.12	Effect of virus type on the reaction for two different droplet sizes for each virus type. Red-green-blue lines represent the larger droplets, while yellow-light blue-purple represent smaller droplets. Reaction was similar in all types and highest HA activity was observed in the freshly prepared HA-NA-M1** virus stock similar to the 96-well plate results. N=20 droplets were recorded for each chip (Chip 13-red line, 14-green line, 15-blue line, 16-purple line, 17-light-blue line, 18-yellow line) in a single run. were used for each virus preparations to prevent cross-contamination. ( $P_{oil}=300$ mBar and $P_{HA}, P_{RBC}=290$ mBar, for larger droplets), ( $P_{oil}= 310$ mBar $P_{RBC}, P_{HA}= 290$ mBar, for smaller droplets). . . . .	102

6.13	Comparison of the standard HA assay with the microfluidic system in terms of the limit of the detection. Top figure represents the HA assay in 96-well plate of a given virus stock (HA-NA-M1**). Agglutination reaction ended at the 8 <sup>th</sup> (Chip 19) dilution of the sample. However, when the same samples were transferred into the microfluidic chip, the reaction was still observable at the 11 <sup>th</sup> (Chip 22) dilution of the virus stock which proves the greater sensitivity of the droplet based microfluidic system over the standard assay.	103
B.1	Calibration curves of the flow sensor for three different silicone oil viscosities.	126
B.2	Viscosity measurements of the chicken red blood cells for various cell concentrations under the range of shear rate from 1-3000 1/s in the microfluidic channels (cross, 100% RBC), (parallelogram, 45% RBC), (cube, 30% RBC), (triangle, 20% RBC), (circle, 10% RBC), (plus, Plasma) [29]. . . . .	127

# List of Tables

2.1	Dimensionless numbers in a two-phase microflow, which are scaled to the characteristic length. All the dimensionless numbers have a dependence on the characteristic length (L), whereas the capillary number is independent of L, which makes it the governing dimensionless number when the flow is analyzed in micro-scale. . . . .	6
4.1	List of conditions for each experimental case study. Overall there were 13 different experiments. Among these experiments, only diluted red blood cell sample (45% RBCs) were tested using one silicone oil type (100 mPa.s) and one geometrical design ( $h^*=0.6$ , $\Lambda=1$ ) (see experiment number 13) . . . . .	46
4.2	Physical properties of the dispersed and continuous phases. Viscosity of the red blood cells was adopted from the literature for both cell concentration values [29], [26]. The interfacial tension of red blood cells with the silicone oil was measured using a Wilhemy plate tensiometer (Data Physics, DCAT 11, Germany). . . . .	46
B.1	Physical properties of the dispersed and the continuous phases. . . . .	126

# Nomenclature

**1D** one dimensional, two dimensional, three dimensional [64](#), [83](#)

**BEVS** Baculovirus Expression System [34](#)

**Ca** Capillary Number [34](#)

**DLS** Dynamic light scattering [104](#)

**DNA** Deoxyribonucleic acid [34](#)

**EDTA** Ethylenediaminetetraacetic acid [64](#), [83](#), [104](#)

**ELISA** Enzyme-linked immune sorbent assay [104](#)

**ETFE** Ethylene tetrafluoroethylene [34](#)

**FDA** Food and Drug Administration [34](#)

**GFP RFP** Green and red fluorescent proteins [104](#)

**HA** Hemagglutinin [3](#), [34](#)

**HA assay** Hemagglutination Assay [3](#)

**HAU** Hemagglutination unit [104](#)

**Hct** Hematocrit Level [34](#)

**HPV** Human papillomavirus [34](#)



**LC-MS** Liquid chromatography-mass spectrometer 104

**MOI** Multiplicity of infection 104

**NA** Neuraminidase enzyme of the Influenza Virus 34

**NP** Nucleoprotein of the influenza virus 34

**NS1** Nonstructural proteins of the influenza virus 34

**PB1** Polymerase subunits of the influenza virus 34

**PBS** Phosphate buffer saline 64, 83, 104

**PDMS** Polydimethylsiloxane 34

**PE** Peclet number 104

**PEO** Polyethylene oxide 64, 83

**Re** Reynolds number 34

**RNA** Ribonucleic acid 34

**RP-HPLC** Reversed-phase high-performance liquid chromatography 104

**Sf9** Spodoptera frugiperda cell 104

**SRID** Single radial immunodiffusion assay 104

**TEM** Transmission electron microscopy 104

**UV** Ultraviolet 34

**VLP** Virus Like Particle 3, 34

# List of Symbols

$2r_n$  Neck thickness of the droplet 65, 84

$V_d$  Droplet Volume 64, 83

$A_{gap}^*$  Dimensionless area of the bypass around the droplet 65, 84

$\alpha, \beta$  Fitting parameters 65, 84

$\alpha_{lag}, \alpha_{fill}$  droplet volume at lag and filling stage respectively 65, 84

$h^*$  Aspect ratio of phases 64, 83

$a^*$  Dimensionless elongation length of the droplet 65, 84

$b_{ave}^*$  Dimensionless average penetration depth 65, 84

$b_{fill}$  Penetration depth at the end of the filling stage 64, 84

$b_{pinch}$  Penetration depth at the end of the necking stage 65, 84

$b^*$  Dimensionless penetration depth 64, 83

$C_{cell}$  Red blood cell concentration 64, 83

$L$  Characteristic length 34

$\rho(u\nabla)u$  Convective acceleration term 34

$\partial u/\partial t$  the partial derivative of velocity with respect to the time 34

$\rho$  Fluid density 34

$Q_{drop}$  Flow rate of the droplet 64, 83

$n$  Number of droplets 64, 83  
 $El$  Elasticity of fluids 64, 83  
 $\epsilon^*$  Roundness of the corner of the channel 65, 84  
 $\varphi$  Flow rate ratio of phases 64, 83  
 $f$  Droplet generation frequency 64, 83  
 $h$  Channel height 64, 83  
 $\kappa$  Radius of curvature 34  
 $\eta$  Fluid kinematic viscosity 34  
 $\Delta P, \Delta P_{nb}, \Delta P_{caps}, \Delta P_{body}$  Laplace pressure gradient 34  
 $L_m$  Length of the main channel 64, 83  
 $L_{lag}^*$  Dimensionless lag distance 65, 84  
 $-\nabla P$  Pressure gradient term 34  
 $Q_c$  Flow rate of the continuous phase 64, 83  
 $Q_d$  Flow rate of the dispersed phase 64, 83  
 $R_{hyd}, R_m, R_c$  Hydrodynamic Resistance of the channel 64, 84  
 $R_n, R_{fill}, R_{pinch}$  Radius of back half of the droplet at different stages respectively 65, 84  
 $\beta_{slip}$  Slip factor 34  
 $\lambda$  Spacing between droplets 64, 83  
 $\gamma$  Interfacial tension 34  
 $t_{total}^*, t_{lag}^*, t_{fill}^*, t_{neck}^*$  Dimensionless total formation time, lag time, fill time, neck time, respectively 65, 84  
 $u_d$  Droplet velocity 64, 84  
 $V_{c_{fill}}^*$  Dimensionless control volume at the end of the filling stage 65, 84

- $V_{c_{pinch}}^*$  Dimensionless control volume at the pinch-off point 65, 84
- $V_d^*$  Dimensionless droplet volume 65, 84
- $u$  Fluid velocity 34
- $V_{fill}^*$  Dimensionless droplet volume at the end of the filling stage 65, 84
- $\mu \nabla^2 u$  Viscous term 34
- $w_c$  Channel width of the continuous phase 64, 83
- $w_d$  Channel width of the dispersed phase 64, 83
- $\wedge$  Channel width ratio of phases 64, 83

# Chapter 1

## Introduction

### 1.1 Research Background

Microfluidic technology has intensified over the last two decades and has a broad range of applications in various research areas such as chemistry, biology, pharmacology, and healthcare. The development of this technology has started with the need for scaling down of volume. Microfluidics originates from the field of chemical analysis, which uses techniques such as high-pressure liquid chromatography and capillary electrophoresis [70]. In these studies, it has been shown that using small amounts of sample helps to achieve high sensitivity and resolution. Besides providing highly sensitive analysis, scaling down has several advantages, such as reduction of reagent consumption, minimization of waste products, shortened analysis time, lowered overall cost, and an amenability to high-throughput. The advantages of microfluidic systems also allow researchers, specifically in the fields of chemistry and biology, to have a better understanding of the kinetics of reactions [114].

The majority of microfluidic systems have been investigated using single-phase fluids in microchannels. In single-phase systems flow is laminar. Therefore, mixing of fluids, which is one of the critical parameters for any kind of reaction, becomes sub-optimal. This is because mixing, under laminar flow, is dominated by diffusion, which is slow compared to the mixing from the turbulent flow. It is, therefore, difficult to maintain an optimal mixing in these systems. Another drawback of laminar flow is the cross-contamination between reagents in the channel. For example, a protein solution cannot be adequately evaluated due to the possibility of adsorption of proteins to channel walls, which can cause cross-contamination [114]. Droplet-based microfluidics is an alternative approach, which can prevent cross-contamination of reagents due to the compartmentalized structure of

droplets that blocks diffusion of reagents in the carrier fluid. Mixing is also enhanced because of the nature of the convective flow, which is a result of rotating vortices in moving droplets [90]. In addition, the small working volume of droplets prevents the use of excessive amounts of reagents. Lastly, since droplet generation can be done on the order of kHz, high-throughput can be achieved [16]. Therefore, droplet-based microfluidics can serve as a platform for studying the chemical synthesis and to perform biochemical assays. Most of these assays require sampling of biological fluids that are mostly non-Newtonian in nature. In the many applications of droplet-based microfluidic systems dealing with biological fluids, the focus has been on the quantification and detection of elements within these fluids, while research on the droplets themselves, or their formation, has largely been ignored. To fill this gap, a comprehensive formation analysis of droplet of red blood cells within microchannels was undertaken in this study. In the literature, the droplet formation dynamics of Newtonian fluids were analyzed by a few research groups where a mathematical model was developed for the prediction of the final droplet volume. However, due to the shear-thinning property of the red blood cells, the final droplet volume cannot be predicted using current mathematical models. Thus, a formation analysis and a new mathematical model of the final droplet volume of red blood cells are needed to be investigated. This study was followed by the development of a droplet-based hemagglutination assay to quantify viruses and virus-like particles. To achieve precise quantification, highly monodisperse droplets of red blood cells are needed to be generated so that batch-to-batch variations can be eliminated. Therefore, the design of the microfluidic network was done by considering criteria that has been identified in the dynamics analysis and more sensitive and faster quantification was achieved.

## 1.2 Thesis Outline

To place this work both in the field of microfluidics and biochemical assays, a literature survey that covers the fundamental aspects of both parts are presented in Chapter 2. In the first section, an overview of droplet-based microfluidic is discussed. This section outlines the fundamentals of droplet-based microfluidics, including the physics of two-phase fluids, the mechanism of droplet generation as well as droplet manipulation. In the second section, a brief summary of fluid properties of the interest of this study, such as rheology of red blood cells and property of red blood cells, are explained. The chapter ends with a focus on our virus of interest, namely Influenza, its structure and reactive components.

In Chapter 3, the fabrication of the microfluidic devices and the experimental setup used throughout this thesis are described.

In Chapter 4, a comprehensive study of biological non-Newtonian droplet generation in a T-junction microfluidic device is presented. In this study, red blood cells were used as the non-Newtonian fluid due to our interest in developing a droplet-based microfluidic system to detect virus particles. In this section, the dynamics surrounding the formation of droplets of red blood cells are detailed. The analysis was performed by investigating the effect of flow conditions and channel geometries on droplet formation.

In Chapter 5, by utilizing the analysis in Chapter 4, a mathematical model is developed to predict the final volume of red blood cell droplets, as well as the droplet generation frequency and the spacing between droplets. Then the mathematical model is validated by the experimental data.

Chapter 6 presents the application of a droplet-based microfluidic system aimed at the biochemical analysis of the Influenza virus. The system utilizes the established principles of the hemagglutination assay, such that virus or virus like particle (VLP) titer is determined via the agglutination profile of red blood cells. Contrary to the standard HA assay, which is more labor-intensive and time consuming, the droplet-based microfluidic system eliminates many of the drawbacks of the current assay. First, the hemagglutination reaction was observed in droplets and was compared to negative controls. From this, quantification was possible through image analysis. Various parameters that affect the hemagglutination reaction, such as red blood cell concentration, virus-like particles type, the freshness of samples, and droplet sizes were also investigated. Finally, the limit of detection was determined by lowering the concentration of the virus until the reaction in droplets became undetectable. Overall, this study presents a better performing assay compared to traditional protocols.

Chapter 7 summarizes the overall contributions of this work to the scientific field, states the major conclusions from my work, and further provides recommendations for the future development of this area.

## Symbols and Nomenclature

HA

VLP

HA assay

# Chapter 2

## Literature Review

In this section, an overview of the fundamentals of two-phase microfluidics and droplet generation are provided. This is followed by a literature review on the non-Newtonian fluid behavior of red blood cells. In addition to the flow behavior of red blood cells in microchannels, a brief introduction is given about the interaction of red blood cells with hemagglutinin proteins, as well as the relationship between hemagglutinin proteins and Influenza viruses.

### 2.1 Fundamentals of Droplet-Based Microfluidics

Droplet-microfluidics is a two-phase flow system where two immiscible fluids flow in a channel and share a common interface. Liquid or gas droplets flow through the channel via a carrier fluid (in most cases, oil). The focus of this study is related to liquid droplets that are carried with their complimentary oil. In cases where liquid droplets flow with their complementary oil, a number of distinct forces plays role in the development of droplets in microfluidic channels. Those forces are described in the following subsections.

#### 2.1.1 Forces and Dimensionless Numbers

Like any kind of fluid motion, droplet formation is determined by a competition of forces acting on a fluid. Since liquid-liquid two-phase microflows can also be described as a continuum, Navier-Stokes Equation (2.1) can be used to find those effecting forces.



$$\rho \partial u / \partial t + \rho u \nabla u = -\nabla p + \eta \nabla^2 u + f \quad (2.1)$$

The left side of the equation represents inertial acceleration, which is the sum of the time-dependent acceleration and the convective acceleration. The right side of the equation consists of the pressure force, the viscous force (friction force) and the gravitational force, respectively. Navier-Stokes equation can be simplified as four different forces acting on the droplet formation: inertial force  $f_i$ , pressure force  $f_g$ , viscous force  $f_v$  and capillary force  $f_\gamma$ , as shown in Equations 2.2 to 2.5.

$$f_i \sim \rho u^2 \quad (2.2)$$

$$f_v \sim \eta u / L \quad (2.3)$$

$$f_g \sim \rho g L \quad (2.4)$$

$$f_\gamma \sim \gamma L \quad (2.5)$$

By scaling and unifying these forces, dimensionless numbers can be derived to predict the behavior of different fluids. For example, the ratio of the inertial force to the viscous force is represented by the Reynolds number ( $Re = f_i / f_v$ ) (Equation 2.6).

$$Re = \rho u L / \eta \quad (2.6)$$

Due to low flow velocity in microchannels, the flow is laminar and the inertial forces become negligible. Therefore, microfluidic systems run in low Re number conditions ( $Re \ll 1$ ).

Under macroscopic flow conditions, there are a number of other dimensionless numbers that are used to describe the flow characteristics such as Grashoff Number, Weber Number and Bond Number as shown in Table 2.1 [8], [94], [39], [88], [102]. However, in microfluidic systems due to the high surface volume ratio of flows, gravity becomes insignificant which makes Grashoff number and Bond Number negligible. Since inertial forces are also negligible, Weber number becomes insignificant. As a result, the flow is governed by only viscous and interfacial forces. The competition between the viscous and interfacial forces can be evaluated using a dimensionless number known as the capillary number, see Equation 2.7.

$$Ca = \mu U / \gamma \quad (2.7)$$

As given in its definition, the capillary number involves specific parameters such as viscosity  $\mu$  (Pa.s), flow velocity  $U$  (m/s), and surface tension  $\gamma$  (N/m). All the listed dimensionless numbers except the capillary number has some degree of dependence on the characteristic length ( $L$ ) as shown in Table 2.1. This shows that the dependent dimensionless numbers become very small and ineffective as the characteristic length is reduced from the macro-scale to micro-scale. Eventually, by varying the capillary number, one can manipulate the formation of droplets in microchannels.

Dimensionless number	Competing Forces	Equation	Scaling
Capillary Number	Viscous/Interfacial	$\frac{\mu Q}{wh \gamma}$	0
Reynolds Number	Inertia/viscous	$\frac{\rho U L}{\mu}$	1
Grashoff Number	Buoyancy/viscous	$\frac{\Delta T \beta \rho^2 L^3}{\mu^2}$	3
Bond Number	Gravitational/Interfacial	$\frac{(\rho - \rho_t) g L^2}{wh \gamma}$	2
Weber Number	Inertia/Interfacial	$\frac{\rho U^2 L}{\gamma}$	1

Table 2.1: Dimensionless numbers in a two-phase microflow, which are scaled to the characteristic length. All the dimensionless numbers have a dependence on the characteristic length ( $L$ ), whereas the capillary number is independent of  $L$ , which makes it the governing dimensionless number when the flow is analyzed in micro-scale.

As one can see, the capillary number consists of the surface tension of fluids and flow conditions. In the following section, the impact of surface tension as well as the other fluid properties of microfluidics system are explained.

### 2.1.2 Effect of Fluid Properties

There are three main fluid properties that one needs to consider before generating droplets. The first one is wettability of fluids that are encapsulated in the droplets. Droplets are

carried in the channel via a continuous phase. The continuous phase acts as a lubrication layer between the droplets and the channel walls. However, there are cases where the droplets wet the channel surface not the continuous phase. As a result, the lubrication cannot be provided, and cross-contamination can occur in the channel. To prevent wetting, one must select a proper fluid. In most cases, an inert oil that has higher wettability than fluids in droplets is used as a carrier fluid. In other cases, a surface treatment is applied to the microfluidic channel to achieve the compatible wettability [56], [66].

In this study, hydrophobic channel walls were fabricated to achieve non-wetting conditions without applying an additional surface treatment so that the droplets repel from the channel walls; details are explained in Chapter 3.

The second consideration is the use of surfactants. Surfactant molecules consist of two parts, a hydrophilic head and a lipophilic tail. These parts are soluble in aqueous phases. Thus, the surfactant molecules migrate and become trapped at the interface of the two fluids as shown in Figure 2.1. The adsorption of the surfactant at the interface is a dynamic mass transfer process by diffusion or fluid flow (advection). Once the surfactant molecules migrate to the interface, they eliminate wetting of the channel walls of the microfluidic chip by creating a layer between the surface and the fluid. In addition, surfactants can alleviate the merging of the droplets, in case the collection of droplets is required after the droplet generation [106]. It is important to note that adding a surfactant lowers the interfacial tension between the droplet and the continuum phase, which affects the capillary number and droplet formation [117], [36].

Interfacial tension is defined as energy per unit area that minimizes the total surface area of the droplet and reduce the free energy of the interface. Internal surfactant molecules are balanced, surrounded by attraction and repulsion forces of the same molecules. At the interface of two fluids, there is a force imbalance due to the acting forces on the interface molecule. The interface molecules are pulled by the internal molecules and form a net inward direction force. To reduce this force, surfactant molecules reduce the interfacial area and form a spherical shape as shown in Figure 2.2. This curved shape creates pressure around the interface, which can be calculated using the Young-Laplace Equation 2.8. It is the equivalent of the Laplace pressure, which occurs in droplet formation in microfluidic channels.

$$\Delta p = \gamma \kappa \tag{2.8}$$

where  $\kappa$  is the radius of curvature, and  $\gamma$  is the interfacial tension (or surface tension for liquid-gas contact). Since interfacial tension depends on the temperature and the

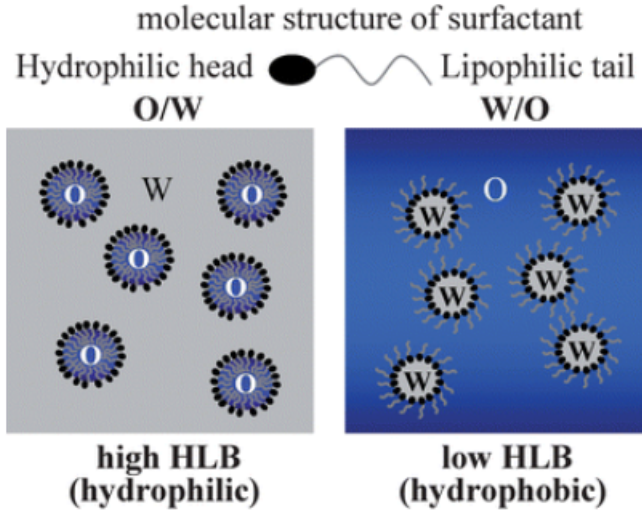


Figure 2.1: Schematic of the molecular transport of the surfactant molecules to the interface of two fluids. On the left, oil droplets are encapsulated in the water phase. Head parts of the surfactant molecules face outward and on the right, water droplets are encapsulated in the oil phase. Head and tail parts of the surfactant molecules align corresponding to the material of the phase [88].

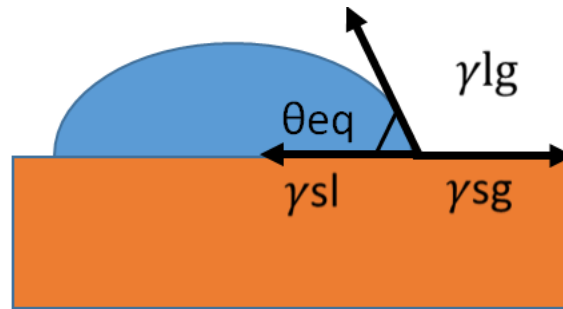


Figure 2.2: Schematic of the contact angle of a droplet on a solid surface with three surface tension values at equilibrium wetting condition.  $\theta_{eq}$  is the contact angle,  $\gamma_{sl}$  is the solid-liquid interfacial tension,  $\gamma_{sg}$  is the solid-gas interfacial tension, and  $\gamma_{lg}$  is the liquid-gas interfacial tension.

surfactant molecules at the interface, lack of surfactant molecules can change the interfacial tension dynamically resulting in formation of a Marangoni stress [8]. Marangoni stress

causes a flow along with the interface of fluids in the direction from low to high interfacial tension regions (Marangoni flow). As a consequence, the flow will be disturbed, and in the case of droplets, droplet formation and motion will be affected by these changes in the microchannel. Therefore, the surfactant was not used in this study to eliminate any additional dynamic changes during the formation process of shear-thinning fluid (red blood cells).

The third consideration is the material of carrier fluids (continuous phase). Many types of carrier fluids were used in the droplet-based microfluidic systems so far such as hexadecane, mineral oil, silicone oil, or perfluorinated oils. Hexadecane and mineral oils are not commonly used with polydimethylsiloxane (PDMS) microchannels since they lead to swelling of the channel [23], [63]. Perfluorinated oils have been mostly used for cell encapsulation in droplets to enhance the gas transfer, such as carbon dioxide CO<sub>2</sub> and oxygen O<sub>2</sub> in cells [81], [48]. In this study, silicone oil was employed as a carrier oil due to its ease-of-use to achieve the hydrophobic surface of the PDMS channel (see details in Chapter 3).

## 2.2 Droplet Generation Regimes and Methods

As discussed in the previous section, droplet generation occurs as a result of the competition between viscous and interfacial forces that can be described by the capillary number, which contains the information of four main parameters: surface tension, viscosity of fluids, flow rate and channel geometry. By altering these parameters, the flow field can be changed, and as a result, droplet formation can be adjusted. To manipulate the flow of dispersed phase (droplet content) and continuous phase (carrier oil), two different approaches are employed (Figure 2.3). The first one is the passive method, which utilizes the flow instabilities with the help of the channel geometry and flow rates. The second approach is known as the active droplet generation. In active generation methods, droplets are generated either by changing the balance of the force at the interface of two-fluids with the help of additional energy inputs (e.g. with electric fields, magnetic fields, and centrifugal forces) or by changing the intrinsic properties of fluids (e.g. viscosity, flow velocity and capillary force).

Before explaining the generation mechanism of a particular method, the droplet generation regimes are explained to enhance the understanding of the passive and active methods.

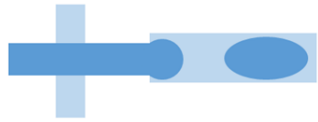


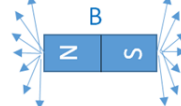


Microfluidic Droplet Generators	
A) Passive	B) Active
i) Flow Focusing 	iv) External Force
ii) Cross-Flow 	<div style="display: flex; justify-content: space-around;"> <div style="text-align: center;"> <p>Electric</p>  </div> <div style="text-align: center;"> <p>Magnetic</p>  </div> <div style="text-align: center;"> <p>Centrifugal</p>  </div> </div>
iii) Co-Flow 	v) Internal Force
	<p>Fluid Viscosity → <math>\eta_{\text{disperse}}/\eta_{\text{continuous}}</math></p> <p>Fluid Density → <math>\rho_{\text{disperse}}/\rho_{\text{continuous}}</math></p> <p>Fluid Velocity → <math>V_{\text{disperse}}/V_{\text{continuous}}</math></p> <p>Interfacial Tension → <math>\gamma_{\text{disperse}}/\gamma_{\text{continuous}}</math></p>

Figure 2.3: List of microfluidic droplet generators a) passive droplet generation methods that include i) flow focusing, ii) cross-flow, iii) co-flow designs b) active droplet generation methods that include iv) external forces and v) internal forces.

### 2.2.1 Generation Regimes

Generation regimes explain how droplets are formed under what flow conditions and capillary number. Depending on the generation regime, the droplet size, the generation frequency, and the spacing between droplets can change. Details are explained in the this section.

#### Squeezing Regime:

In the squeezing regime, the dispersed phase first reaches to the junction and starts to grow there. As the dispersed phase enlarges, the continuous phase is restricted, which builds up a pressure gradient over the emerging droplet interface. As the gap between the continuous phase and the channel wall decreases, the pressure continues to build up. Once the pressure gradient is sufficient to overcome the pressure inside the dispersed phase, the

interface is squeezed and deformed. Finally, the dispersed phase necks into a droplet, as presented in Figure 2.4a. Since the build-up of pressure is also related to the distance to the outer channel wall, the squeezing regime is dependent on the channel design. In this study, the droplet generation was done under the squeezing regime for all experimental studies.

### **Dripping Regime:**

The dripping regime occurs following the squeezing regime in a case where the capillary number is increased. As the capillary number increases, the viscous forces start to dominate so that the dispersed phase cannot grow in the main channel as in the squeezing regime [27], [108]. As a result, small droplets are generated, as shown in Figure 2.4b.

### **Jetting Regime:**

Jetting regime occurs when either the continuous phase or dispersed phase flow rate is increased while the dripping regime flow is present. The dispersed phase fluid extends along the horizontal axis with the continuous phase and immediately breaks up into droplets [93]. The jetting regime is driven by the viscous forces. As the magnitude of viscous forces exceeds the magnitude of capillary force, a jet of the dispersed phase stretches along with the continuous phase and thinning its tail before breaking up, as shown in Figure 2.4c.

### **Tip Streaming Regime:**

The tip streaming regime was observed only in co-flow and flow-focusing designs [14]. In this type of design, the droplet generation occurs when the dispersed phase tip deforms into a conical shape, and its apex breaks into droplets. To form a conical shape of the dispersed phase, the viscous force of the continuous phase must dominate the capillary pressure at the injection nozzle. In the thin jet region where the jet has a cone shape, as shown in Figure 2.4d. Since streamlines need to converge at the interface to form a cone shape, tip streaming cannot be generated in a T-junction design. In addition, the average dispersed phase velocity should be equal to the velocity of the continuous phase to enter the tip streaming regime.

### Tip Multi Breaking Regime:

The tip multi-breaking regime has been developed by Pingan Zhou et al. and this regime resembles the tip streaming regime in terms of forming a conical shape of the dispersed phase [121]. However, the conical shape of the dispersed phase in the tip multi-breaking regime can lead to instabilities and unequal droplet sizes. A discrete droplet generation occurs as opposed to continuous droplet generation in the tip streaming regime due to the oscillations of the conical shape, as shown in Figure 2.4e.

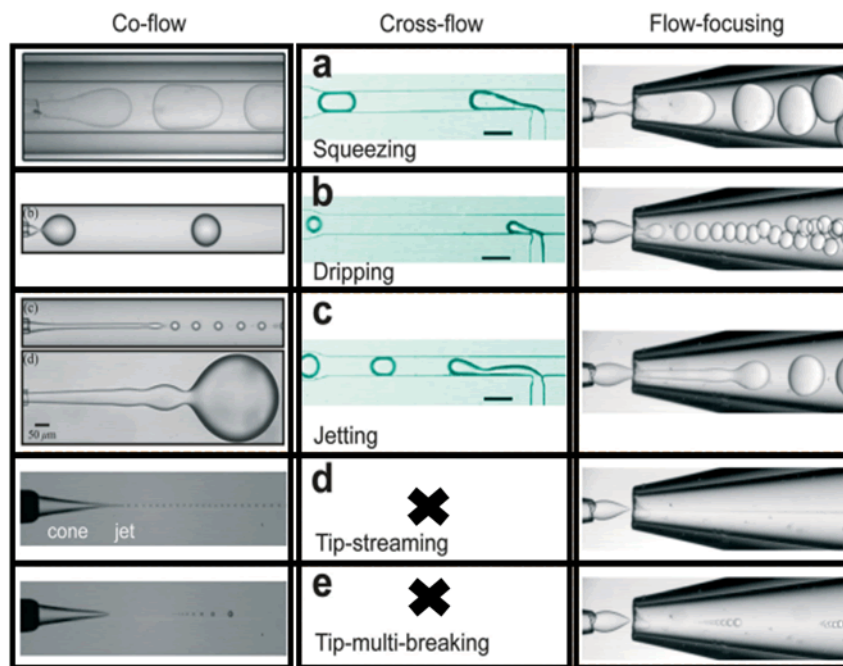


Figure 2.4: Microscopic images of five droplet generation regimes in the three major droplet generator designs. Droplets can be generated in all regimes in co-flow and flow-focusing designs (left and right images, respectively). However, tip-streaming and tip-multi breaking regimes cannot be achieved in cross-flow design (middle image) [14].

### 2.2.2 Generation Methods - Passive Methods

Passive droplet generation methods have three different generation geometries: Co-flow, Cross-flow and Flow-focusing. Besides, in each geometries different generation regimes can be achieved.



## Generation Geometries

### Co-flow:

Co-flow designs consist of two concentric capillary channels as shown in Figure 2.5a. The inner channel carries the dispersed phase while the outer channel carries a continuous phase. Once the inner phase meets with the outer phase, the viscous stresses stretch the interface of the inner phase until a droplet is formed. The performance of this geometry depends mostly on the flow rates of fluids. If the flow rate of the continuous phase increases, smaller droplets are generated at high frequencies. The flow rate of the dispersed phase has less influence on the droplet formation. Adding the surfactant into phases reduces the surface tension, which results in larger droplets [39]. This configuration is mostly used for generating droplets in the dripping and jetting regimes [21]. In the dripping regime, droplets break off at the intersection. However, in the jetting regime, droplets break off after forming an extended thread right after the intersection [21]. This design is not preferred due to the tedious fabrication procedure.

### Cross-Flow:

Cross-flow designs consist of two single channels that form either a T-shape [105] or Y-shape [96]. One channel carries the dispersed phase, and the other carries the oil phase (continuous phase) as shown in Figure 2.5b. The dispersed phase elongates into the junction until the shear forces of the continuous phase pinches off a droplet. The performance of this geometry mainly depends on the channel design and flow rates of fluids. Various generation performances can be observed by having different generation regimes in these geometries. In the squeezing regime, the dispersed phase penetrates the junction and touches the far channel wall before it is pinched off by a built-up pressure from the continuous phase [34], [109]. In the dripping regime, droplets are pinched off before the droplets contact with the far wall. In this regime, the generation is governed by the force balance between the viscous drag on the penetrating interface and the surface tension of the dispersed phase. In the jetting regime, the dispersed phase penetrates the junction and, flows downstream and the generation of the droplet occurs from the that constant dispersed phase thread.

This geometry is highly preferred for droplet generation due to its simplicity to generate droplets and its capability to control the droplet size. Garstecki et al. developed a detailed scaling law that models final droplet volume in the squeezing regime [34]. Formation of droplets in this regime depends on the geometry of the intersection plus the amount of the fluid pumped into the droplet at the junction as its neck collapses. A similar model

has been developed for the dripping regime by which shows that droplet size inversely scales with the capillary number [49]. An additional regime occurs in between squeezing and dripping regimes, which is called a transition regime. Christopher et al.; developed a model for the transition regime which required the addition of fluid viscosities [16]. In this study, only cross-flow was used to generate droplets. In Chapter 4 and 5, a simple T-junction was used to analyze the formation dynamics of droplets of red blood cells. In Chapter 6, two dispersed phases flow in the Y-shaped channel connected to the T-junction were used to generate droplets of two different reagents.

### **Flow Focusing:**

Flow focusing designs consist of three planar channels and one orifice, as shown in Figure 2.5c. The middle channel carries the dispersed phase, and the other two channels carry the continuous phase. Because of the symmetric viscous stresses caused by the continuous phase and the high shear stress at the orifice, the dispersed phase breaks off as all three flows go through the orifice [5]. The performance of this geometry depends on the channel geometry, and the flow fields both before and after the orifice [61]. In this design, different generation regimes can be achieved. In the squeezing regime, the dispersed phase grows at the intersection and blocks the flow of the continuous phase, which causes pressure to build-up. Built-up pressure squeezes the dispersed phase and a droplet pinches off at the intersection of the channels. In the dripping regime, with the help of an increased continuous phase flow rate, the generation occurs at the intersection of the channels. After the droplet pinches off, the dispersed phase fluid stays at the orifice. As the flow rate of the oil phase increases, the dispersed phase forms a thread through the downstream (after the the intersection of the channels) at which point the system in the jetting regime. If surfactant is added (near the critical micelle concentration), a longer thread than in the jetting regime forms beyond the intersection where droplets form. The latter is referred to the tip-streaming regime [6]. An additional regime, called tip-multi breaking occurs in the presence of oscillations in the dispersed phase. In addition, monodispersity of the droplets depends on the generation regime. For example, highly monodisperse droplets can be achieved in the squeezing and dripping regimes. However, in the tip-multi breaking regime, equal size droplets can not be formed due to the oscillations in the flow.

### **2.2.3 Generation Methods - Active Methods**

The generation of droplets in active methods is mainly referred to as “on-demand generation.” While droplet size and generation frequency are dependent on each other in the

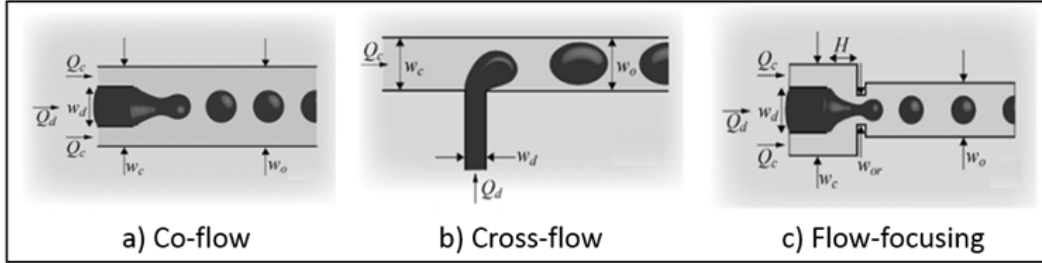


Figure 2.5: Schematic of passive microfluidic droplet generators: a) co-flowing, b) cross-flowing and c) flow focusing [16].

passive droplet generation methods, in the active methods, they are independent of each other. One advantage is reduced stabilization time for droplet generation. In active methods, it has been observed that droplet generation can be stabilized faster than passive methods [15]. Active droplet generation methods can be classified by the type of the external forces applied to the microfluidic system. The majority of active droplet generation methods have utilized the flow focusing and co-flow microfluidic designs [122]. In addition, each force can be utilized for different applications in the microfluidic system. For instance, an electrical force can be used in various ways, such as for di-electrophoresis, electro-wetting and electrochemical reactions. To run fluid flow with the electric field, the dielectric constant or surface tension of fluids are needed to be known. Based on the application requirement for the flow, different electric field should be applied.

## 2.2.4 Comparison of Droplet Generators

A comparison of droplet generators that fall under passive and active methods can be made based on the application type, compactness of the system, and ease of fabrication. In the case of the droplet generation and manipulation, most researchers prefer passive methods due to their simplicity. In the active method, droplet generation relies on tedious fabrication steps and external equipment such as electrodes, magnets and piezo-materials. In passive methods, the geometric design of flow focusing, and T-junction microfluidic chips govern the droplet formation without any external force. However, the geometry of the passive droplet generators is dictated by the application requirements. For example, flow focusing designs are more preferred than T-junction designs for single cell encapsulation applications due to the design's capability to align the cells in incoming flow which increases the probability of encapsulation only one cell per droplet. Another example is analysis

of formation dynamics of droplets. Dynamics analysis has been investigated by many researchers for Newtonian fluids under the T-junction geometry. Therefore, one can desire to use the T-junction design to analyze the droplet formation of different fluids to have the opportunity to compare the data with the previous studies.

## 2.3 Droplet Motion in a Microfluidic Channel

To manipulate droplets in a microchannel, motions of the droplets need to be well understood. Plug-like-shaped droplets are droplets confine the cross-section of the channel and have a longer length than the channel width, as shown in Figure 2.6.

### 2.3.1 Fluid Motion in a Droplet

As droplets move through the channel, counter-rotating re-circulation zones occur, as shown in Figure 2.6. Circular motion in the droplets is divided into two half portions of droplets, and each side flow in opposite directions. For plugs that occupy the majority of the cross-sectional area of the channel, local and global flow fields are influenced by hydrodynamics. Fuerstman et al. have shown that changes in vortices (flow field) that are created by droplet motion are due to the viscosity difference of the fluids in the channels [32]. As a result, the distribution of flow in the microfluidic network depends on the hydrodynamic resistances of both branched channels and droplets in those channels.

### 2.3.2 Hydrodynamic Resistance of Droplets in Microchannel (Pressure Drop)

Hydrodynamic resistance is explained by the relationship between pressure drop and flow rate. This relationship is analogous to that of Ohms' Law, where the voltage (pressure drop) is related to the current (flow rate) by means of resistance; however, due to the complex physics of the droplet shape, it is hard to have as robust of an expression for resistance in microfluidic channels. The complexities with respect to the droplet is mostly related to the lubrication layer between the droplets and the channel walls in Figure 2.7b, and the curvature at the front/back end of the droplets, as shown in Figure 2.7a.

To estimate the pressure drop in the microchannel, Fuerstman et al, defined the total pressure drop as a sum of three different pressure drops. The first one is related to

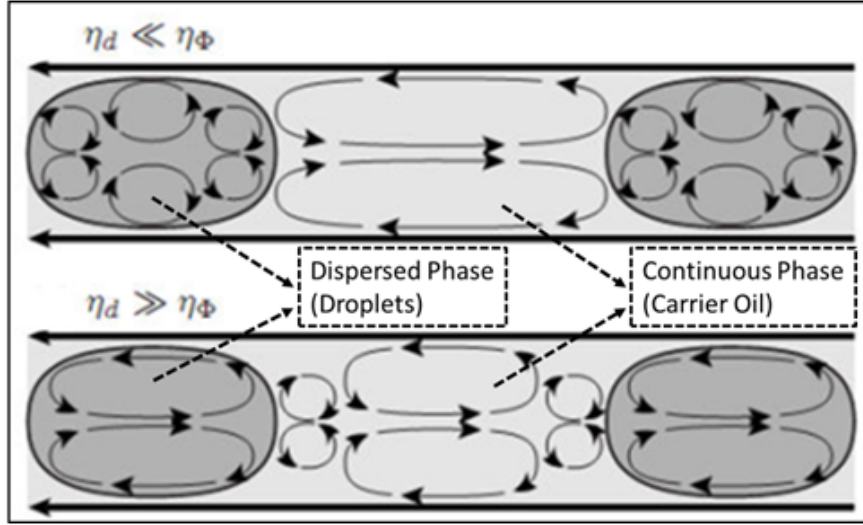


Figure 2.6: Schematic of the vortices in the droplet and the continuous phase for two different cases ( $\eta_d \ll \eta_\phi$  or  $\eta_d \gg \eta_\phi$ ). The top figure indicates the case where the viscosity of the carrier oil is much larger than the fluid viscosity in the droplets. The bottom figure illustrates the case where the viscosity of the continuous phase is lower than the fluid viscosity in the droplets. In the latter case, the number of vortices is higher than the former case in droplets [32].

the pressure drop due to the viscous resistance of the continuous phase between droplets ( $\Delta P_{nb}$ ). Similar to the first one, the second one is the pressure drop due to the viscous resistance of the body of the droplet ( $\Delta P_{body}$ ). The last one is the Laplace pressure jump due to the curvatures of the droplet ( $\Delta P_{caps}$ ). Using the Ohms' Law analogy, the pressure drops can be given by the expression below (Equation 2.9):

$$\Delta P = (a\mu_c/wh^3)LQ = (a\mu_c/h^2)LU \quad (2.9)$$

where  $a$  is a dimensionless constant,  $\mu$  is the viscosity of the continuous phase,  $L$  is the length of the plug/droplet,  $Q$  is the flow rate of the continuous phase, and  $U$  is the mean velocity of the continuous phase. From this expression, Fuerstman et al. developed an expression for the pressure reduction of the cap region of the droplets as given below (Equation 2.10).

$$\Delta P_{caps} = N_d c \mu_c (\gamma/h) Ca^{2/3} \quad (2.10)$$

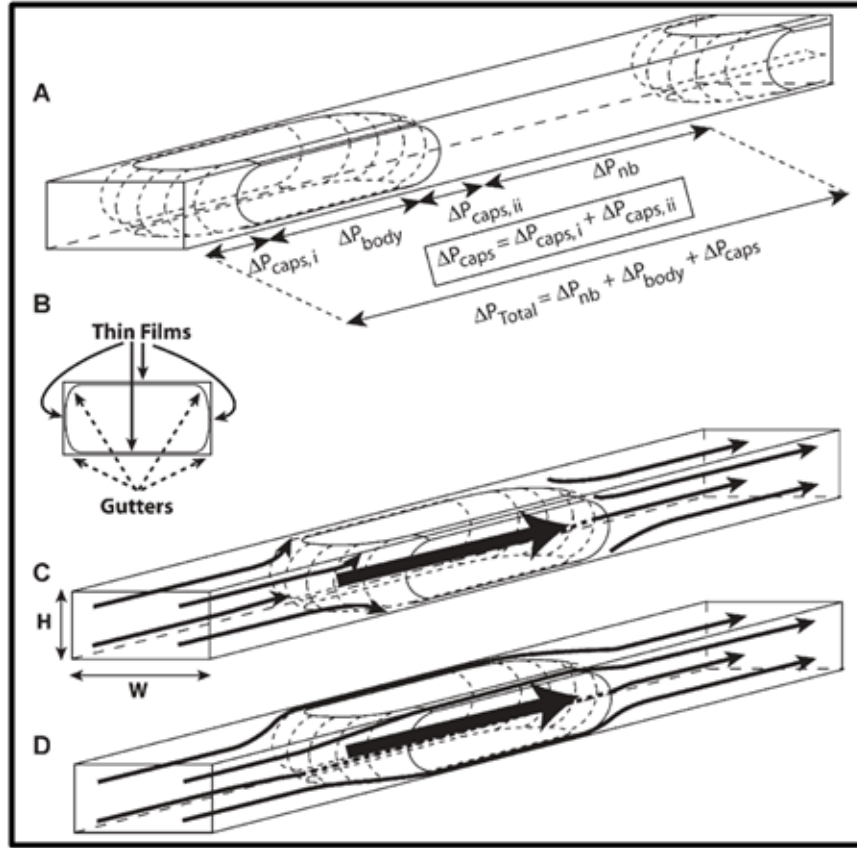


Figure 2.7: a) The sketch illustrates the curvature of both ends of the droplets and the pressure drop along a microchannel b) Cross-section view of the droplet showing the lubrication layer (thin film) and the gutter region (the gaps between the droplet and four channel corners), which makes the droplet resistance complex c) A schematic diagram illustrates no flow of the lubrication layer is present d) A schematic diagram showing the lubrication layer bypasses the droplet [32].

where  $N_d$  is the number of droplets,  $c$  is a dimensionless parameter which depends on geometric parameters ( $w$ ,  $h$ ,  $L_{droplet}$ ). By using the same expression given in Equation 2.10, the continuous phase pressure drop, and the droplet body pressure drop can be found, as shown below, respectively in Equations 2.11, 2.12.

$$\Delta P_c = a(\mu_c/h^2)L_cU_c, \quad (2.11)$$

$$\Delta P_d = b(d/h^2)L_d U_d, \quad (2.12)$$

where  $a$ ,  $b$  are dimensionless parameters,  $\mu_d$ ,  $\mu_c$ ,  $L_d, L_c$  and  $U_d$ ,  $U_c$  are the viscosity, the length and the average velocity of droplets and the continuous phases respectively. The total pressure drop is the sum of the Equations 2.10, 2.11, 2.12. One can see that the pressure drop is a complex expression; it involves viscosity of the fluids, the velocity of each phase, the channel geometry and the interfacial tension of the fluids. Several experimental studies show how these parameters influence the overall droplet resistance. For example, Adzima and Valenkar et al. have shown that the hydraulic resistance of the droplets increases with droplet size and decreases with droplet velocity [2]. Vanapalli et al. found that the resistance increases as the droplet fluid viscosity increases, which increases the magnitude of the pressure drop, as shown in Figure 2.8 [110]. Finally, Labrot et al. found that, the overall droplet train resistance decreases due to eddies that are formed in the continuous phase as the spacing between droplets decreases (see, Figure 2.6 for eddies/vorticities in continuous phase) [60].

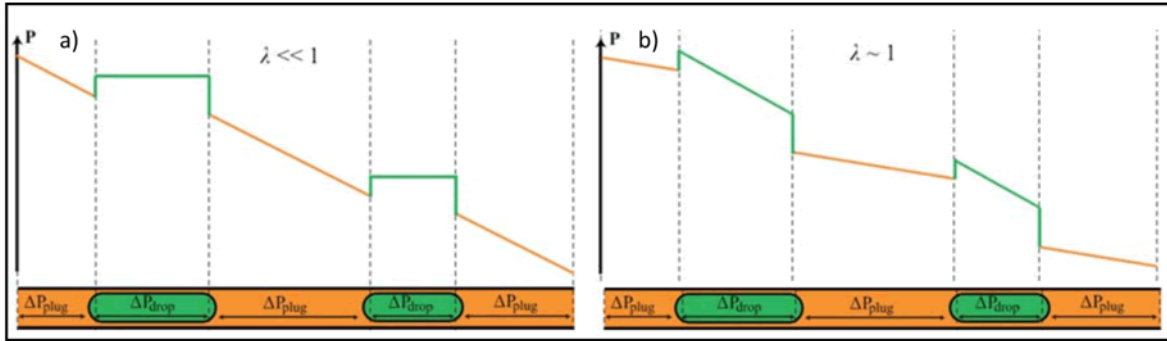


Figure 2.8: Schematics of the pressure drop along a microchannel containing a droplet train. In the case of (a) where inviscid droplets ( $\eta \ll 1$ ) were generated, pressure remains constant along the body part of the droplet. However in the case (b) where viscous droplets ( $\eta \sim 1$ ) were generated, pressure drops along the body part of the droplet [8].

### 2.3.3 Droplet Velocity in Microchannel

Besides the hydrodynamic droplet resistance, the droplet velocity also contributes to the flow motion in the channel. A lubrication layer surrounds the droplet, as shown in Figure 2.9 has an impact on slug (slug/plug: a droplet that confines the cross section of the

channel) motion. In a circular capillary channel, it has been shown that a thin film causes droplets to move faster [27]. However, in a rectangular channel, droplets move slower than the surrounding fluid due to the flux at the gutter [115], which has the same direction as the droplet motion, as shown in Figure 2.9c, d. Therefore, it is important to consider the droplet size while analyzing the formation dynamics. In this study, only plug (or slug) like droplets were used to identify the pressure drop by Equation 2.12.

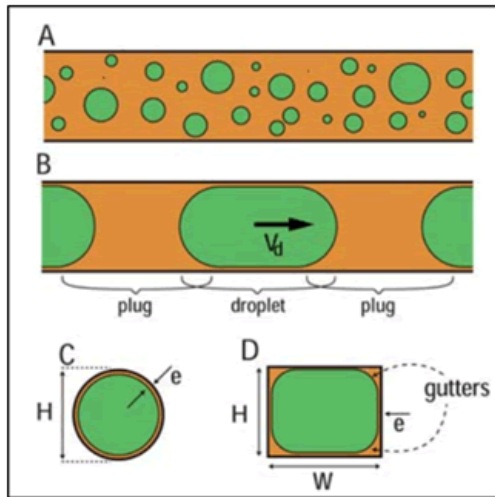


Figure 2.9: a) Schematic of isolated droplets where droplets do not confine the channel and float. b) Schematic of slug/plug like droplets that confine the channel cross-section. c) Schematic of lubrication layer/oil phase between the isolated droplets and the channel walls. d) Schematic of the lubrication layer with the gutter formation between the edges of the rectangular channel and the slug/plug like droplet. The gutter region causes back flow of the oil phase to the opposite direction of droplet flow which changes the entire flow field in the microfluidic channel [8].

When the droplets move in the direction as shown in Figure 2.9b, the continuous phase is pulled back by the droplets in the opposite direction due to the viscous forces, which is the source of the lubrication film between the droplet and the channel wall. In addition to the movement of the droplet, since the Laplace pressure in the droplet is larger than the pressure in the continuous phase, there is a Laplace pressure jump at the interface, which moves the carrier fluid from the lubrication layer into the bulk. The velocity difference between the droplet and the continuous phase in the main channel is described by slip factor,  $\beta_{slip}$ , as given expression below [86], [60]:



$$u_d = Q_m(\beta_{slip})/(wh), \quad (2.13)$$

where  $Q_m$  is the continuous phase flow rate in the main channel. This expression becomes more complex in the presence of the viscous droplets [47], [3] and several studies have been done. Vanapalli et al., showed that the slip factor is constant ( $\beta_{slip}=1.28$ ) for viscous drops for any viscosity ratio in the system. However, Labrot et al., showed the slip factor ( $\beta_{slip}$ ) equals to 1.6. Sessoms et al., have shown that when the droplet length is shorter than the channel width,  $\beta_{slip} > 1$  and vice versa [87]. The dependence of slip factor on three parameters: channel width, droplet length, and viscosity ratio has been summarized as follows [51]:

- For  $\eta < 1$  and length  $1.5 < l/w < 3$ :  $\beta_{slip} \sim 0.95$ -1.35.
- For  $\eta < 1$  and  $l/w > 3$ :  $\beta_{slip} \sim 1$ .
- For  $\eta = 3$ :  $0.6 < \beta_{slip} < 0.95$ .
- For  $\eta = 33.3$ : the trend between the slip factor and the size of the droplet was linear.

In our study, to eliminate the error, a flow sensor was used to measure the flow rate of the continuous phase and the droplet speed were calculated using frame by frame image analysis in Chapter 4 and 5.

Adding the surfactant into the system makes the slip factor more complicated due to the local variation in the boundary condition at the interface (Marangoni stresses). However, it has been shown that droplet velocity decreases compared to those that have no surfactant inside [95], [3], [34]. Since no surfactant was used in this study, the impact of the surfactant on the flow field of microfluidic network is not a concern.

## 2.4 Passive Manipulation of Droplets in Microchannels

In previous sections, the droplet generation mechanism and droplet motion in the microchannel are explained. By using the given information of flow physics in those sections, manipulation of the droplets for specific functions such as droplet sorting, droplet merging, and droplet splitting can be easily implemented. Manipulation of the droplets can be done

actively and passively. Since all the projects are completed using passive manipulation methods in our study, the examples in the following sections are related to the passive manipulation methods.

### 2.4.1 Mixing in Droplets

Chemical reactions require mixing of reagents in a reactor. Since, droplets act as an individual reactor in a microfluidic system, reagents must be mixed in droplets to complete the reaction [74]. Passive mixing in droplets generally relies on the diffusion. More specifically, in droplet-based mixing, the mechanism is based on the turns and bends of the liquids that are encapsulated in the droplets. When a droplet flows through a serpentine channel, the body and the edges of the droplet contact the channel at different angles. For example, a trailing edge of the droplet is exposed to a larger arc, whereas the receding edge of the droplet makes contact at a small angle. As a result, smaller circulation of liquids in the droplet occurs at the receding edge compared to the trailing edge. Also, turning in the serpentine channel causes the liquids to invert in the droplet, which leads to extra stirring, as shown in Figure 2.10 [12].

### 2.4.2 Splitting of Droplets

To increase the functionality of the device, a droplet can be split into two daughter droplets. Thus, each daughter droplet can be used in different reactions or functions in a device. The splitting mechanism relies on using shear forces to elongate the mother droplet until it breaks up into two smaller droplets. Several parameters are needed to be considered during the breaking of the droplet, such as the flow rate ratio of fluids, resistance of the outlet channels, and geometry of the channel. Splitting has been achieved using Y and T junctions, as shown in Figure 2.11 [63]. The mother droplet comes to the bifurcation and starts to elongate. This elongation blocks the channel, and the pressure at the upstream of the channel builds up. Built-up pressure squeezes and elongates the droplet until it is pinched off.

### 2.4.3 Coalescence/Merging of Droplets

Droplet merging can be achieved by changing the geometry of the microchannel. Bremond et al. developed a channel that involves an expansion region where droplets slow down and merge with the former droplet in a sequence, as shown in Figure 2.12a [10]. Droplet

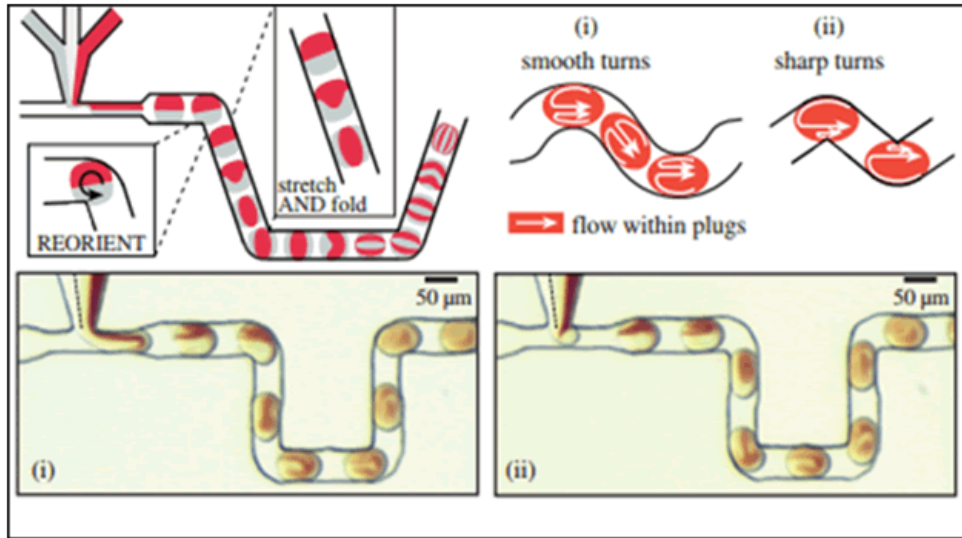


Figure 2.10: The top figure illustrates the mixing in droplets. Vortices in the droplets changes as the angle of the serpentine channel changes. Smooth turns (i) maintain the symmetry in the vortices and cause slow mixing. However, sharp turns (ii) break the symmetry and lead to faster mixing. The bottom figure is the microscope image of mixing of two different food dyes in droplets [12].

coalescence does not occur in the expansion region; but at the exit of the extension region since the two tips of the droplets form an interface and fuse into each other.

Another design developed by Niu et al. had pillars in the expansion part [76]. A pillar was used to trap a droplet and hold it until another droplet arrives and merges to the former. The trap mechanism is governed by surface tension forces and hydrostatic forces that occur due to the blockage of flow between pillars. When the second droplet comes into the trapping region, pressure builds up at the upstream and forces the droplet to merge with the first one, as shown in Figure 2.12b.

#### 2.4.4 Sorting of Droplets

Sorting process is an essential step to isolate the desired droplets that are generated in the channel. In passive sorting, two parameters are considered: drag force in the channel and droplet size compared to channel dimensions [100]. Droplets with a smaller diameter than the channel diameter tend to flow in the regions where the flow velocity of the continuous

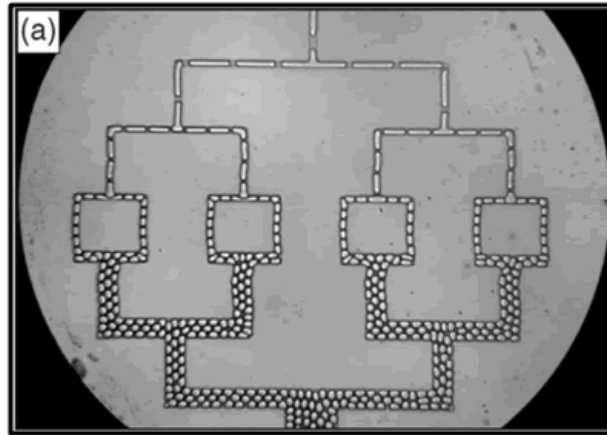


Figure 2.11: A microscope image of droplet splitting using a bifurcation design in the channel. A larger droplet came to the T-junction at the top of the figure and was split into two daughter droplets. Then, these two droplets were split into four at the second T-junction. This procedure continued until the last T-junction in the design [63].

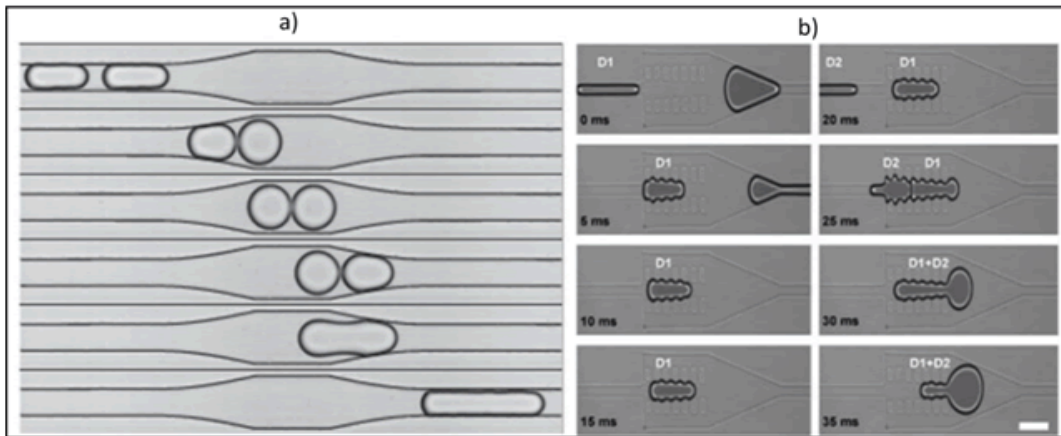


Figure 2.12: Microscope images of two different passive droplet coalescence/merging methods a) droplets merged at the exit of the expanded part of the channel b) the previously formed droplet was held by the pillars, and the following droplet merged with the previous droplet [10].

phase is maximum [100]. However, droplets with a larger diameter than the channel width will flow slower than the continuous phase. Therefore, the smaller droplets will follow a narrow branch of bifurcation, whereas the larger droplets will flow through the larger

branch, as shown in Figure 2.13 [71].

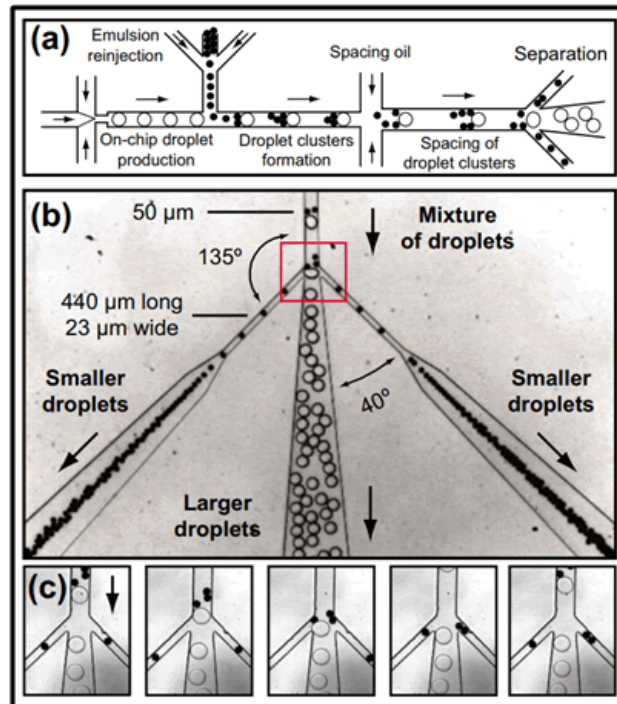


Figure 2.13: Passive sorting of droplets. a) Schematic of overall microfluidic channel design for droplet separation. b) Microscope image showing the separation of the larger droplets from the small droplets c) Enlarged view of the separation channel [71].

## 2.5 Characteristics of Blood Cells

In this section, elements of red blood cells are explained in general. Since all the experiments were done by using chicken red blood cells in this thesis, the red blood cell morphology, and flow characteristics are reviewed.

### 2.5.1 Components of Blood

Blood for vertebrates consist of three major components. The first part consists of the blood cells, which include red blood cells (erythrocytes), white blood cells (leukocytes)

and platelets (thrombocytes). The second part are the lipoproteins, which transport lipids throughout the body. The third one is plasma, which consists of electrolytes, water and other dissolved proteins. Red blood cells make up the majority of the blood cells. Human red blood cells account for 45% of the total volume fraction of blood cells. The volume fraction of red blood cells is also known as the Hematocrit level. Since red blood cells have the largest fraction, flow behavior of blood is mostly governed by these red blood cells. In addition, type of the red blood cells impact the blood flow due to the difference in cell deformation ability, viscosity, presence of nuclei and shape.

## 2.5.2 Red Blood Cell Morphology

Red blood cell size and shape depend on the species [43]. For example, the human red blood cells are smaller than those the birds and reptiles. Avian red blood cells have an ovoid shape and are nucleated, unlike human red blood cells [19]. In addition to this shape, avian red blood cells have additional cytoskeletal elements on the membrane, and the shear modulus at the cell membrane is higher than mammalian cells [26].

In this study, our focus is specifically the avian red blood cells. This is because quantification of the produced virus/virus-like particles is generally done using chicken red blood cells due to their convenience to handle in laboratories. In addition, laboratories require additional safety regulations to work with human red blood cells. Thus, chicken red blood cells were used in our experiments.

## 2.6 Influenza A Virus and Virus-Like Particles

### 2.6.1 Influenza A Virus

Influenza viruses are enveloped RNA viruses that typically have a diameter of 80 to 120 nm, as shown in Figure 2.14. They are further classified into three different types; Influenza A, B and C. Type A Influenza is the most significant cause of morbidity and mortality in the modern world [77]. The Influenza virus genome consists of 8 single-stranded RNA fragments. These fragments are used for encoding proteins. Of these, hemagglutinin surface protein (HA) is used for attachment of the virus to sialic acid on a host cell and also for membrane fusion between the virus and the cell. Another protein is known as neuraminidase surface protein, which is required to cleave sialic acid-HA protein binding. A third protein, M1, assists in viral structure by viral binding RNA with HA and NA. Other

proteins such as M2, PB1, PB, PA, NP, NS1 and NS2 have functions in viral infectivity and transmission of the host cell.

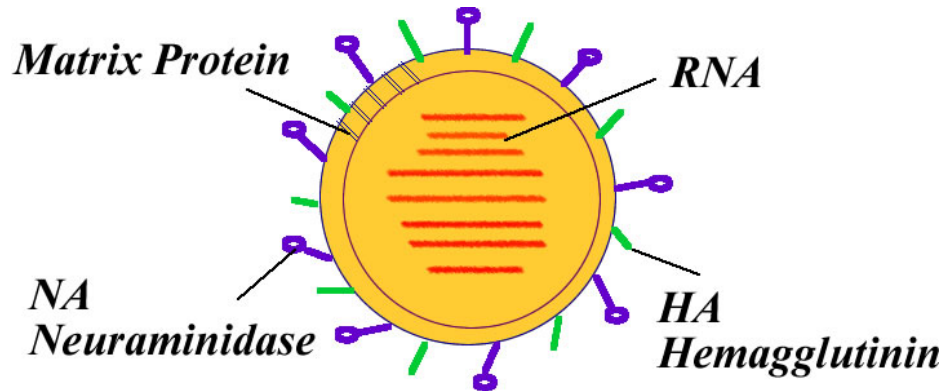


Figure 2.14: Schematic of Influenza A Virus. The virus contains Hemagglutinin (HA) and Neuraminidase (NA) proteins at the surface, RNA at the core and Matrix Proteins at the interface.

The infection cycle consists of several steps, as shown in Figure 2.15. In the first step, the Influenza virus attaches to the sialic acid of the host cell membrane with the help of the Hemagglutinin protein (HA). After binding, the virus is up taken into the host cell by endocytosis as a second step. Due to the acidic environment of the cell, the virus opens its channel to release its viral RNA. In the third step, the viral RNA enters the nucleus to start replication of its own by using a host cell machinery. As a next step, the surface proteins of the virus and the viral RNA are exported to the cell membrane. Finally, new viruses bud out of the host cell to infect another host cell around.

## 2.6.2 Influenza A Virus Vaccine

Vaccines are not only used to provide immunity to a particular disease but also play a role in therapeutic applications, such as the treatment of certain cancers. A typical vaccine consists of either a dead or weakened microorganism or microorganism toxins/surface proteins that cause disease. Once these organisms enter the body, they stimulate the immune system. By stimulation of an immune response, antibodies are created to bind, isolate and lead to the destruction of the foreign microorganism and the antibodies created lead to a memory of the microorganism for subsequent infections.

The most important reservoir of Influenza A virus is wild birds. 16 different subtypes of the virus are known, based on the antigenic properties of the HA protein. Because

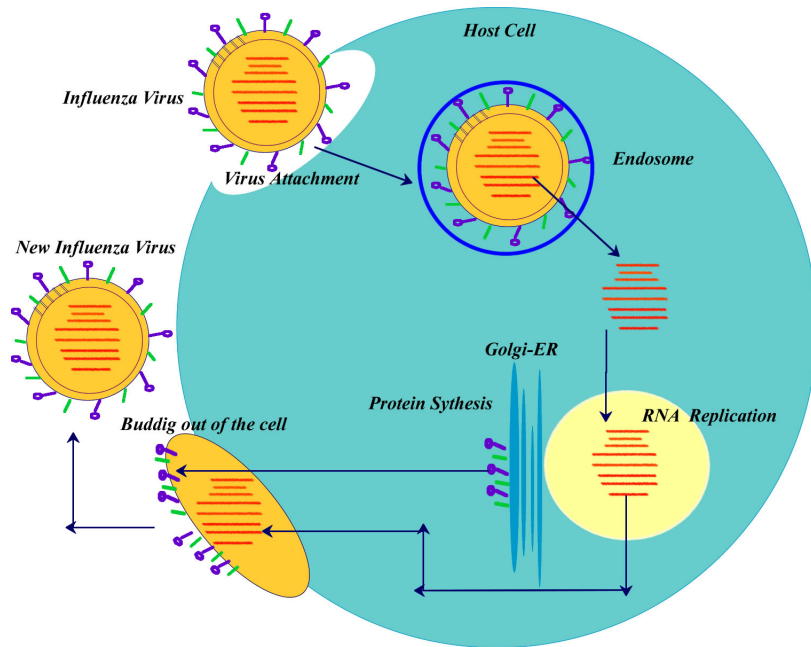


Figure 2.15: Schematic of Influenza virus infection cycle in the a host cell. The cycle starts with attachment of the Influenza virus with the sialic acid receptors of the host cell. Once the attachment is complete, the virus enters into the cell with endocytosis. Then, the virus release its RNA. The released RNA enters into the nucleus of the host cell to start replication of itself. Then, the surface proteins of the virus and the viral RNA are exported to the cell membrane to form a new virus. Finally, the new virus emerges from the host cell.

it is an RNA-based virus (mutations occur much more frequently in RNA than in DNA molecules) and because of its segmented genome, it is highly possible to encounter newly mutated viruses [31] and these viruses can cause new epidemics for the coming year – and in some cases even a pandemic. Repeated (yearly) vaccination are the most effective way to control Influenza infection because vaccine strains are determined based on the epidemiological and antigenic properties of current circulating human strains. Two types of vaccines are commonly available, which require fertilized chicken eggs as a substrate [52]. One is a chemically inactivated vaccine (inactive but previously virulent) of detergent-split virion subunits, containing the hemagglutinin protein (HA). It has been observed that this type of vaccine does not sufficiently protect the elderly [103]. The other vaccine type is known as a live attenuated vaccine (active but less virulent), which has been approved by FDA to be used in patients aged six months to 49 years [52].



During an avian Influenza virus outbreak (an outbreak caused by the virus jumping from one species to another - from birds to humans), propagation of the virus in eggs may be hindered because of the lethality of the virus to chickens. In addition, and more generally, people with egg allergies cannot be vaccinated by the vaccine that is produced in eggs. Furthermore, biosafety level 3 facility requirements support the need for developing new influenza vaccines that do not rely on propagating Influenza virus or use eggs. To eliminate these drawbacks, production of virus proteins or even non-replicating virus-like particles in cell culture have become available.

### 2.6.3 Virus-Like Particle (VLP)

Virus-Like Particles are protein complexes that are composed of viral structural proteins, as shown in Figure 2.16. When structural proteins are expressed in the recombinant system, they assemble and form virus-like particles. These particles mimic the organization and structure of the original virus, but they do not contain any genetic material inside.

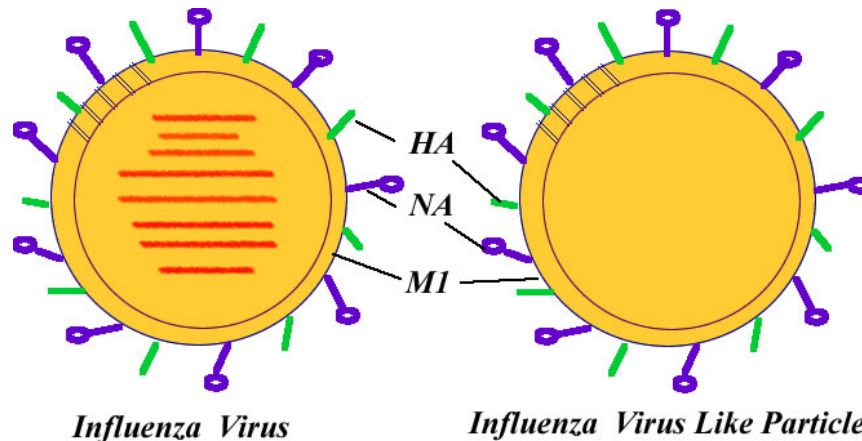


Figure 2.16: Schematic of Influenza A Virus (Left) and Influenza Virus-Like Particle (Right). The fundamental difference between Influenza virus and Influenza VLP is that the VLP does not contain RNA.

## 2.7 Virus Quantification Methods

To prevent pandemic outbreak of Influenza virus, rapid diagnosis is needed, along with effective vaccine manufacturing during the acute phase of an infection. Recently, many di-

agnostic methods have been developed. In the following section, these detection methods are briefly explained. Influenza A virus quantification methods can be grouped in three major categories: antibody-dependent methods, antibody-independent methods, and methods for infectivity measurement as shown in the Figure 2.17 [103].

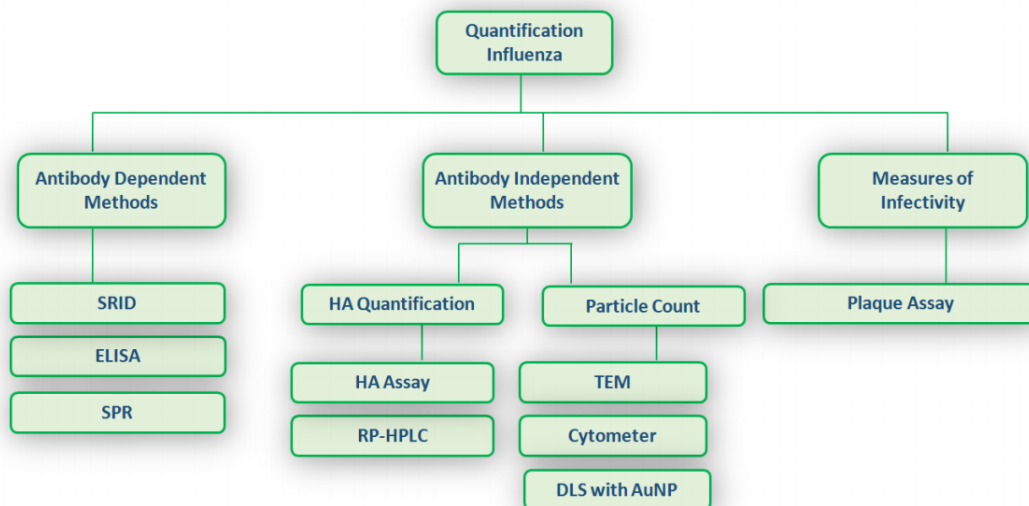


Figure 2.17: List of Influenza virus quantification methods. The quantification methods are categorized under three main branches, which are antibody dependent methods, antibody independent methods and measures of measures of infectivity.

### 2.7.1 Antibody Dependant Methods

#### Single Radial Immunodiffusion (SRID):

This method measures the radial diffusion of viral antigens in agarose gels containing antibodies. A ring forms upon injecting the viral antigen into the agarose gel. The concentration of the target virus can be determined based on the diameter of the ring. The limit of detection of this method is 3-5  $\mu\text{g}/\text{ml}$  of HA. Although this method is approved by the WHO, it has several limitations, such as having a time consuming detection procedure, requiring a strain-specific antibody, which raises the cost of the detection system, and variability of results due to the operator [104].

### **Enzyme-Linked Immune Sorbent Assay (ELISA):**

This method is used to detect presence of antibodies in biological samples. A biological sample is interacted with enzyme linked antibodies on a plate based assay. Once the interaction of antigens with antibodies is complete, the activity of the enzymes, so called reporter enzymes, is measured to quantify the amount of antigens, typically observing a color change. Although this is a promising method for vaccine development, this method has not been used to detect Influenza VLPs [103].

### **Surface Plasmon Resonance (SPR):**

The principle of SPR is based on the competitive binding of antibodies to the proteins present in the sample. The concentration of HA proteins can be quantified by analyzing the binding of HA to sialic acid by observing the color change of gold nanoparticles [68]. However, this technique was abandoned due to the low limit of detection. In addition, VLP detection has not been conducted with this method. Therefore, the limit of detection for VLPs is unknown [104].

## **2.7.2 Antibody Independent Methods**

### **Hemagglutination Assay (HA Assay):**

Hemagglutination assay is used to quantify virus, bacteria and antibodies in red blood cells. The activity is measured by observing agglutination of red blood cells (RBCs). In the presence of viruses, cells and viruses start to bind together and form a lattice. The reaction looks like a homogeneous red sheet in the 96-well plate as shown in Figure 2.18. However, red blood cells precipitate to the bottom of the well, in the absence of the virus-cell binding reaction.

The procedure of the assay starts with dilution of an unknown quantity of the virus from the first well of the plate to the last well. Then, red blood cells are added into each well to start reaction. At the end of the reaction, titer of the virus can be calculated by dividing the dilution factor to the sample volume. For example, as shown in Figure 2.19, virus titer was equal to 128 HAU/50  $\mu$ l for the given 10% RBC concentration of the sample.

Although the assay procedure is commonly used for virus quantification, this method has few limitations. For example, the read-out of the reaction is subjective to the operator's judgement, the reaction takes long time to run for a single test, assay preparation is tedious

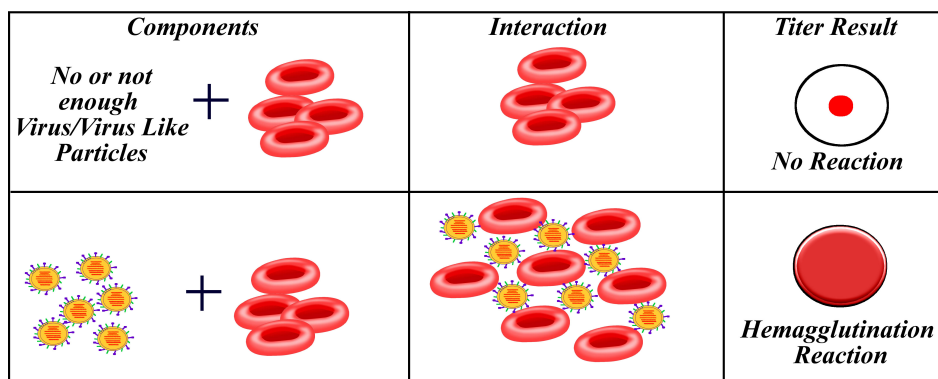


Figure 2.18: Schematic of hemagglutination reaction in 96-well plate. The top row indicates no reaction where the red blood cells precipitates at the bottom of the well in the absence of the virus. The bottom row shows that reaction occurs, where the viruses attach to the red blood cells and form a lattice. This results in a homogeneous color in the well [30].

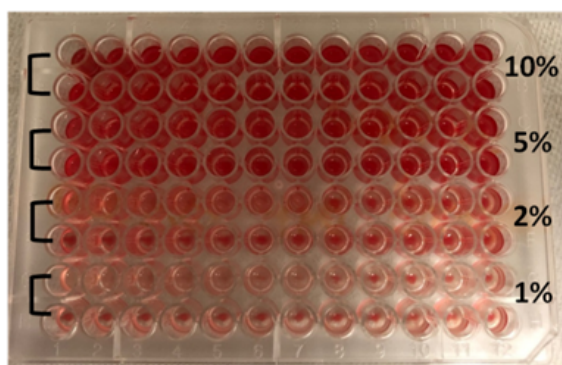


Figure 2.19: Photograph of the hemagglutination reaction in 96-well plate for various red blood cell (RBC) concentrations. The concentration of the 10% washed RBCs were diluted by phosphate buffer saline (PBS, 1X, pH=7.4). The cell concentration was adjusted to 10% in the top two rows, 5% in the 3rd and 4th rows, 2% for the 5th and 6th rows and 1% in the bottom two rows.

and tend to cause cross contamination due to the pipetting procedure. Moreover, the limit of detection of this assay is 2 units HA/50  $\mu$ l [103]. To eliminate these issues, we developed a droplet based microfluidic system to improve HA assay performance for virus quantification in Chapter 6.

### **Reversed-Phase High Performance Liquid Chromatography (RP-HPLC):**

This method includes a treatment with detergent to solubilize membrane proteins of viruses followed by a treatment with a reducing agent to break the disulfide bonds between HA1 and HA2 subunits. The method has been proven to be efficient for quantification of all the 16 HA subtypes from A and B strains of Influenza. However, its use is limited to the final vaccine formulation or purified materials such as virus-like particles [104].

### **Transmission Electron Microscopy (TEM):**

Electron microscopy is generally used to visualize size and morphology of virus particles. The major drawback of this method is the tedious sample preparation prior to imaging virus samples [104] as well as being open to interpretation.

### **Cytometer:**

The basic analytical principle behind a cytometer relies on fluorescence detection. The cytometer uses a non-virus specific dye, which stains proteins and nucleic acids of the sample. It is equipped with a software that quantifies intact virus particles. However, there have been a few studies with VLPs which requires further standardization [103].

### **Dynamic Light Scattering with Gold Nanoparticles (DLS with AuNP):**

Light scattering methods have been utilized to measure the size, aggregation and zeta potential of particles. In this method, viruses are conjugated on gold nanoparticles using antibodies. Then, the aggregation diameter of the target virus and the gold nanoparticles is measured by analyzing the absorbance of light. In this method, VLP quantification can be done [103].

## **2.7.3 Infectivity Measurement**

### **Plaque Assay:**

The plaque assay is used to determine infectivity of viruses. Infectivity is evaluated based on the ability of a virus to kill a target cell. In this assay, cells are infected with serial dilutions of the virus and incubated for 3 to 6 days. The cytopathic effect is then monitored

with a microscope and the plaques on the cell culture plate are counted. Based on the dilution and counted plaques, the plaque forming units can be determined. However, the quantification of VLPs has not been studied yet [103].

## Symbols and Nomenclature

$\rho$

$u$

$\eta$

$L$

$\partial u / \partial t$

$-\nabla P$

$\rho(u \nabla)u$

$\mu \nabla^2 u$

$\gamma$

$\Delta P, \Delta P_{nb}, \Delta P_{caps}, \Delta P_{body}$

PDMS

$\kappa$

$\beta_{slip}$

Hct

RNA

DNA

PB1

NP

NS1

FDA

HPV

BEVS

Re

Ca

UV

ETFE

HA

VLP

NA

# Chapter 3

## Material and Methods

In this section, the fabrication process of the microfluidic chip is first presented. Then, measurement setup for the projects, which is integrated with microfluidics chips, is explained.

### 3.1 Microfluidic Chip Fabrication

Fabrication of the micro-device includes photolithography and soft lithography processes. Photolithography was used to transfer computer aided designs (CADs) of the microfluidic chip onto silicon wafers. Soft lithography was used to replicate the designs on polydimethylsiloxane (PDMS). In photolithography, a negative resist (SU-8, MicroChem, MA, USA) was used, which is desired when high aspect ratio features are needed. Moreover, the SU-8 is durable to daylight, which is needed due to the soft lithography procedure. Schematic of the photolithography is given in Figure 3.1, while the steps are described below:

- SU-8 2005 was spin-coated onto a silicon wafer using a fluid dispenser (EFD Nordson Company, CA, USA) at 500 rpm for 30 s using a spinner (200 CB, Brewer Science, MO, USA). This layer is used as an adhesive layer for the top layer in Figure 3.1a.
- Coated wafers were exposed to soft bake, to crosslink the photoresist, at 65 °C, 95 °C and 65 °C for 2 min, 3 min and 2 min, respectively in Figure 3.1b.
- The wafer was exposed to the blind UV ( $\sim 300$  nm) exposure for 24 s (UV exposure machine, Newport, CA, USA) in Figure 3.1c.

- For further cross-linking, a second rapid heating step was applied at 65 °C, 95 °C and 65 °C for 1 min, 2 min and 1 min, respectively in Figure 3.1d.
- The second layer of photoresist (SU-8 2075 or SU-8 2025, negative photoresists, MicroChem, MA, USA) was spin-coated onto the wafer by using the fluid dispenser at 500 rpm for 30 s, followed by 3000 rpm for 35 s. Because different channel heights were desired for different projects, different thicknesses of photoresist were needed (60 and 40  $\mu\text{m}$ ). For SU-8 2025, the spin rate for 60  $\mu\text{m}$  was 2000 rpm, and for 40  $\mu\text{m}$  was 1850 rpm. However, in Chapter 6, the channel height was designed to be 80  $\mu\text{m}$ . Therefore, SU-8 2075 was coated on the wafer by using the same spinning parameters in Figure 3.1e.
- Heat was applied for soft baking at 65 °C, 95 °C and 65 °C for 4 min, 8 min and 2 min, respectively in Figure 3.1f.
- The wafer was illuminated with UV light using the UV exposure machine for 38 s with a photomask that includes the desired channel design. The photomask was designed via AutoCAD (Autodesk, CA, USA) and printed on Mylar film with 20K dpi resolution (CAD/Art services, CA, USA) in Figure 3.1g.
- After exposure, a hard bake was completed at 65 °C, 95 °C and 65 °C for 3 min, 7 min and 1 min, respectively in Figure 3.1h.
- To develop the sample and achieve the final design on the wafer, the wafer was immersed in a SU-8 developer (MicroChem, MA, USA) for 7 min. After the etching process, the wafer was washed with Isopropyl-alcohol (Sigma Aldrich, MO, USA) and dried with Nitrogen in Figure 3.1i.

The schematic of the second step (soft lithography) is given in Figure 3.2, and the fabrication steps are given in detail below:

- PDMS pre-polymer (w/w) (Sylgard 184, Dow Corning, Sigma Aldrich, MO, USA) was prepared in a mixture of 10:1 (base polymer: curing agent).
- Bubbles that occurred during the mixing of the polymer were removed by degassing using a vacuum oven (Isotemp Vacuum Oven Model 280 A, Fischer Scientific, NH, USA) (applied pressure was 25kPa for 30 min).
- PDMS was poured onto the silicon wafer and was incubated at 95 °C for at least 3 hours.



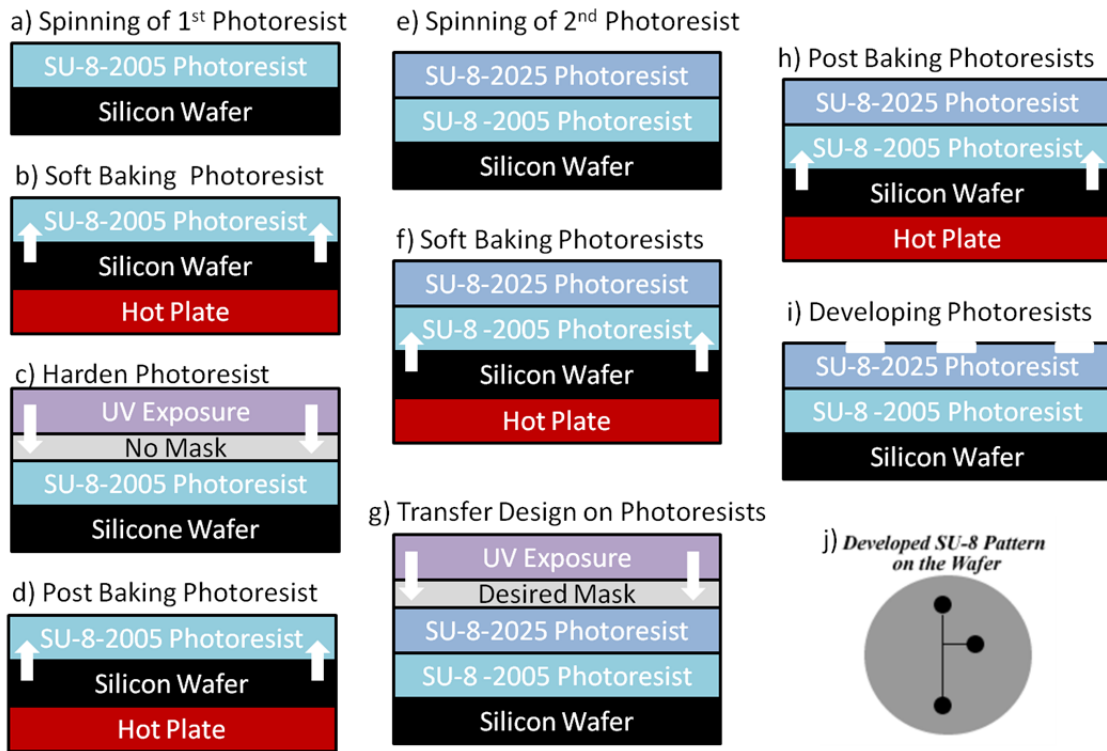


Figure 3.1: Schematics of photo-lithography steps for transferring CAD design (desired microfluidic device design) onto the silicon wafer. a) Spinning of the 1<sup>st</sup> photoresist, b) Soft-baking the photoresist, c) UV exposure (without a mask) to harden the photoresist, d) Post-baking the photoresist, e) Spinning a second layer of photoresist, f) Soft-baking step for the second resist, g) UV exposure with the mask to transfer microfluidic chip pattern, h) Post-baking for the second photoresist, i) Development of the exposed photoresist pattern, j) The final pattern transferred onto the Si wafer.

- After heating, PDMS was peeled off from the silicon wafer. Inlets and outlets for the channel were cut using a biopsy punch.
- To seal the channel, the PDMS microchannel was bonded onto a glass substrate, which was covered by a thin PDMS layer. To achieve bonding, the two substrates were exposed to oxygen plasma for 10 sec at 29.6 W at 500 mTorr using an Expanded Plasma Cleaner (PDC-001, Harrick Plasma, NY, USA). Since oxygen plasma changes hydrophobicity of PDMS, the bonded microchips were heated at 190 °C for 12 hours to reverse the effect.

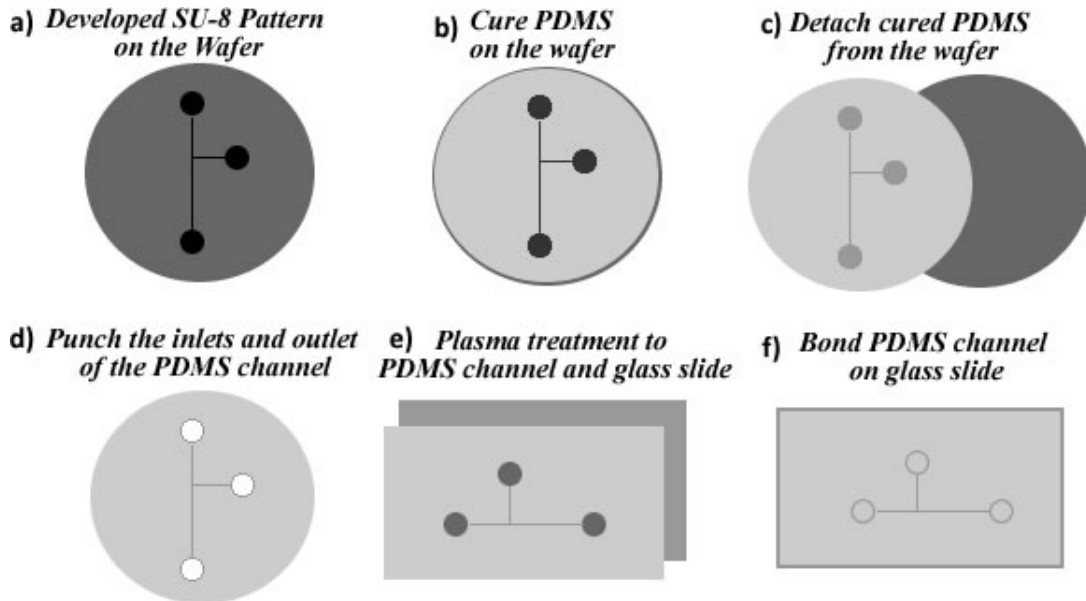


Figure 3.2: Schematic of PDMS casting steps and bonding. a) Developed photoresist on the silicon wafer, b) PDMS was poured on the silicon wafer and baked to cure the polymer, c) The cured PDMS was peeled off of the silicon wafer, d) The detached PDMS was punched from the inlets and outlets, e) A glass substrate and PDMS were exposed to oxygen plasma to activate the surfaces for bonding f) PDMS was bonded onto the glass slide.

## 3.2 Experimental Setup of the Microfluidic System

The experimental setup consists of several components, such as a microscope, flow sensor, microfluidic chips, a pressure system, and cameras, as shown in Figure 3.3. To visualize droplet flow in a microchannel, two different cameras were used. In the first project, where red blood cell droplet formation dynamics were analyzed, high resolution imaging was required to capture small changes during the formation. Thus, a high-speed camera (Phantom V210, Vision Research, NY, USA) was used to record videos and images of droplets. With a 12-bit digital image quality at 1280x800 full resolutions, the camera recorded images at 2190 frames per second (fps). To achieve ten kfps, the resolution and region of interest can be reduced. For low-frequency range droplet generation, an inverted epifluorescence microscope (Eclipse Ti, Nikon, Japan) was used. Images were recorded using a Retiga 2000R Fast 1394 monochrome CCD camera (Qimaging, AZ, USA). 4X and 60X objectives were coupled to the microscope. To control fluid flow inside the

microchannel, a pressure pump system (Fluigent, MFCS EZ, Germany) was used. The system had eight different programmable channels with a maximum of 1 achievable bar pressure in 40 ms per channel. Each channel outlet was connected to the fluid reservoir using ETFE (ethyltrifluoroethylene) tubing (IDEX, ON, Canada). The system pumps the fluids through the channel. The pressure system software was used to adjust the applied pressure level. Moreover, the flow sensor (SLG 1430-4870, Sensirion) was connected to the other end of the reservoir to measure the flow rate of the silicone oil during red blood cell droplet generation. The sensor measurement limit was  $40 \mu\text{l}/\text{min}$  with update rates of 100 Hz.

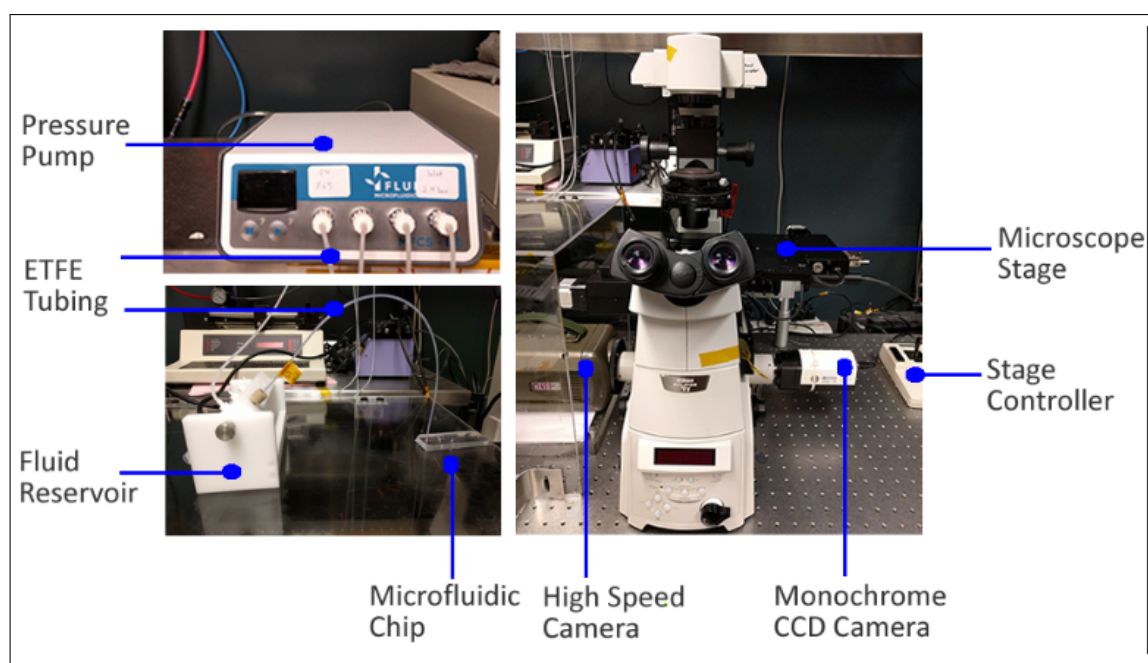


Figure 3.3: Experimental setup. Fluids were pumped into the microfluidic device using the pressure pump system (top left). The pressure pump creates air pressure that pumps the desired fluids from the reservoir (bottom left) to the microfluidic chip. A flow sensor is connected in between the reservoir and the microfluidic chip to measure the flow rate of fluids. The flow is recorded using a high speed camera or a CCD camera. Images were acquired using the microscope (right).

# Chapter 4

## Experimental Analysis of Droplet Formation of Red Blood Cells in a T-junction

In this project Merve Marcali (Ph.D. candidate, Department of Mechanical and Mechatronics Engineering) designed, fabricated, tested the microfluidic device performance, and conducted all the experiments and data analysis. Prof. Carolyn Ren (Department of Mechanical and Mechatronics Engineering, University of Waterloo) and Prof. Marc G. Aucoin (Department of Chemical Engineering, University of Waterloo) provided thoughtful discussions to accomplish the project.

### 4.1 Overview of Previous Works

Droplet-based microfluidic systems have shown great potential in a variety of applications involving chemical processes to biochemical analysis. This promise relies on the ability of these systems to produce monodisperse droplets of biological fluids such as cells, blood, saliva, and tear [91], [69], [1], [67], [58], [41], [116]. Producing monodisperse droplets is of great importance for these applications to eliminate batch-to-batch variability. Therefore, it is essential to understand if and how the droplet formation dynamics affect the final droplet volume. Several research groups have investigated droplet formation dynamics using both Newtonian and non-Newtonian fluids. Among these studies, the T-junction is the most common channel geometry used to form droplets. In this design, the channel

that carries the fluid destined to become the droplet (dispersed phase), is perpendicular to the channel that carries the continuous phase. As the dispersed phase flows into the main channel, forces created at the junction causes droplets to form [105]. This generator can work under three different generation regimes: squeezing, dripping, and jetting [16], [24], [40]. The regime is controlled by the capillary number, and the flow rate ratio of the phases. The monodispersity of droplets can only be achieved in the squeezing and dripping regimes, as mentioned in Chapter 2.

Formation of Newtonian fluid droplets in the dripping regime occurs in the range of  $0.02 < Ca < 0.3$ , and the dispersed phase can only penetrate a small distance in the main channel. Droplet break up is governed by the competition between surface tension forces, which resist formation, and the viscous drag forces, which act on the interface of the droplets. The final size of the droplet is defined at the point where the forces are balanced [34], [49], [17]. However, in the squeezing regime Newtonian-droplet break up occurs in the range of  $Ca < 0.02$ . Since the surface tension forces exceed the drag force, the interface between the dispersed and continuous phases penetrates the main channel, touches the far wall, and blocks the main channel [34], [17]. Formation of the droplet is governed by channel geometry.

In summary, depending on the generation regime, several parameters affect the formation of a droplet. In Figure 4.1, parameters that are investigated are presented in details.

The first group of parameters that affect droplet formation is related to the channel geometry and includes the dispersed phase channel width,  $w_d$ , and the continuous phase channel width,  $w_c$ . The main channel,  $w_m$ , which is the part where the dispersed and continuous phase intersect, is equal to  $w_c$ . Channel height is denoted as  $h$ .

The second group is related to the flow conditions. The flow rate in the main channel,  $Q_m$ , is the sum of the flow rates of the continuous phase,  $Q_c$  and dispersed phase,  $Q_d$ . Flow rates are controlled by the pressure pump, and the related pressures,  $P$ , follow the same subscript notation ( $c$ ,  $d$  and  $m$  for continuous, dispersed and main, respectively). By changing these parameters, the volume of the droplets,  $V_d$ , the droplet generation frequency,  $f$ , and the spacing between the droplets,  $\lambda$ , change. The droplet flow rate  $Q_{drop}$  is equal to the product of the droplet generation frequency and the droplet volume ( $Q_{drop} = V_d * f$ ), while the droplet velocity,  $u_d$ , is the product of the generation frequency and the spacing between droplets ( $u_d = \lambda * f$ ). Finally, the number of droplets can be obtained by the division of the main channel length,  $L_m$ , to droplet spacing ( $n = L_m / \lambda$ ).

To analyze the formation dynamics, these parameters are needed to evaluate the performance of the system. To simplify the analysis of the formation, the Buckingham  $\pi$  theorem has been used to reduce the parameters to six dimensionless numbers that are

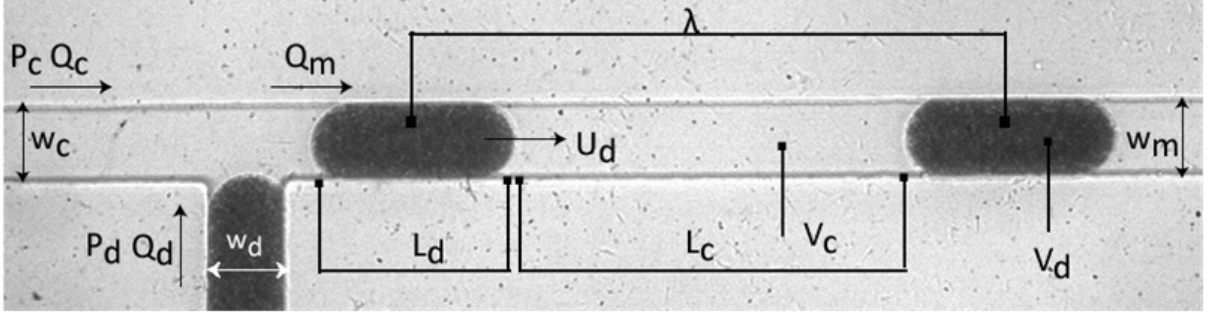


Figure 4.1: Microscope image of the generated droplets of red blood cells in a T-junction generator. Parameters affecting the droplet formation:  $P_c$ ,  $Q_c$ ,  $w_c$  are the continuous phase pressure, flow rate, and channel width, respectively.  $P_d$ ,  $Q_d$ ,  $w_d$  are the dispersed phase pressure, flow rate, and channel width, respectively.  $L_d$  is the length of the droplet,  $L_c$  is the length of the oil phase between droplets,  $u_d$  is the droplet speed,  $V_d$  is the droplet volume,  $\lambda$  is the spacing length between the droplets.  $Q_m$  and  $w_m$  are the main channel flow rate and channel width, respectively.

listed from Equation 4.1 to Equation 4.6 below [40]:

$$\varphi = Q_d/Q_c \quad (4.1)$$

$$\Lambda = w_d/w_c \quad (4.2)$$

$$h^* = h/w_c \quad (4.3)$$

$$\eta = \mu_d/\mu_c \quad (4.4)$$

$$Re = \rho Q_c/h\mu_c \quad (4.5)$$

$$Ca = Q_c\mu_c/\gamma hw_c \quad (4.6)$$

where  $\varphi$  is the flow rate ratio,  $\Lambda$  is the channel width ratio of the phases,  $h^*$  is the aspect ratio,  $\eta$  is the viscosity ratio,  $Ca$  is the capillary number, and  $Re$  is the Reynolds number. Since  $Re \ll 1$  in microfluidic channels,  $Re$  can be neglected. Then, the final dimensionless droplet volume becomes dependent on the remaining five dimensionless groups ( $V_d^* = f(\varphi, \eta, \Lambda, h^*, Ca)$ ). By using these dimensionless groups, several physical models have been developed to describe the final droplet volume. In the squeezing regime, where the formation of the droplet is governed by the channel geometry, Garstecki et al. described the droplet size of Newtonian fluid by the Equation 4.7 given below [34]:

$$L_d/w = 1 + aQ_d/Q_c \quad (4.7)$$

where  $L_d$  is the droplet length,  $w$  is the channel width,  $a$  is a geometric factor, and  $Q_d/Q_c$  is the flow rate ratio between the dispersed and the continuous phases. In the transition regime (in between squeezing and dripping regimes) where the droplet formation depends not only on the channel geometry but also on the capillary number, Christopher et al. showed that the Newtonian-droplet volume could be described by the Equation 4.8 given below [17]:

$$V_d^* = b^{*2} + \wedge Q_d/Q_c \quad (4.8)$$

where  $V_d^*$  is the dimensionless volume,  $b^*$  is the dimensionless penetration depth of the dispersed phase,  $\wedge$  is the channel width ratio, and  $Q_d/Q_c$  is the flow rate ratio of the two phases. Based on these two equations, one can see that the droplet formation in a T-junction is governed by the geometry of the generator and the flow conditions together.

For non-Newtonian fluids, Zhang et al. evaluated the dynamics of the droplet formation for a viscoelastic polyethylene oxide (PEO)-glycerol solution under three different generation regimes using both a T-junction and a flow-focusing generator [119], [25]. Using a similar dimensional analysis that was used in Newtonian fluids, it was found that the elasticity of the non-Newtonian fluids is also needed to calculate the final droplet volume and is described by Equation 4.9 given below:

$$L_d/W = 0.92(Q_c/Q_d)^{-0.22} C a_c^{-0.36} E l^{0.08} \quad (4.9)$$

PEO-glycerol or PEO-water mixtures are considered viscoelastic fluids where their viscosities are independent of shear rate. Furthermore, changing the PEO molecular weight does not change the solution viscosity. However, fluids that are non-Newtonian or have a time-dependent viscosity such as blood, tears, xanthan gum, and gellan gum have a dependence on the amplitude of shear stress or duration of shear stress. Therefore, it is expected to observe different formation dynamics with such fluids. For example, Rostami et al. investigated the droplet formation of a non-Newtonian fluid (xanthan gum solution) in a flow-focusing generator with a stadium-shaped cross sectioned glass channel for all three generation regimes (squeezing, dripping and jetting regimes). They showed that the role of the viscosity ratio, and the shear thinning property of the xanthan gum solution on the droplet volume is weak in both the squeezing and dripping regimes [83]. Using the same polymer solution, Gu and Liow et al. investigated the effect of the dispersed phase

angle and polymer concentration on the droplet formation dynamics in the jetting regime. They found that the angle does not change the formation dynamics, but the increased concentration of xanthan gum results in a more prolonged breakup of droplets [38]. In contrast to Rostami et al., Costa et al. used another non-Newtonian fluid. They generated gellan gum droplets in soybean oil under the three different regimes using a flow-focusing generator. They showed that droplet size not only depends on the flow rate ratio but also the viscosity of fluids and the interfacial tension of the different phases [20]. One can see that there are conflicting results in the literature. Furthermore, none of these studies presented a mathematical model to predict the final droplet volume with biological non-Newtonian fluids.

## 4.2 Introduction and Objective of the Project

The objective of this project was to investigate droplet formation dynamics of red blood cell solutions in a T-junction in the squeezing regime; and to predict and control the final droplet volume.

Although studies have investigated the mechanisms of non-Newtonian droplet formation in microfluidic channels with different geometries and under different generation regimes, none performed a comprehensive analysis involving all five dimensionless groups. To deepen our understanding of the dynamics of biological non-Newtonian droplet formation, a comprehensive analysis of the droplet formation using red blood cell solutions are presented in this chapter. In this analysis, the role of the width ratio ( $\Lambda = w_d/w_c$ ), aspect ratio ( $h^* = h/w_c$ ), flow rate ratio ( $\varphi = Q_d/Q_c$ ) and viscosity ratio ( $\eta = \mu_d/\mu_c$ ) on droplet formation was elucidated. Furthermore, the cell concentration ( $C_{cell}$ ) was used to alter the viscosity of the red blood cell solution.

To analyze the effects of these parameters on droplet formation, various conditions were tracked during the formation cycle such as the shape of the droplet, spacing between the droplets and production rate of the droplets. A formation cycle using Newtonian fluids consists of three major stages: the lag, filling and necking stages. The cycle begins with the lag stage, where the dispersed phase is pulled back into its channel after the previous droplet is pinched off, and re-flows back to the junction to form a new droplet. As the droplet comes to the intersection, it starts to penetrate the main channel and reaches the maximum penetration depth, and a neck begins to form. During this time, the continuous phase bypasses the droplet and constructs the spacing between the droplets. Then necking of the droplet starts because the continuous phase pushes the interface to collapse due to the pressure build-up at the junction. At the same time, the dispersed phase continues



to grow and reaches the far wall. In the end, the neck reaches its critical thickness, collapse accelerates, and the droplet pinches off. The cycle repeats, starting from the lag stage again [109]. However, in non-Newtonian fluids, another stage has been recorded. The stretching stage is when the elongation of the non-Newtonian fluid occurs before the droplet is pinched off [49], [119]. Our experimental studies presented different stages than the other non-Newtonian fluid studies, details are given in the results section.

In this study, a squeezing regime was preferred to isolate the effects of the viscous drag force and the shear thinning property of the red blood cell solution during droplet generation. Although the generation is only governed by channel geometry in the squeezing regime for Newtonian fluids, experimental results suggested that droplet formation depended on not only channel geometry, but also capillary number, flow rate ratio and viscosity ratio of the fluids in the presence of biological non-Newtonian fluids (red blood cells). Furthermore, in previous works on non-Newtonian fluids, isolated droplets were generated where the droplets did not confine the entire cross-section of the microchannel. However, it has been shown that the speed of the plug-like droplets in the main channel and the pressure at the junction change due to the flow of the carrier fluid from the gutter regions. This change results in variations in the flow field at the junction [32]. Therefore, to compare the formation dynamics of a non-Newtonian fluid with Newtonian fluids, only plug-like droplets were analyzed in this study.

## 4.3 Design of Experiment

The design of this experimental study was done by varying parameters affecting droplet formation such as width ratio, aspect ratio, cell concentration, flow rate ratio and viscosity ratio. Conditions for each experimental setup are listed in Table 4.1. In Table 4.2, the physical properties of the fluids were given.

### 4.3.1 Material And Methods

To evaluate the droplet formation response to geometrical differences, the channel height and the channel width of the dispersed phase were adjusted. For all the experimental sets, the channel width of the main channel was kept constant around  $100 \mu\text{m}$ , and the dispersed phase width was set to two different values,  $\sim 50 \mu\text{m}$  and  $\sim 100 \mu\text{m}$ , corresponding to  $\Lambda=0.5$ , and 1, respectively. Garstecki et al. showed that droplets could not form at  $\Lambda=0.2$  (1:5 ratio) in the squeezing regime and determined the minimum ratio as 1:3 [34]. In

addition, two different channel heights were fabricated:  $\sim 60 \mu\text{m}$  and  $\sim 40 \mu\text{m}$ . This corresponds to aspect ratios,  $h^*$ , of 0.6 and 0.4, respectively.

Exp. No	$\mu\text{c}$	$C_{\text{Cell}}$	$h^*$	$\Lambda^*$
1 - 4	100 mPa.s	100 %	0.6, 0.4	1, 0.5
5 - 8	50 mPa.s	100 %	0.6, 0.4	1, 0.5
9 - 12	10 mPa.s	100 %	0.6, 0.4	1, 0.5
13	100 mPa.s	45 %	0.6	1

Table 4.1: List of conditions for each experimental case study. Overall there were 13 different experiments. Among these experiments, only diluted red blood cell sample (45% RBCs) were tested using one silicone oil type (100 mPa.s) and one geometrical design ( $h^*=0.6$ ,  $\Lambda=1$ ) (see experiment number 13)

Continuous Phase		Dispersed Phase	
Silicone Oil	Viscosity (mPa.s)	Chicken-Red Blood Cell Concentration	Effective Viscosity (mPa.s)
	100	100 %	$\sim 8-10$
	50	45 %	$\sim 6-9$
Interfacial Tension (mN/m)		$15.117 \pm 0.01$	

Table 4.2: Physical properties of the dispersed and continuous phases. Viscosity of the red blood cells was adopted from the literature for both cell concentration values [29], [26]. The interfacial tension of red blood cells with the silicone oil was measured using a Wilhemy plate tensiometer (Data Physics, DCAT 11, Germany).

### The Continuous Phase

In this study, silicone oil (DC200, Sigma Aldrich, MO, USA) was used as a continuous phase. Since red blood cells adhere to the surface of the PDMS channel, surface treatment was needed. Among the other surface treatment methods available, such as the use of perfluorinated solutions, silicone oil presented itself as the simplest and the most effective solution to eliminate cell adhesion. Silicone oil was preferred as a carrier oil as well. However, it should be noted that after the treatment, PDMS swells, which causes a change

in channel height and width. Therefore, channel dimensions were measured carefully before running experiments. As shown in Tables 4.1 and 4.2, experiments were done using three different viscosities of silicone oil (10, 50 and 100 mPa.s) to analyze the effect of the viscous drag force on the emerging interface of the shear-thinning fluid (red blood cell solution).

### **The Dispersed Phase**

Solutions of red blood cells (Rockland, Chicken RBC %10 washed cell,  $1.20 \times 10^6$  cells/ml, USA) were used as a dispersed phase. Washing procedure was done by the supplier. As shown in Table 4.2, different cell concentrations were used in experiments to alter the viscosity of the dispersed phase. The shear-thinning behavior of red blood cells is mostly related to a rouleaux formation of red blood cells [79]. As the red blood cell solution is exposed to shear stress, cells start to clump together and form the rouleaux, which causes a change in the viscosity of the solution. The number of red blood cells was defined as a hematocrit level ( $Hct = C_{cell} = \text{Cell concentration}$ ), and it has been shown that as the Hct level decreases, the viscosity of the red blood cell solution decreases [28], [79]. Viscosities for specific cell concentrations were adopted from the literature and presented in Table 4.2 [29]. Due to the shear-thinning property, the viscosity of red blood cell solutions were given as ranges. These ranges were determined by applying shear from 0 to 3000 1/s. The cell concentration of the dispersed phase was varied from 100% to 0% i.e. blood plasma. Dilution of the chicken red blood cell was done with phosphate buffer solution (PBS 1x, pH=7.4, Sigma Aldrich) and pH was kept constant for each dilution. Since blood samples were stored in EDTA (ethylenediaminetetraacetic acid) tubes at 4° C before its dilution with the buffer solution, cell coagulation was prevented. Then, Hct level of the final mixtures were measured using a hemocytometer (Countess II F1, Life Technologies, ThermoFisher Scientific, MA, USA). In addition, cell deformability changes the rouleaux formation, which results in a change in the viscosity of the sample as well [4], [29]. Therefore to have consistent cell deformability for a single experimental set, fresh samples were used. It is essential to mention that, due to the Fahraeus-Lindqvist effect [4], the number of cells in the droplet did not reflect the same number of cells that were prepared in the bulk solution. Therefore, the concentration of the cells in the droplets was labeled relative to each other.

### **Interfacial Tension**

Interfacial tension of the silicone oil with the red blood cells was measured using the Wilhemy plate method (Data Physics DCAT 11, Germany), and shown in Table 4.2.

## Surfactant

In this project, a surfactant was not added to either phases so that uniform interfacial tension can be achieved throughout the droplet formation process, which also simplifies the analysis due to the absence of dynamic mass transport of surfactant molecules to the emerging interface of the droplet.

## Global Network Design and Design Criteria

The microfluidic channel design is presented in Figure 4.2. The length of the dispersed and the continuous phase channels are equal (1 cm), and the main channel length is 5 cm. The channel was designed based on the design criteria reported by Glawdel et al. [36]. The study showed that the performance of the droplet generation was affected by the channel design. For example, the main channel length should be long enough so that the overall flow in the system does not fluctuate when one droplet enters and exits the system. However, it should also be short enough so that the pressure system can provide enough pressure to drive the flow.

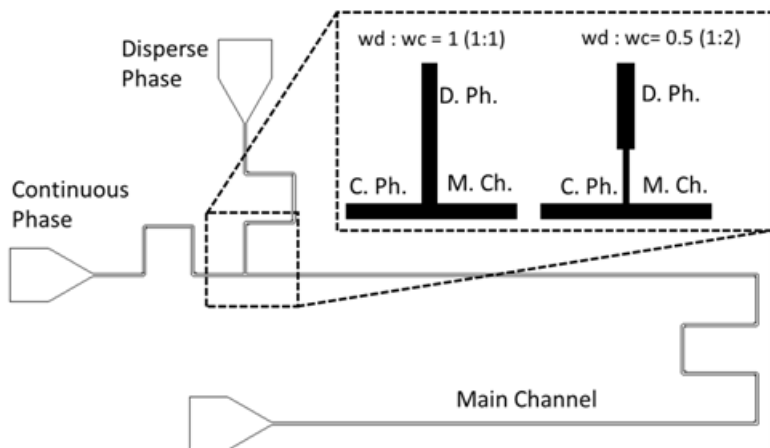


Figure 4.2: Schematic of the overall microfluidic device design. The design consists of one dispersed phase, one continuous phase and a main channel. To generate droplets, a T-junction generator was used. At the junction, we used two dispersed phase channel widths. The left side of the enlarged figure represents a wider dispersed phase channel width, and the right side of the enlarged figure represents a narrow dispersed phase channel width.

## Channel Dimension Measurement

To measure the droplet volume accurately, channel dimensions need to be measured precisely. PDMS swells due to the surface treatment with silicon oil. As a result, the channel dimensions vary from the original dimensions. To measure the dimensions, flow sensors and pressure systems were used to measure the hydrodynamic resistance of the network. Since hydrodynamic resistances are a result of channel dimensions, channel height can be calculated by applying the 1-D hydrodynamic model for pressure-driven flow. The dispersed phase was plugged with a metal tip to eliminate incoming flow (red cross in Figure 4.3). Next, the flow of silicone oil was applied only from the continuous phase. After a certain pressure was applied, the flow rate of the silicone oil was recorded by the flow sensor, and the hydrodynamic resistance,  $R_{hyd}$ , was calculated by Equation 4.10:

$$R_{hyd} = P/Q \quad (4.10)$$

By applying circuit analysis, one can conclude that  $R_{hyd}$  is the sum of two serial resistances, as shown in Figure 4.3.

$$R_{hyd} = R_m + R_c \quad (4.11)$$

For a rectangular microchannel operating under laminar flow conditions that has  $h < w$ ,  $R_{hyd}$  can be calculated from the following Equation 4.12 [13]:

$$R_{hyd} = \frac{12\mu L}{wh^3} \quad (4.12)$$

where the channel width,  $w$ , was measured from the microscope image of the T-junction intersection and length,  $L$  was already known to form the design. By substituting the pressure and flow rate values into the given Equation 4.10 above,  $R_{hyd}$  was calculated. Once  $R_{hyd}$  was measured,  $h$ , channel height could be calculated. This measurement was done for each experimental set due to the variation in channel dimensions.

### 4.3.2 Experimental Setup

The microfluidic chip was mounted on the microscope, and the desired fluids were connected to the chip via tubing (ETFE, ethyltrifluoroethylene, IDEX, WA, USA). By using the Fluigent pressure system (Germany), constant fluid flow was provided to the microchannel.

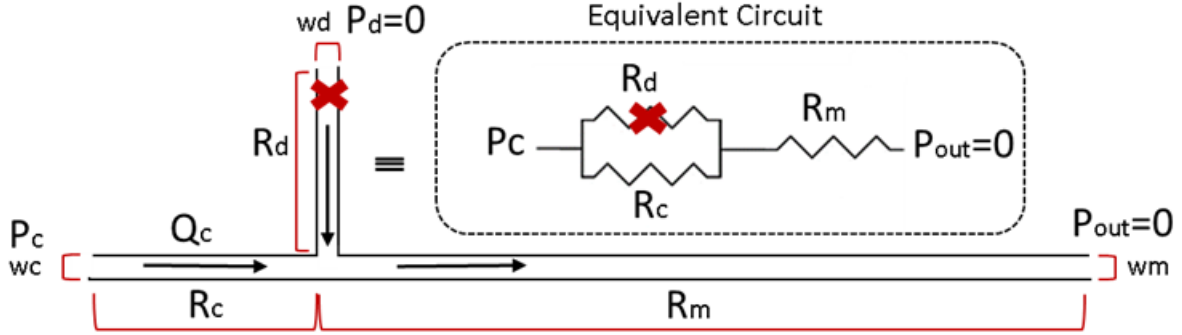


Figure 4.3: Schematic of the equivalent electrical circuit of the microfluidic chip design. The circuit was utilized to calculate the hydrodynamic resistances of the channels and the channel height. In this case, the dispersed phase channel was plugged to prevent incoming flow into the channel. Then, silicone oil was flushed into the device from the continuous phase through the outlet, and flow rate of the silicone oil was measured using a flow sensor. Finally, hydrodynamic resistances of the two serially connected channels ( $R_c$  and  $R_m$ ) were calculated using the flow rate data and Equations 4.10, 4.12 which also give channel height information.

As the droplets were generated, the high-speed camera recorded videos for each set of experiments. Each experiments were done in room temperature, 24 °C. To span a range of capillary numbers, the pressure of the fluids was adjusted to various levels. At each level, the pressure of the dispersed phase was adjusted to change the flow rate ratio, hence, droplet sizes. The minimum pressure limit was the pressure that allowed an isolated droplet to form or the pressure which resulted in the flow sensor reading  $0.5 \mu\text{l}/\text{min}$ . The maximum pressure limit was the pressure at which large droplets merged once formed or 1050 mBar. Droplet formation was recorded three minutes after setting the pressure to eliminate fluctuations in the system.

### 4.3.3 Experimental Procedure

First, the flow sensor was calibrated for three silicone oil viscosities. Details of the calibration were given in Appendix B. Then, the interfacial tension measurement of the desired fluids was done using the tensiometer (Data Physics, DCAT11, Germany). By utilizing the data of these measurements, a microfluidic device was designed. Then, the microfluidic chips were fabricated using the procedure described in Chapter 3.1. Before the experiment,

the fabricated microfluidic chips were flushed with the desired silicone oil type and were baked at 120° C overnight. During the experiments, the microfluidic chip was connected to the pressure system at one end, and to the flow sensor on the other end. Silicone oil was flushed into the channel for 10 minutes before the droplet generation to eliminate PDMS channel wall expansion which causes channel height variations. The chips were also inspected for dust or any clogs. 10 minutes after flushing the system with silicone oil, the channel dimensions were measured. Then, the dispersed phase fluid was connected to the pressure system, and pressures of both fluids were adjusted to form droplets. Formation of droplets was recorded using a high speed camera (Phantom V210, Vision Research, NY, USA), and videos were edited by using MATLAB (MathWorks, MA, USA) image processing tools to capture 5 to 10 droplets. Recorded videos were analyzed using a custom image analysis program. Details of the program are given in the next section. This procedure was repeated for all new configurations.

#### 4.3.4 Video Analysis

##### **Droplet Shape, Size and Volume Calculation using Image analysis**

Analysis of droplet volume, size and shape were done using a custom image analysis program in MATLAB (MathWorks, MA, USA). In the analysis, the direction of a moving droplet was adjusted such that droplets flow from the top to the bottom of the recorded image and the T-junction was located on the right side of the image, as shown in Figure 4.4. The microfluidic chips were mounted on the microscope by considering this orientation to be consistent. In each video, the region of interest was cropped and recorded as an image. Then, the cropped images were filtered by using the median and Weiner filters to eliminate the noise before the images were turned into binary image (Black and White Image). Threshold binning was applied to eliminate dark spots in the gray scale image that were not attributed to the droplet of red blood cell solution. The edge of the droplet was detected by an edge detection function. To differentiate the dispersed phase from the droplet, the objects that were enclosed by the boundary (droplets) were filled with a white color. Labelling function was used to discriminate two droplets in case two droplets appear in the same frame. The function selects the droplet that is closer to the T-junction. The final product of this procedure was the droplet of interest. By analyzing the boundary information of the labelled droplet, the length and width of the droplet were calculated, which were utilized to calculate the volume of the droplet. In this study, it was assumed that the out of plane curvature of the droplet was equal to the half the channel depth ( $r \approx h/2$ ) and the volume calculation was done using Van Steijn model in given Equation

5.2 below [109]:

$$V = hA - h^2/2(1 - \pi/4)l \quad (4.13)$$

where  $V$  is the volume of the droplet,  $h$  the channel height,  $l$  the perimeter of the droplet, and  $A$  the 2D top-view area of the droplet.

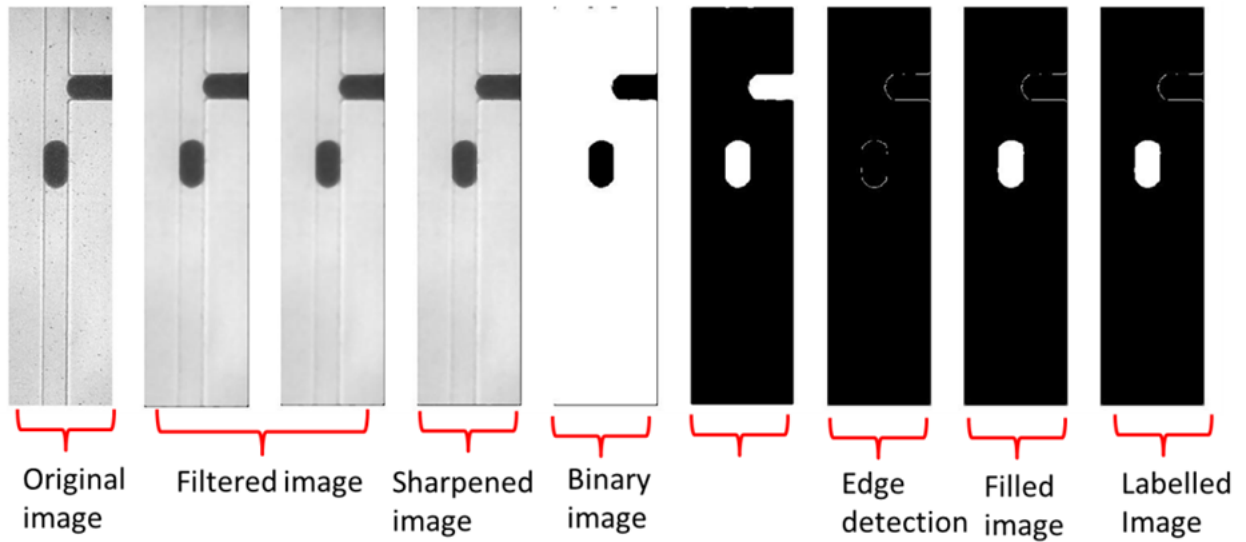


Figure 4.4: Sequence of image processing for a single droplet image. First, a video of the droplet formation was recorded using a high-speed camera. Then, each frame of the recorded video was cropped to be analyzed. The cropped images were filtered to eliminate noise using median and Weiner filters. The filtered images were sharpened to highlight the boundary of the droplets. Then, the sharpened images were converted into binary images (Black and white image). The edge of the droplet was defined by using edge detection function to differentiate the droplet from the dispersed phase and enclosed object (droplet) was labelled with white color. Finally, the droplets were labelled in different colors to eliminate double processing in case two droplets are captured in a single frame. By doing this only the droplet closer to the junction was analyzed.



## **Droplet Speed, Frequency and Spacing Calculation using Image Analysis**

In the calculation of speed, frequency and spacing, only the top droplet that was closest to the junction was used. First, the position of the top droplet was determined. Displacement of this droplet was calculated and compared with the median value of the droplet frame by frame so that any erroneous droplet identification was eliminated. To calculate generation frequency, a detection point was determined in the y-direction. Then by measuring the time it takes between the droplets passing the detection point, the generation frequency was calculated. The speed of the droplet was calculated by dividing the displacement between frames to the frame rate. The spacing between droplets ( $\lambda$ ) was calculated by multiplying the generation frequency ( $f$ ) to the droplet speed ( $\lambda = u_d \cdot f$ ). Moreover, the flow rate of the dispersed phase was calculated by the product of the generation frequency and the droplet volume ( $Q_d = V_d \cdot f$ ). All these data were averaged for the number of droplets in each video, and the standard deviation was less than 3%.

## **Penetration Depth and Neck Thickness Calculation using Image Analysis**

By tracking the farthest point that the dispersed phase reached in the main channel, penetration depth was calculated. The neck thickness of the droplet was calculated by tracking the farthest point of the droplet from the opposite inner corner of the junction at a 45° angle.

## **Data Output**

All the information was obtained from the image analysis was outputted to an excel file that includes the microfluidic channel geometry, fluid properties, applied pressures, flow rates, droplet dimensions, generation frequencies, the spacing between droplets, penetration depths and neck thicknesses. All the non-dimensional analysis was computed using the information in this output file.

# **4.4 Results and Discussions**

## **4.4.1 Dynamics of Red Blood Cell Droplet Formation**

In contrast to the studies of non-Newtonian fluids, the high-speed video evidence suggested that the droplet formation process of red blood cells consisted of only three major stages

similar to Newtonian fluids, as shown in Figure 4.5.

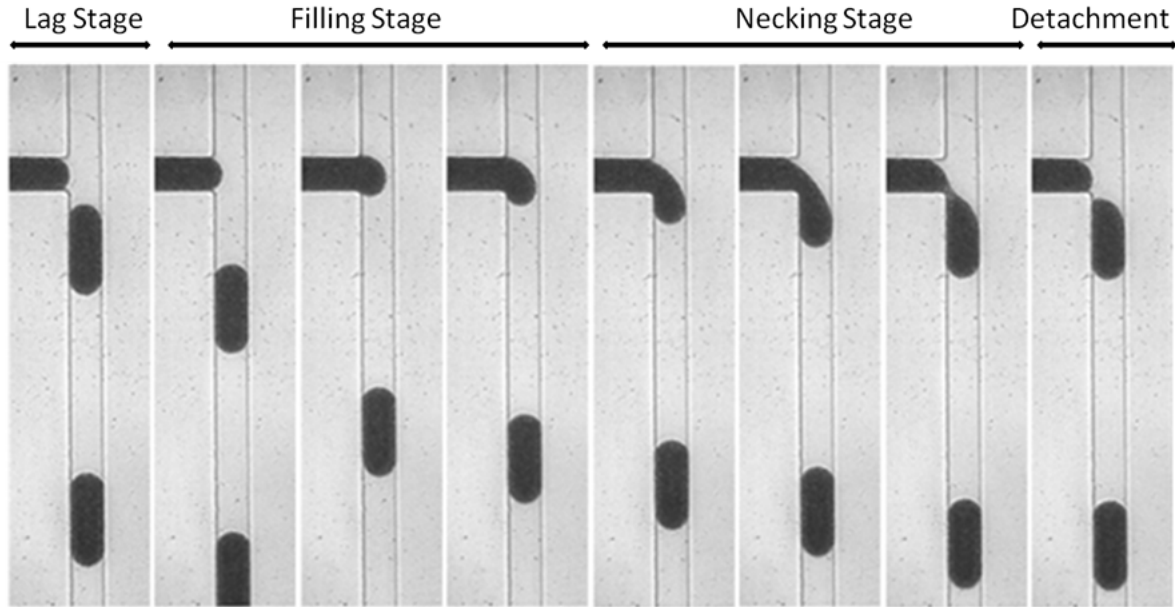


Figure 4.5: Microscopic images of a single formation cycle of red blood cells droplets in a T-junction generator under the squeezing regime. The cycle consists of three stages: lag, filling and necking stages. After these three stages, a detachment of the droplet occurs.

To demonstrate a broad overview of droplet formation, 6 cases were selected from the 13 experimental conditions as shown in Figure 4.6. Each case was selected such that when compared to case A, a single parameter was effectively changed. For instance, case A and case B are demonstrative of the influence of the width ratio on droplet formation. On the other hand, case A and case C show the effect of the aspect ratio on droplet formation, and so on. Although cases have a unique combination, all cases presented an identical formation cycle where the formation process could be divided into three stages: the lag, filling, and necking stages. Each stage was investigated in detail. To follow the analysis better, it is suggested that readers refer to Figures 4.6 and 4.7 for the following sections.

Similar to Newtonian fluids, each cycle started with an injection of the dispersed phase into the main channel. Then, the interface of the dispersed phase reached its maximum penetration depth,  $b_{fill}$  (square in Figure 4.7a, Figure 4.7b), while the continuous phase bypassed the interface constructing a gap between droplets. At the same time, the neck thickness of the droplet increased and reached a plateau. The neck thickness is the  $45^\circ$

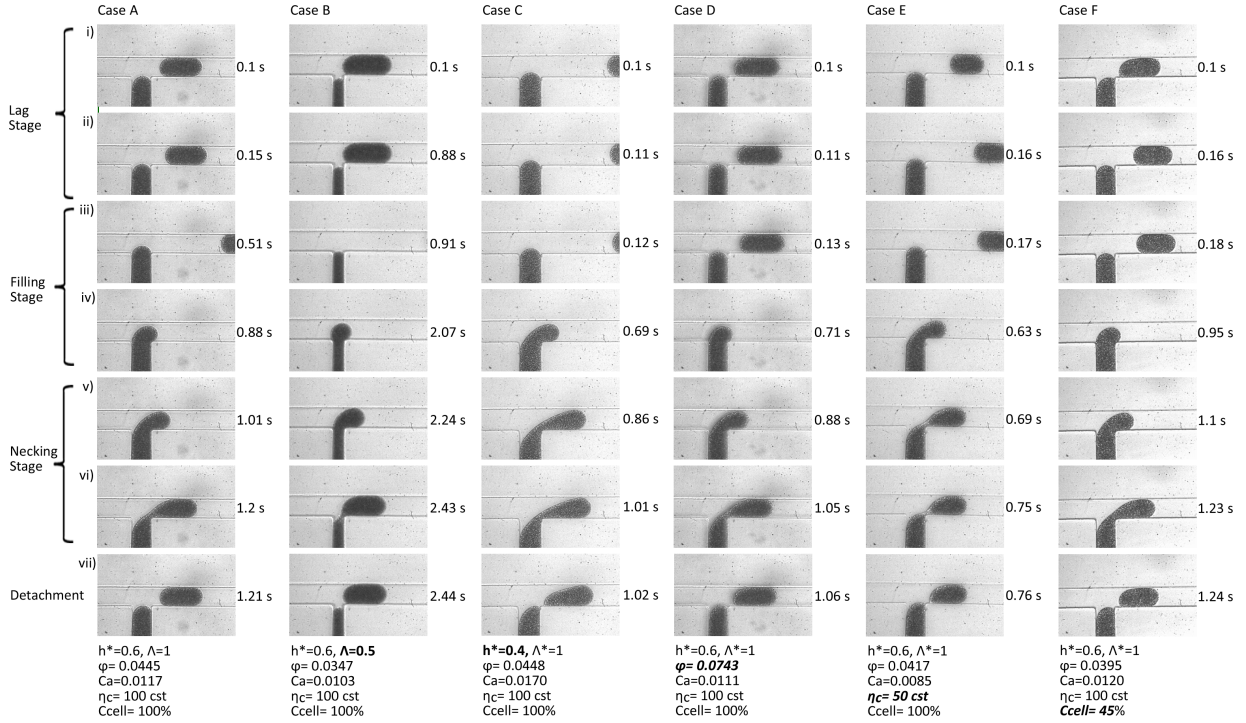


Figure 4.6: High-speed camera images of an individual droplet formation cycle for six different cases. Droplet formation with non-Newtonian fluid (red blood cell solution) consists of three stages: lag, filling, and necking stages. Each case was differentiated from case A in terms of channel dimensions and fluid properties (detailed parameters of each case were given under each figure). Droplet volume, spacing between droplets and generation frequency were different in each case showing the impact of the listed parameters on a formation cycle.

distance between the right corner of the T-junction to the back half of the droplet and is defined as  $2r_n$  (triangle in Figure 4.7a, Figure 4.7b). As pressure built up due to the obstruction of the continuous phase, the necking stage began, and neck thickness started to decrease. While the neck of the droplet was collapsing, the dispersed phase continued to be pumped into the droplet. Once the droplet touched the far channel wall, the penetration depth is redefined as the penetration depth at pinch-off,  $b_{pinch}$  (see Figure 4.7a), necking accelerated, and the droplet pinched off. The neck thickness at this point is defined as  $2r_{pinch}$  (see Figure 4.7a). All these variables were converted into non-dimensional form by dividing all lengths by  $w_c$ , all volumes by  $w_c^2h$ , and time by the period of formation ( $t/\text{period}$ ). As shown in Figure 4.7a, depending on the channel geometry and the flow

conditions, these variables presented different characteristic features. For example, the lag stage lasted longer for narrower dispersed phase channel designs (Case B). A more detailed analysis of these variables is discussed in the next section.

## Lag Stage

For  $\Lambda=0.5$ , the lag stage was very similar to what has been seen for Newtonian fluids. The emerging dispersed phase receded into its originating channel following the detachment from the released droplet; followed by the dispersed phase pushing back into the junction to form a new droplet (see Figure 4.6, Case B). In systems with a wider dispersed phase channel, the interface of the emerging droplet pinned at the entrance of the junction after the previous droplet detachment.

Glawdel et al. showed that the lag stage generally represents 2-10% of the formation cycle, which affects the spacing between the droplets and has no role in the final droplet volume [36]. In this study, the lag stage represented 20-35% of the formation cycle, as shown in Figure 4.6, and the duration of the stage increased with a narrower dispersed phase channel (see Figure 4.7, Case B). In some cases the lag distance was immeasurable, i.e.,  $\sim 1\text{-}2\ \mu\text{m}$ , whereas for experiments with  $\Lambda=0.5$ , the lag distance was generally  $\sim 8\text{-}18\ \mu\text{m}$ . Thus, a smaller dispersed phase channel width was associated with longer lag distances and the lag stage. All 12 cases were analyzed to confirm this analysis, and all experimental sets with narrower dispersed phase channel had longer lag distances and a longer lag stage (Figure 4.8). The duration of this stage was mostly governed by the width ratio. As shown in Figure 4.8, width ratio was the parameter that created a significant difference on duration compared to other dimensionless parameters such as aspect ratio, cell concentration and the viscosity ratio of the fluids. Hence, it was concluded that the lag stage was governed by only the width ratio of the channel. In addition, similar to Newtonian fluids, this stage did not play a significant role in the final droplet volume (details are given in Chapter 5). However, the spacing between droplets was larger in the presence of the narrower dispersed channels, as shown in the Figure 4.12c.

## Filling Stage

In this stage, the dispersed phase penetrated into the main channel and progressed to the far wall. As the droplet grew, the gap between the interface and the outer wall narrowed. The neck thickness ( $2r_n^*$ , triangle, see Figure 4.7b) increased for all cases and reached a plateau as the dispersed phase filled the main channel. The filling stage ended when the

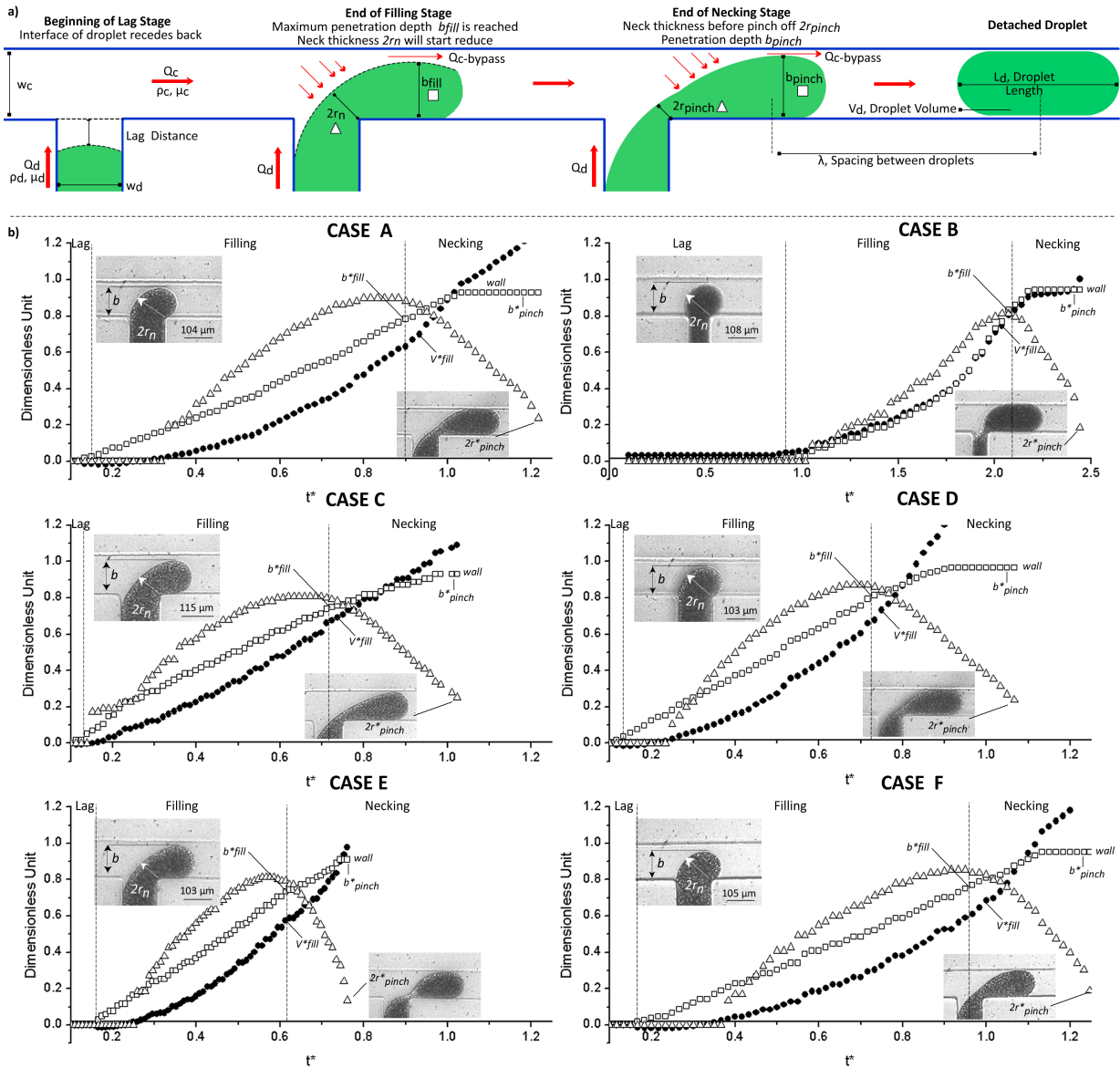


Figure 4.7: a) Schematic of the critical points of the three stages of a droplet formation cycle in the T-junction with analyzed dimensionless variables ( $L_{lag}$ ,  $b_{fill}$ ,  $b_{pinch}$ ,  $V_{fill}$ ,  $2r_n$ ,  $2r_{pinch}$ ), and b) Evolution of droplets with respect to time for six representative cases and the dynamic changes of the dimensionless variables (Droplet volume ( $V_d^*$ , circle), penetration depth ( $b_{fill}^*$ , square), and neck thickness ( $2r_n^*$ , triangle)) over time.

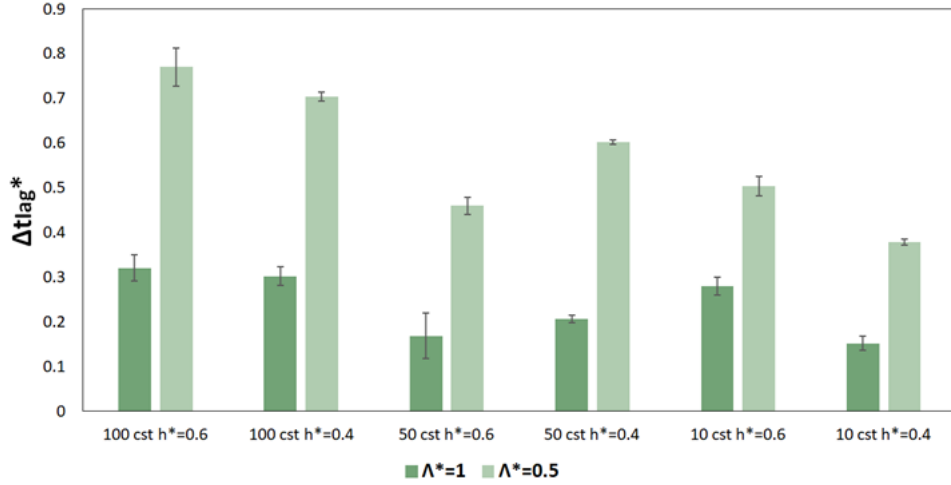


Figure 4.8: Bar plot of the duration of the lag stage for all experimental cases. Duration of lag stage was governed by the width ratio ( $\Lambda$ ) of the channels and other dimensionless parameters ( $h^*$  and  $\eta$ ) became less effective. As the width ratio decreased ( $\Lambda=1$  to  $0.5$ ), the lag duration increased due to the receding of the dispersed phase into the channel.

maximum neck thickness ( $2r_n^*$ , triangle, see Figure 4.7b) was reached. In a prior study using Newtonian fluids, manipulating the channel height and width resulted in a significant difference in the penetration depth [36]. In our study, to examine the dimensionless parameters individually, an additional experiment allowed the effect to be attributed to either the channel height or width.

Contrary to what has been previously reported,  $b_{fill}^*$  did not vary as extensively for all cases (0.69 to 0.78) under the same flow conditions except the experiments with 10 mPa.s silicone oil where the penetration depth reached the highest point (0.80-0.90) (see, Figure 4.11a). Furthermore, the penetration depth was mostly affected by the aspect ratio rather than the width ratio. As the aspect ratio reduced, the penetration depth decreased for all experiments.

For Newtonian systems, the final penetration depth is reached when the capillary force and the drag force acting on the dispersed phase are balanced, and a characteristic shape appears [109]. In our system, a similar characteristic shape was achieved: a half-circle at the front of the droplets with diameter  $b_{fill}^*$ , and a quarter circle or a circular segment at the back half of the droplet (see Figure 4.7a). The emerging droplet volume ( $V_{fill}^*$ ) during the filling stage was calculated using this characteristic shape; hence, a linear correlation between the  $b_{fill}^*$  and  $V_{fill}^*$  was expected. Our analysis showed that larger  $b_{fill}^*$  resulted

in larger  $V_{fill}^*$  as shown in Figure 4.11b.

Higher viscosity oil resulted in similar  $V_{fill}^*$  values (0.48-0.62), whereas for low viscosity oil i.e. 10 mPa.s silicone oil,  $V_{fill}^*$  values were distinctly higher (0.63-0.73). It should also be noted that the effect of the channel height on the final droplet volume may be confounded in this analysis, given that the dimensionless filling volume is the result of dividing the filling volume by the channel height (thus making the dimensionless filling volume larger). Similar analysis effects were highlighted by others [113].

Similar to what is observed for Newtonian fluids, the duration of the filling stage represented the largest portion of the formation cycle (from 40% to 55%). However, compared to other non-Newtonian fluid, a longer filling stage was observed in our study [85]. As shown in Figure 4.9, the length of the filling stage varied in all twelve cases. Among all the dimensionless parameters, the width ratio ( $\Lambda$ ) was found to affect the filling stage the most. As the width ratio decreased, the duration of the filling stage increased (Figure 4.9).

On the other hand, oil viscosity, cell concentration, and aspect ratio had limited impact on the filling duration. Lower oil viscosities and higher aspect ratios represented shorter filling stages. This stage was a function of both geometrical and flow conditions of the system.

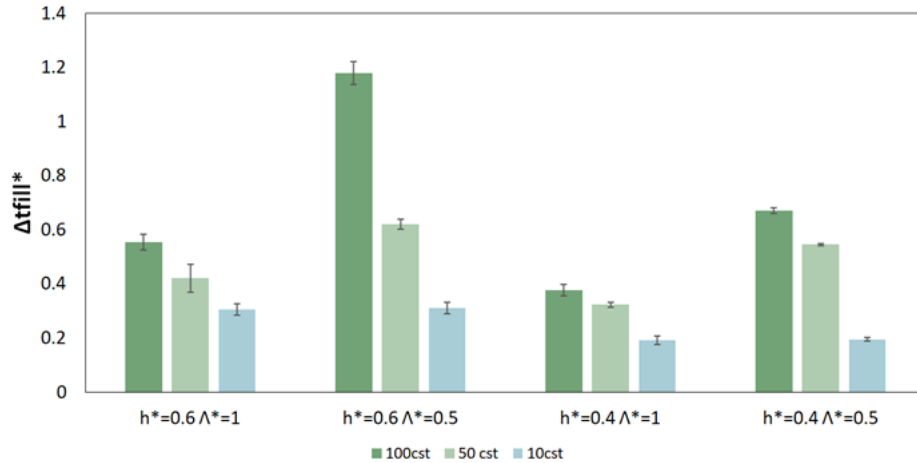


Figure 4.9: Bar plot of the duration of the filling stage for all experimental cases. Duration of the filling stage was mostly governed by the width ratio ( $\Lambda$ ) of the channels and other dimensionless parameters ( $h^*$  and  $\eta$ ) had limited impact on the duration. As the width ratio was decreased, the duration of the filling stage increased. However, as the oil viscosity or the aspect ratio was decreased, the duration of this stage decreased.

## Necking Stage

The necking stage was the last part of the formation cycle seen for all conditions. In this stage, the droplet volume continued to increase at a linear rate as it penetrated into the main channel. As the droplet grew, the penetration depth continued to increase ( $b_{fill}^*$ , circle, see Figure 4.7a,b) and the neck thickness reduced and reached a critical size, ( $2r_{pinch}^*$ , triangle, see Figure 4.7a,b) where the droplet pinches off suddenly. This stage was shorter than what has been previously reported for Newtonian fluids, making up only 15-25% of the formation cycle. Furthermore, no stretching of the dispersed phase into the main channel was observed before pinch-off like in other non-Newtonian fluids. As shown in Figure 4.7b, all cases indicated similar necking time except, Case E, where the oil viscosity was reduced to 50 mPa.s. Therefore the necking stage has some dependence on the viscosity of the continuous phase. As the oil viscosity was reduced, the duration of the necking stage also reduced (Figure 4.10). Furthermore, the analysis showed that aspect ratio, cell concentration, and width ratio had no impact on the duration of the necking stage.

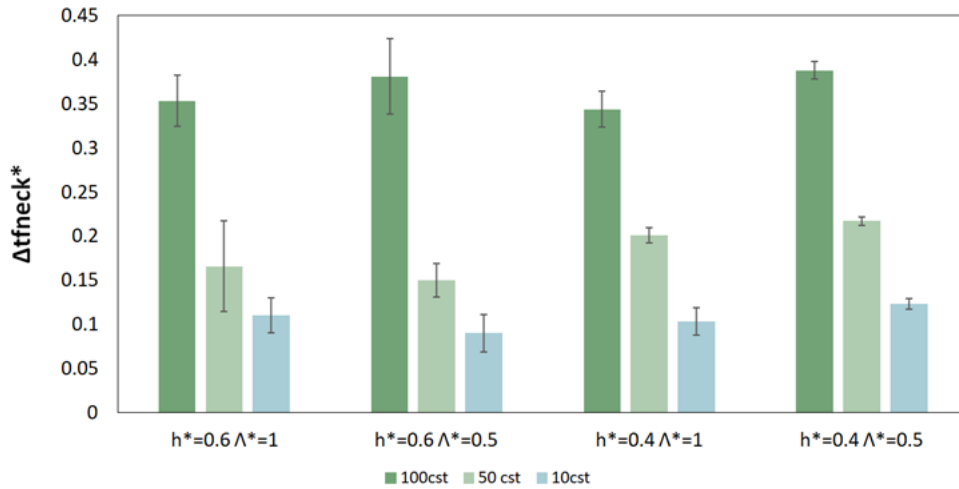


Figure 4.10: Bar plot of the duration of the necking stage for all experimental cases. Duration of this stage was only governed by the oil viscosity (or the viscosity ratio of fluids:  $\eta$ ) and as the oil viscosity was reduced, the necking duration was shortened due to the shear thinning property of the red blood cells. Other dimensionless parameters ( $h^*$ ,  $\Lambda$ ) had no impact on the duration of this stage.

The duration of this stage is correlated with a degree of blockage of the continuous phase. Thus, droplet volume is correlated with the characteristic shape of the droplet in



each stage. Van Steijn et al. suggested that for Newtonian fluids, the neck thickness at the pinch-off point is determined by the geometry of the system ( $2r_{pinch}^* = h^*/1+h^*$ ) [109]. For non-Newtonian fluids, Zhang et al. compared the neck thicknesses of fluids with various elasticity. They found that the neck thickness is not only controlled by the continuous phase but also by the shear-thinning property of the fluid [119]. However, it was found that neither oil viscosity nor red blood cell concentration affects the neck thickness at pinch-off (see Figure 4.7b, case E and F and Figure 4.11c). Moreover, our analysis agreed well with Van Steijn’s analysis, where  $2r_{pinch}^*$  only depends on the aspect ratio of the channel (see Figure 4.7b and Figure 4.11c). However, it was also found that, as the oil viscosity increased, the droplet elongated, likely due to the shear-thinning property of the red blood cell solution, which resulted in the differences seen in the necking duration (see details in Chapter 5).

The overall formation cycle was governed by three dimensionless parameters, but was most affected by the width ratio. As the width ratio decreased, the duration of droplet formation increased due to the long lag stage, as shown in Figure 4.11d. The second parameter was the viscosity ratio. Increasing the oil viscosity resulted in a longer formation cycle due to the elongation of the droplet of the red blood cell solution. The last parameter was the aspect ratio, where its increase resulted in a longer formation cycle. As shown in Figure 4.7b, the cell concentration did not significantly affect the formation cycle.

#### 4.4.2 Scaling of Operational Parameters

In this section, the effect of the dimensionless parameters on the final droplet volume, droplet spacing, and droplet frequency was investigated. As shown in Figure 4.12, all the experimental data followed the general scaling law  $V_d^* = \alpha + \beta$  that is known to be valid for Newtonian fluids.  $\varphi$  and  $\beta$  are functions of the various dimensionless parameters defined previously, which will be elucidated shortly. In general, the droplet volume scaled with the flow rate ratio linearly (Figure 4.12a). This linear correlation was utilized in modeling of the final droplet volume for non-Newtonian fluids in the Chapter 5. The generation frequency, however, did not conform to a linear relationship (Figure 4.12b) and the spacing between the droplets scaled linearly with the inverse of the flow rate ratio for all cases (Figure 4.12c).

As shown in Figure 4.12, under the same flow conditions, reducing the width ratio or aspect ratio resulted in smaller droplet formation at higher frequencies with longer spacing (Case A-C or Case A-B). Thus, the geometry of the channel plays a role in the droplet formation. Under the same geometrical conditions, increasing the flow rate ratio resulted

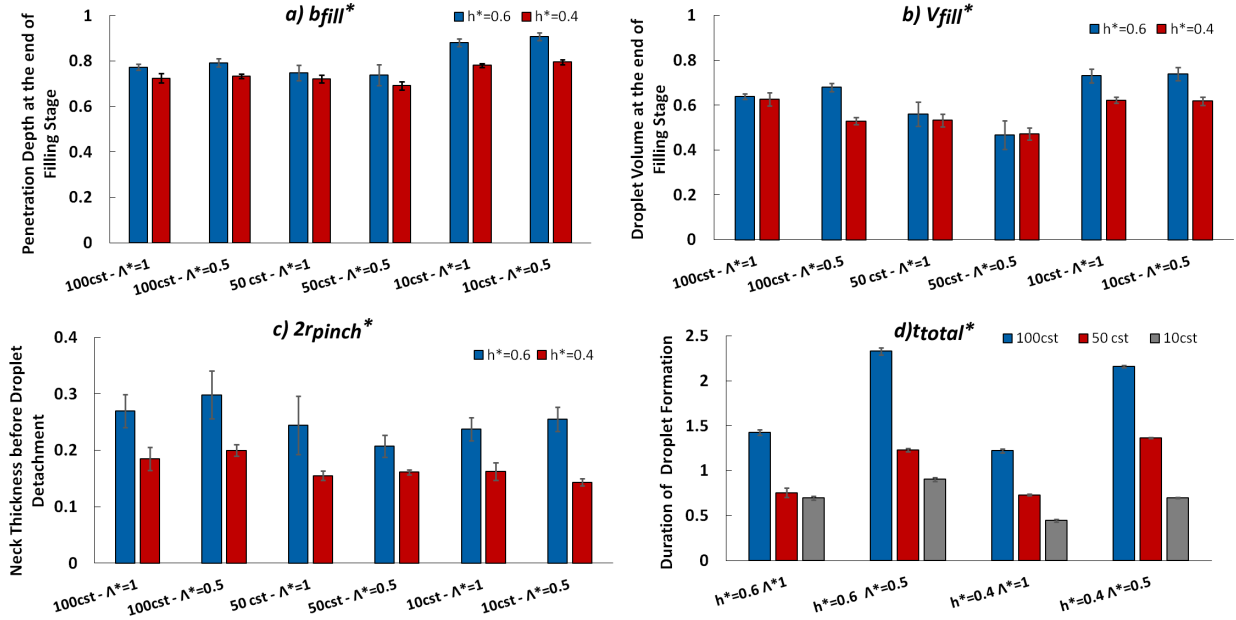


Figure 4.11: Bar plots showing the dependence of the four dimensionless variables ( $b_{fill}^*$ ,  $V_{fill}^*$ ,  $2r_{pinch}^*$ ,  $t_{total}^*$ ) to the dimensionless parameters ( $h^*$ ,  $\Lambda$ ,  $\eta$ ) for twelve cases a) Dimensionless penetration depth ( $b_{fill}^*$ ) at the end of the filling stage was dependent only to the aspect ratio ( $h^*$ ) b) Similar to the penetration depth, dimensionless droplet volume at the end of the filling stage ( $V_{fill}^*$ ) was dependent to the aspect ratio ( $h^*$ ) c) Dimensionless neck thickness right before the pinch-off point ( $2r_{pinch}^*$ ) was dependent only to the aspect ratio ( $h^*$ ) d) Dimensionless total duration of a droplet formation cycle ( $t_{total}^*$ ) was dependent to all dimensionless parameters ( $h^*$ ,  $\Lambda$ ,  $\eta$ ).

in larger droplets at a higher formation frequency with shorter spacing between droplets (Case A-D). When both geometrical conditions and flow rate ratio were kept fixed, droplet volume decreased, and both generation frequency and spacing increased as the oil viscosity was increased (Case A-E). Finally, it was observed that changing the concentration of red blood cells did not affect the observed trends (Case A-F).

## 4.5 Conclusion

In summary, the dependence of each formation stage on the dimensionless parameters was analyzed, and it was found that all the dimensionless parameters play a role in a

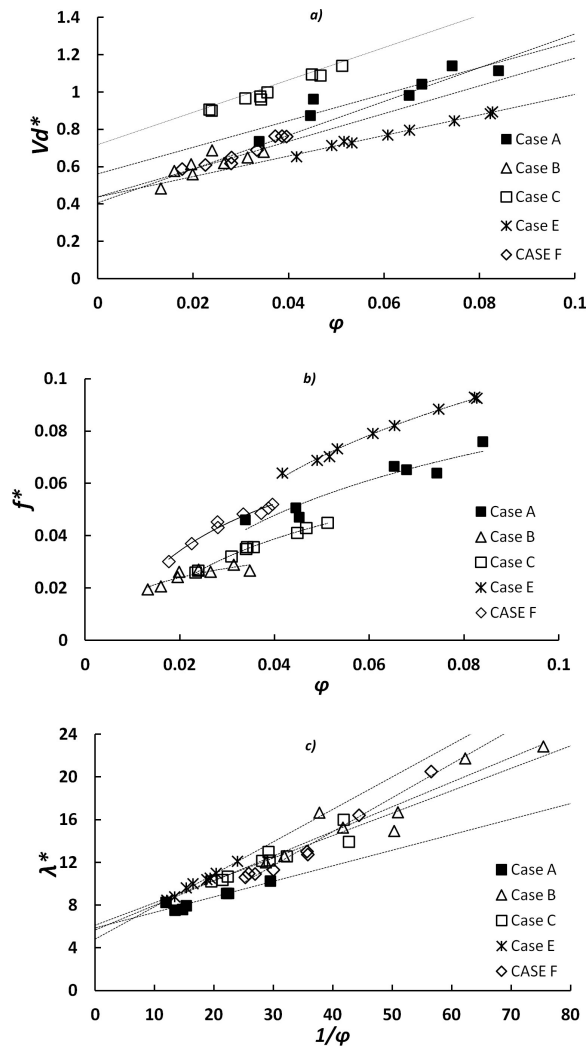


Figure 4.12: Scaling analysis of the dimensionless operational parameters (final droplet volume ( $V_d^*$ ), spacing between droplets ( $\lambda$ ) and droplet generation frequency ( $f^*$ )) over a range of flow rate ratios ( $\varphi$ ) for six representative cases, a) Dimensionless final droplet volumes over flow rate ratios. Final droplet volumes were linearly proportional to the flow rate ratios for all cases, b) Dimensionless generation frequencies over flow rate ratios. The data exhibit a non-linear trend with respect to the flow rate ratios, c) Dimensionless spacing between droplets over flow rate ratios. Spacing between droplets were inversely proportional to the flow rate ratio.

specific stage of the formation. Among the dimensionless parameters, cell concentration, which was expected to impact on viscosity ratio, did not vary the formation cycle or any variables discussed above. Thus, one can see that, unlike the standard squeezing regime, the droplet formation depends not only on the geometry and flow conditions but also on fluid viscosities in the presence of the biological non-Newtonian fluids. In the observation part of this study, a detailed analysis of the droplet formation dynamics with the biological non-Newtonian fluids was investigated experimentally. Unlike other non-Newtonian fluids, the evolution of the droplet was divided into three stages: lag, filling, and necking stages. In the following chapter, a mathematical model was presented to define the final droplet volume of red blood cell droplets in a T-junction.

## Symbols and Nomenclature

PEO

1D

EDTA

PBS

$w_c$

$w_d$

$h$

$Q_c$

$Q_d$

$V_d$

$\lambda$

$f$

$Q_{drop}$

$L_m$

$n$

$\varphi$

$\wedge$

$h^*$

$b^*$

$El$

$C_{cell}$

$R_{hyd}, R_m, R_c$

$u_d$

$b_{fill}$

$2r_n$   
 $b_{pinch}$   
 $V_d^*$   
 $V_{fill}^*$   
 $t_{total}^*, t_{lag}^*, t_{fill}^*, t_{neck}^*$   
 $\alpha, \beta$   
 $\alpha_{lag}, \alpha_{fill}$   
 $R_n, R_{fill}, R_{pinch}$   
 $L_{lag}^*$   
 $V_{c_{pinch}}^*$   
 $V_{c_{fill}}^*$   
 $A_{gap}^*$   
 $b_{ave}^*$   
 $a^*$   
 $\epsilon^*$

# Chapter 5

## Mathematical Modeling of Droplet Formation of Red Blood Cells in a T-junction

In this project Merve Marcali (Ph.D. candidate, Department of Mechanical and Mechatronics Engineering) conducted all the data analysis and developed a mathematical model. Prof. Carolyn Ren (Department of Mechanical and Mechatronics Engineering, University of Waterloo) and Prof. Marc G. Aucoin (Department of Chemical Engineering, University of Waterloo) provided thoughtful discussions to accomplish the project.

### 5.1 Introduction and Objective of the Project

In the first part of this study, experimental observations of the evolution of red blood cell droplets under the squeezing regime in a T-junction generator were presented. Unlike Newtonian fluids where the channel geometry governs the formation of the droplet under the squeezing regime, the formation of red blood cell droplets was found to be the result of a combination of channel geometry ( $h^*$ =aspect ratio,  $\Lambda$ =width ratio) and flow conditions (fluid viscosities and  $\varphi$ =flow rate ratio). Furthermore, video analysis showed that the formation of red blood cell droplets consisted of three stages: the lag, filling and necking stages (see Figure 4.5). In literature, a stretching phase was observed for other non-Newtonian fluids where a thread elongated into the main channel before detachment of a droplet [16], [49], [99], [83], [119]. In our work, thread elongation was not present, and it

was found that the red blood cell droplets immediately pinched off from the corner of the T-junction at the end of the necking stage.

In the lag stage, the interface of the droplets receded into the dispersed phase channel after the previous droplet detached. However, receding of the interface of red blood cell solutions was most prominent in channel designs that had a lower width ratio, which resulted in a longer lag stage and a larger spacing between droplets.

In the filling stage, the interface penetrated the main channel and deformed. It was found that the deformed droplet presented a similar characteristic shape of the droplet that presented by Van Steijn et al., and was used to model the final droplet volume [109]. As discussed in previous sections, the penetration depth of the red blood cell droplet ( $b_{fill}^*$ ) was dependent on the aspect ratio. Since the penetration depth of the interface changes the characteristic shape, volume of the droplet at this stage became dependent to the aspect ratio.

In the necking stage, the neck thickness of the droplet ( $2r_n^*$ ) reduced leading the droplet to pinch-off due to obstruction of the main channel. Contribution of the necking stage to the final droplet volume was calculated by defining the shape of the droplet at this stage and the critical neck thickness of the droplet ( $2r_{pinch}^*$ ) right before pinch-off similar to Van Steijn et al. [109]. In addition, the critical neck thickness was only a function of the aspect ratio of the microchannel similar to previous studies with Newtonian fluids. Therefore, a similar mathematical expression was utilized to define the critical neck thickness of the red blood cell droplet.

In this current study, the aim was to develop a model that predicted the final volume of red blood cell droplets. For this, the analysis of two variables ( $b_{fill}^*$  and  $2r_{pinch}^*$ ) are required. To verify the capability of the model to predict the droplet volume and other operational parameters (spacing between droplet and generation frequency), a comprehensive experimental analysis across the various channel geometries and flow conditions was performed in Chapter 4.

Droplet volume for Newtonian fluids has been described by the given Equation 5.1:

$$V_d^* = \alpha_{lag} + \alpha_{fill} + \beta\varphi \quad (5.1)$$

where  $V_d$  is the droplet volume,  $\varphi$  is the flow rate ratio,  $\alpha_{lag}$  and  $\alpha_{fill}$  are the volumes added during the lag and filling stages respectively, and  $\beta$  is the dimensionless necking time, which relates to the growth of the droplet while the neck of the droplet collapses. In this study, mathematical expressions for these three terms were developed and validated against experimental data. The mathematical expressions for these terms were related to

the characteristic geometrical shape of the droplet that was formed, which was previously defined by Van Steijn et al. in Equation 5.2:

$$V = hA - h^2/2(1 - \pi/4)l \quad (5.2)$$

where  $V$  is the volume of the droplet,  $h$  the channel height,  $l$  the perimeter of the droplet, and  $A$  the 2D top-view area of the droplet. To apply this expression to our analysis, the out of plane curvature of the droplet,  $r \sim h/2$ , was predicted by assuming that the non-wetting condition was achieved [39]. Furthermore, all the droplets were plug-like (sizes were larger than the channel width). In addition, the dynamics of changing interfacial tension were neglected by avoiding the use of surfactant and with the assumption that interfacial tension was at equilibrium throughout the formation process [96], [111].

Other variables that are required to define the 2D shape of the droplet and to modify the given definition in Equation 5.2 were presented, as shown in Figure 5.1. The penetration of the droplet interface into the main channel was defined as “ $b$ ”, and this variable was defined as  $b_{fill}^*$  at the end of filling stage and  $b_{pinch}^*$  at the end of necking stage.  $B_{fill}^*$  also defined the diameter of the half-circle at the front of the droplet. The back circle radius was defined as  $R_n^*$ , and the distance from the droplet interface to the opposite corner of the T-junction was defined as neck thickness,  $2r_n^*$ . Similar to penetration depth,  $R_n^*$  and  $2r_n^*$  were defined as  $R_{fill}^*$  and  $2r_n^*$  at the filling stage and  $R_{pinch}^*$ ,  $2r_{pinch}^*$  at the necking stage. In the following section, the mathematical expressions of the  $\alpha_{lag}$ ,  $\alpha_{fill}$  and  $\beta$  parameters are explained.

### 5.1.1 Lag Stage

In this stage, the droplet interface receded into the dispersed phase channel after detachment from the previous droplet. Then the interface was pushed back to the entrance of the junction. Contribution of this recovery to the final droplet volume of this stage can be described based on the shape of the droplet interface after a previous droplet detaches from the dispersed phase channel, as shown in Figure 5.2. Hence, by applying Equation 5.2, the lag phase volume can be calculated using the Equation 5.3 given below:

$$V_{lag}^* = \alpha_{lag} = L_{lag}^* \wedge + \frac{1}{2} \left(1 - \frac{\pi}{4}\right) \left(\wedge^2 + \frac{\pi \wedge h^*}{2}\right) \quad (5.3)$$

where  $L_{lag}^*$  is the dimensionless lag distance, and  $\alpha_{lag}$  is the dimensionless lag volume. The only unknown in this equation is the lag distance. Since lag distance has an undefined and complex relation to the flow conditions and the geometry, instead of defining a



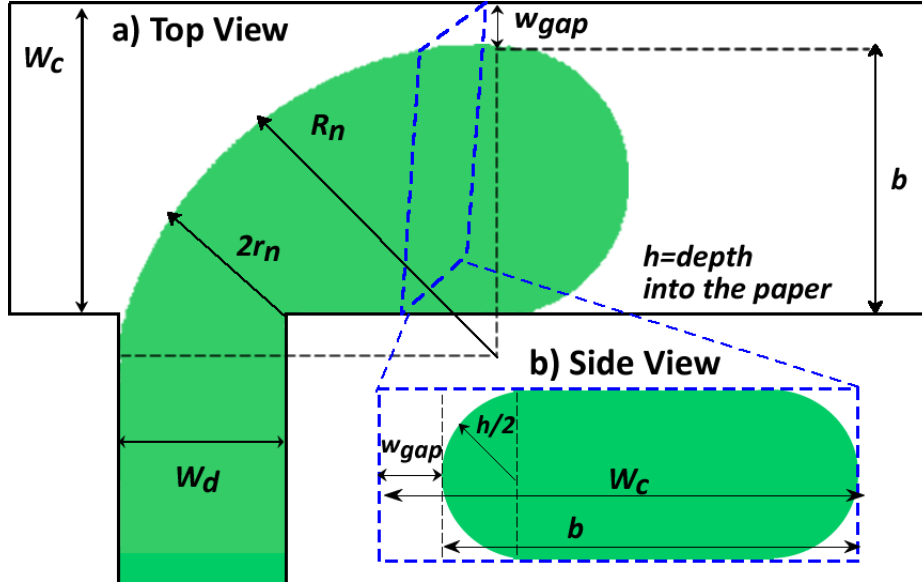


Figure 5.1: Schematic of a 2-D view of the characteristic shape of the droplet a) Top view b) Cross-section view. Channel width of the dispersed phase is indicated as  $w_d$ , channel width of the continuous phase  $w_c$ ,  $h$  is the channel height,  $2r_n$  is the neck thickness of the emerging droplet,  $R_n$  is the radius of the back half of the droplet,  $b$  is the penetration depth (or the radius of the front half of the droplet), and  $w_{gap}$  is the gap between the droplet and the far channel wall where silicone oil bypasses.

mathematical expression, experimental data was inserted into Equation 5.3. Experimental observations showed that the lag distance was more significant when a narrower dispersed phase channel was used. For wider channel designs, the lag distances become immeasurable ( $L_{lag}^* \sim 1,2 \mu m$ ). Thus, the contribution of the lag stage was only considered for  $\Lambda=0.5$ .

### 5.1.2 Filling Stage

In this stage, as the interface penetrated into the main channel, hydrodynamic forces balanced out and deformed into a characteristic shape as shown in Figure 5.3. The shape consisted of two small circular geometries. The first one was a half-circle located at the front of the droplet with a diameter  $b_{fill}$ , and the second one was a circle segment located at the back half of the droplet with a radius  $R_n$ . Depending on the width ratio of the channel, the radius of the circle segment at the back changed, becoming either equal to  $b_{fill}$  or  $w_d$  ( $R_n=b_{fill}$ ; if  $w_d \leq b_{fill}$  or  $R_n=w_d$ ; if  $w_d > b_{fill}$ ). Thus, two different cases

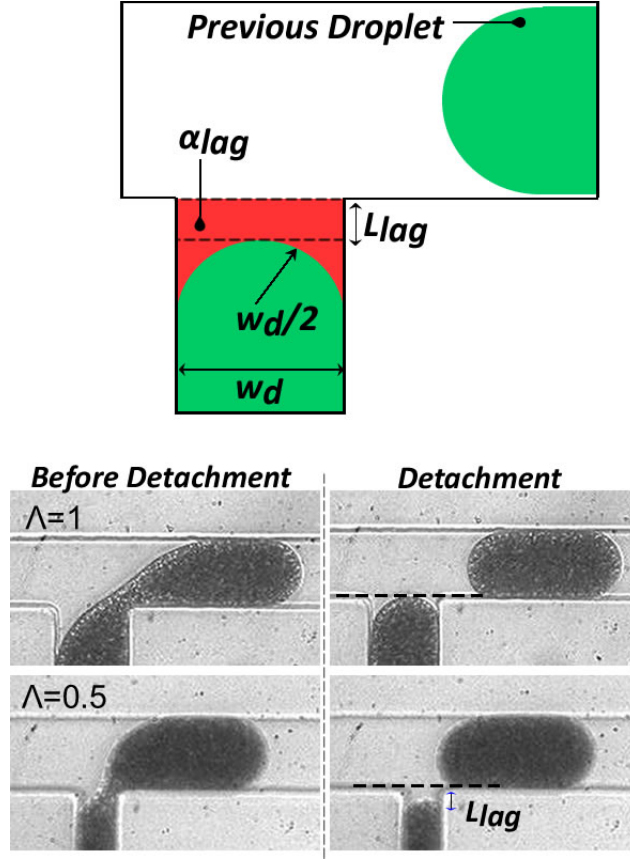


Figure 5.2: Schematic of the droplet interface during the lag stage (top figure). Microscopic images of red blood cell droplets before and after the detachment for two different channel width ratios (bottom image). For the designs where width ratio ( $\Lambda=1$ ), no receding of the interface was observed, and the interface stayed right at the junction entrance after the previous droplet detached as indicated with the black dashed lines. However, in case width ratio ( $\Lambda=0.5$ ), the dispersed phase receded back and the lag distance ( $L_{lag}$ ) became observable.

defined the volume at the filling stage (see Figure 5.3a, Figure 5.3b). The filling volume for  $w_d \leq b_{fill}$  can be calculated in given Equation 5.4:

$$V_{fill}^* = \alpha_{fill} = \frac{3\pi}{8} b_{fill}^{*2} - \frac{h^*}{2} \left(1 - \frac{\pi}{4}\right) (\pi b_{fill}^* + (b_{fill}^* - \Lambda)) \quad (5.4)$$

For  $w_d > b_{fill}$ , the back circular segment becomes a half-circular segment, as shown in

Figure 5.3b. Thus, the volume,  $V_{fill}^*$  was calculated as follows:

$$V_{fill}^* = \alpha_{fill} = \frac{\pi}{8} b_{fill}^{*2} + \frac{\wedge^2}{4} (\theta - \sin \theta) - \frac{h^*}{4} (1 - \frac{\pi}{4}) (\pi b_{fill}^* + \wedge \theta) \quad (5.5)$$

where the angle was calculated by given Equation 5.6 below:

$$\theta = 2 \arccos(1 - \frac{b_{fill}^*}{\wedge}) \quad (5.6)$$

The penetration depth  $b_{fill}^*$  at the end of the filling stage was the only unknown variable. Since hydrodynamic forces define the final shape of the droplet,  $b_{fill}^*$  can be determined by a force balance analysis.

### 5.1.3 Necking Stage

In this stage, the droplet continued to grow as the neck of the droplet collapsed. Thus, the final droplet size depended on the necking time and the flow rate ratios. The dimensionless necking time was defined as  $\beta$  in the current model, and was correlated with the fraction of the flow of the continuous phase that was blocked by the interface. Once the neck reached the critical point ( $2r_{pinch}^*$ ), the droplet pinched off. Thus, the shape of the continuous phase fraction (control volume - red area in Figure 5.4 or red dashed area, see Figure 5.5) was needed to calculate  $\beta$  from the following Equation 5.7:

$$\beta = (v_{c_{pinch}}^* - V_{c_{fill}}^*) (1 - \frac{A_{gap}^*}{h^*})^{-1} \quad (5.7)$$

where  $(1 - A_{gap}^*/h^*)^{-1}$  represents the fraction of the continuous phase which pushes the interface of the droplet to the opposite corner,  $v_{c_{pinch}}^*$  is the control volume at a pinch-off point,  $V_{c_{fill}}^*$  is the control volume at the end of the filling stage.  $A_{gap}^*$ , is the area of the gap between the droplet and the outer wall, can be calculated using the given Equation 5.8:

$$A_{gap}^* = (1 - b_{ave}^*) h^* + (1 - \frac{\pi}{4}) \frac{h^{*2}}{2} \quad (5.8)$$

Because the penetration depth is dynamic during the necking stage, the average penetration depth,  $b_{ave}^*$  ( $b_{ave}^* = (b_{pinch}^* + b_{fill}^*)/2$ ), was used to define the gap. Both control

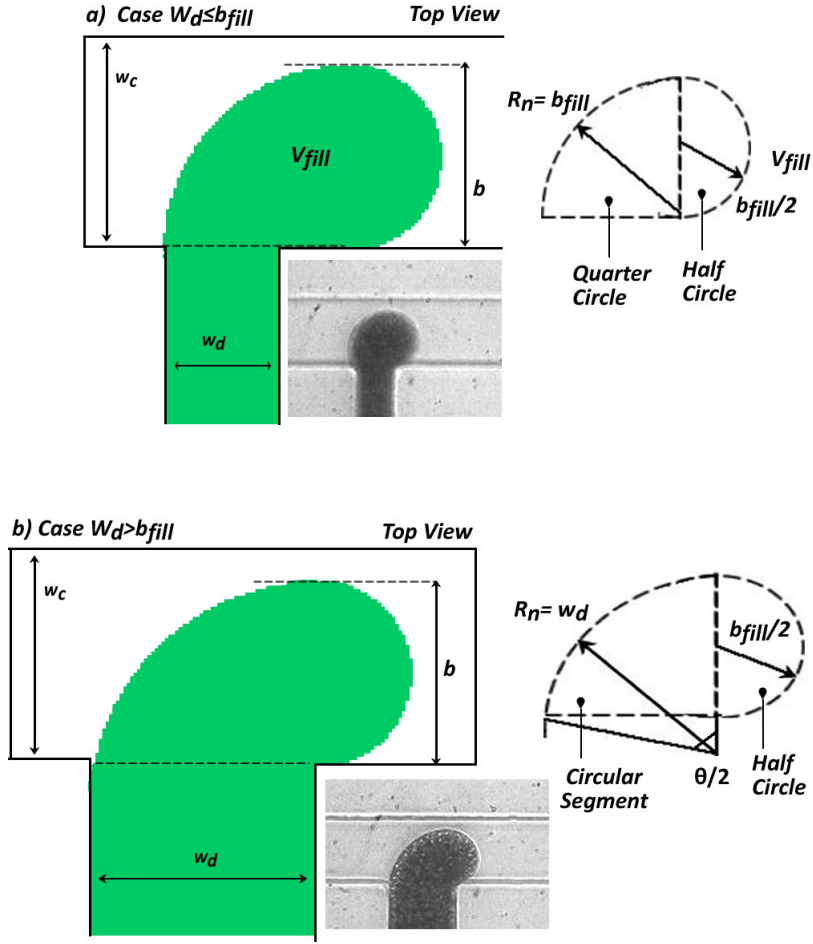


Figure 5.3: Schematic of 2D-shape of the droplet at the end of the filling stage for two cases a) For cases  $w_d \leq b_{fill}$ , the back half of the droplet is a quarter-circle with a diameter equal to  $b_{fill}$  and the radius of the front half of the droplet also is  $b_{fill}$  b) For cases  $w_d > b_{fill}$ , the back half of the droplet is not equal to a quarter circle and the radius of the circular segment equals to the dispersed phase channel width ( $w_d$ ). Therefore, the volume contribution of this stage to the final droplet volume is calculated by utilizing these two different geometrical shapes.

volumes,  $V_{c_{fill}}^*$  and  $V_{c_{pinch}}^*$ , can be obtained by applying Equation 5.2 to the 2D shape of the droplet at those stages. More detailed images of the 2D-shapes of these two volumes were presented in Figure 5.4a, b. In Figure 5.4a, one can say that  $V_{c_{fill}}^*$  was the sum of two regions (purple and red area). Thus,  $V_{c_{fill}}^*$  was calculated by using Equation 5.9:

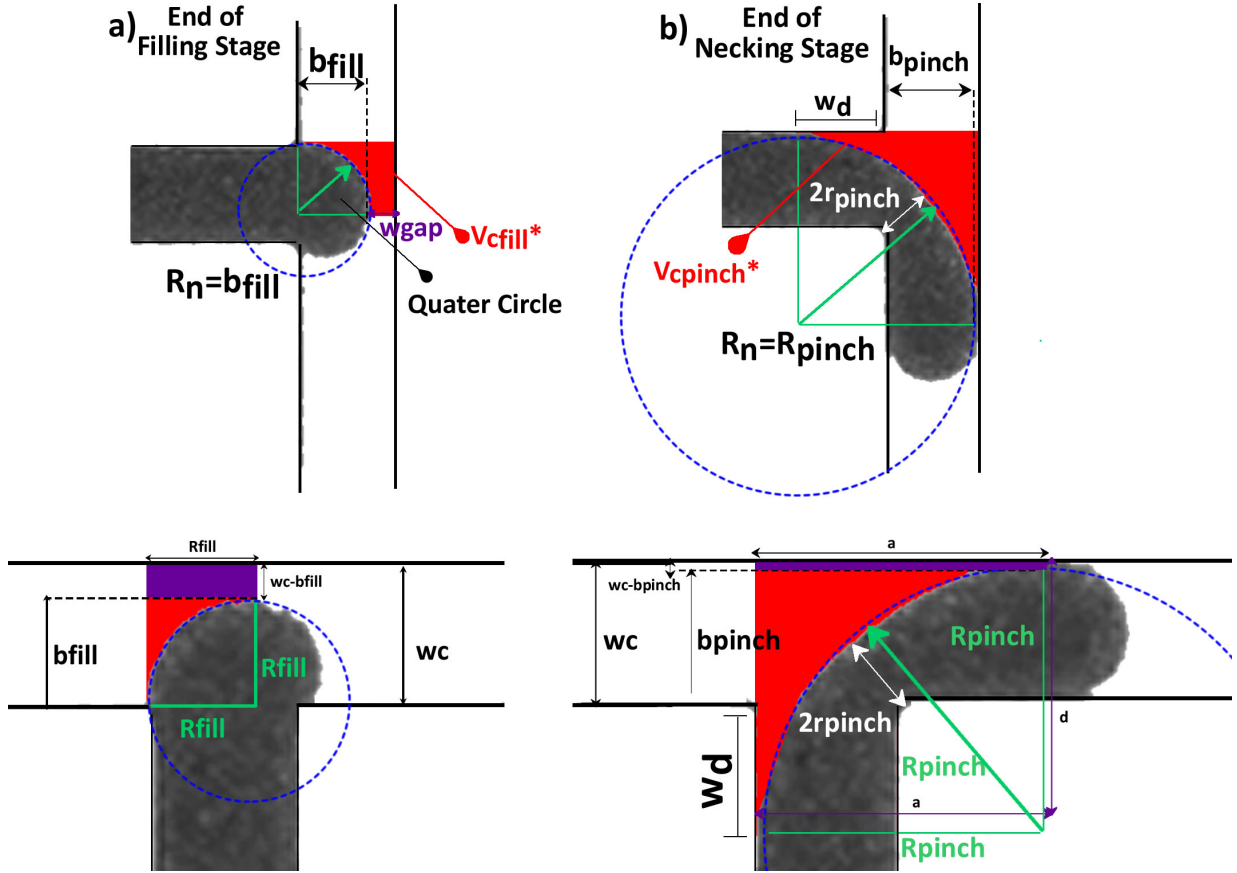


Figure 5.4: Schematic of 2D-shapes of the droplets at the end of the filling and necking stages. The subtraction of the two geometrical shapes (b-a) help to calculate the volume contributions of the oil phase to the droplet pinch-off a) Left top image indicates the end of the filling stage. Red area represents the control volume of the oil phase ( $V_{cfill}^*$ ) that contributes to necking of the droplet. Bottom left figure illustrates a detailed view of the control volume which is the sum of two distinct geometrical regions (red and purple areas) b) Right top image indicates the end of the necking stage. Red area represents the control volume of the oil phase ( $V_{cpinch}^*$ ) that contributes to necking of the droplet. Bottom right figure represents the detailed view of the control volume that was the sum of two geometrical shapes (red and purple areas).

$$V_{cfill}^* = (1 - b^*)R_{fill}^* + (1 - \frac{\pi}{4})(R_{fill}^*)^2 + \frac{\pi h^*}{4}(1 - \frac{\pi}{4})R_{fill}^* \quad (5.9)$$

The first expression on the right hand side of the Equation 5.9 indicates the volume contribution of the purple section. The middle expression indicates the red area and the final expression indicates the volume contribution of the droplet depth into the paper.

In the model of Van Steijn for the Newtonian fluids, the shape of the control volume at the pinch-off point was approximated as a quarter-circle [109]. However, it was found that due to the shear-thinning property of the red blood cell solution, the droplet elongated into the main channel before the detachment, and the quarter-circle shape was distorted as shown in Figure 5.5. The distorted shape of the red blood cell droplet presented a similar shape with the formation of droplets of the Newtonian fluids under the transition regime [36]. For example, the neck shape resembled a quarter-circle shape initially. Then, the shape was distorted as the continuous phase started to penetrate into the dispersed phase channel by a distance  $w_d$ . After that, the continuous phase pinned at that distance as the droplet elongated into the main channel and increased the neck radius ( $R_n^*=R_{pinch}^*$ , see Figure 5.5). As a result, the necking duration increased as the neck radius increased. Furthermore, unlike the droplets under the transition regime, it was found that as the oil viscosity increased, the elongation increased, causing a larger neck radius, as shown in Figure 5.5a. Thus, to develop a mathematical expression for  $V_{c_{pinch}}^*$ , the shape of the back half of the droplet was adapted using the given variables in Figure 5.5b. In addition, these variables were modified based on the shear-thinning property of the red blood cell droplet to the shear stress.

$$d^* = b_{pinch}^* + \wedge \quad (5.10)$$

$$\theta = 2 \arccos\left(1 - \frac{\wedge + b_{pinch}^*}{R_{pinch}^*}\right) \quad (5.11)$$

$$\frac{a^*}{\eta} = \sqrt{d^*(2R_{pinch}^* - d^*)} \quad (5.12)$$

$$2r_{pinch}^* - \epsilon = R_{pinch}^* - \sqrt{(a^* - \wedge)^2 + (R_{pinch}^* - b_{pinch}^*)^2} \quad (5.13)$$

where  $a^*$  was the elongation length,  $\theta$  was the angle,  $\epsilon$  the roundness of the corner of the T-junction and,  $\eta$  was the viscosity ratio of the phases. As the shear increases, the red blood cell droplet viscosity changes, causing a dynamic change in the ratio of the fluid viscosities. However, the viscosity of red blood cells varied slightly under a wide range of shear rate, as shown in Table 4.2. Therefore, the effect of the dynamic viscosity change

was minimal, and the average viscosity of red blood cell provided enough accuracy for the analysis of the formation. Moreover, the roundness of the channel must be considered to minimize the error as suggested by Van Steijn et al. [109].

In the analysis of Glawdel et al., it was shown that the critical neck thickness  $2r_{pinch}^*$  was dependent on the viscosity ratio of the fluids and the channel geometry. Therefore, the changes in the neck radius before pinch-off ( $R_{pinch}^*$ ) was calculated by iterating the Equation 5.12 for the specific  $2r_{pinch}^*$ . Nevertheless, our analysis showed that  $2r_{pinch}^*$  was independent of the fluid viscosities, and it only changed when the aspect ratio of the channel was changed. Thus, the neck radius was calculated before the pinch-off ( $R_{pinch}^*$ ) by iterating the elongation length ( $a^*$ ) of the droplet under different shear rates. As a result, as the oil viscosity increased, the shear stress acting on the droplet increased resulting in lower viscosity ratio, an elongation of the droplet, and a larger neck radius. This also explains, why a longer neck duration was observed under the viscous continuous phases. After the definition of the back half of the droplet, control volume at the pinch-off ( $V_{c_{pinch}}^*$ ) can be calculated by the Equation 5.14:

$$V_{c_{pinch}}^* = (1 - b_{pinch}^*)a^* + (1 - \wedge)a^* - \frac{R_{pinch}^{*2}}{4}(\theta - \sin \theta) + \frac{\theta h^*}{4}(1 - \frac{\pi}{4})R_{pinch}^* \quad (5.14)$$

As shown in Figure 5.4b , the volume contribution of each area were represented in two colors (purple and red areas). Hence, one can say that the volume contribution of the purple area (the part where oil phase bypasses) was represented with the first expression of the Equation 5.14. Then, the middle expression was calculated by the geometrical shape of the red area. The final expression was calculated by considering the depth of the droplet into the paper.

As a final step, calculated  $V_{c_{pinch}}^*$  (5.9) and  $V_{c_{fill}}^*$  (5.10) were substituted into Equation 5.7 to determine  $\beta$ . In summary,  $\alpha$ ,  $\varphi$ , and  $\beta$  factors have been determined. However, ( $b_{fill}^*$  and  $2r_{pinch}^*$  still need to be further defined. In the following section, these two variables were defined.

### 5.1.4 Calculation of $b_{fill}^*$ and $2r_{pinch}^*$

#### Force Balance Analysis of the Emerging Droplet:

Droplet formation is governed by three major forces: the capillary force, the viscous force, and the pressure force. Once these forces are balanced, the characteristic shape of the

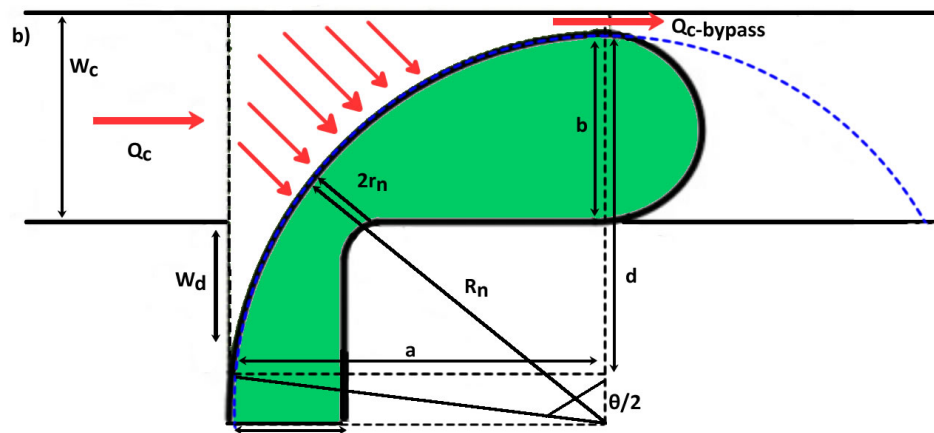
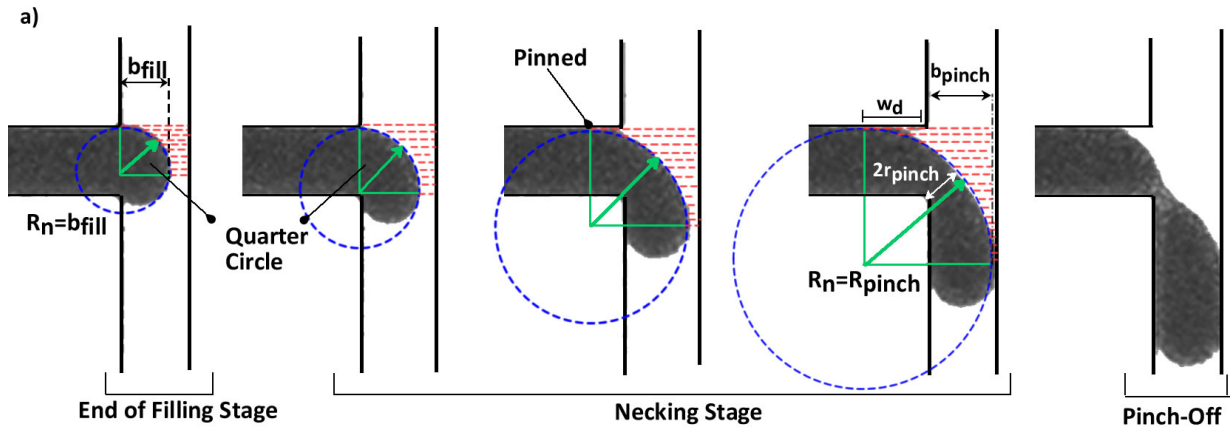


Figure 5.5: a) Sequence of microscopic images of the droplet collapsing during the necking stage. At the beginning of the necking stage, the back half of the droplet had a quarter circle shape. Then, as the droplet elongated due to the shear thinning property of the red blood cells and the pinning of the continuous phase at a distance  $w_d$ , a quarter-circle converted to a circular-segment and red dashed area changed over time. The volume change in the red dashed area contributed to the collapsing rate of the droplet b) To analyze the volume change, geometrical relations between variables were constructed. The schematic represents the geometrical shape and the required variables to calculate the volume of the oil phase at this stage. Elongation length was indicated as  $a$ ,  $d$  was the distance from the pinning point to the farthest penetration distance of the droplet.



droplet is formed. When this occurs, the penetration depth is defined as  $b_{fill}^*$ . When the sum of the viscous and pressure forces exceed the capillary force, necking begins. Thus, if forces are known the penetration depth can be calculated.

The capillary force acts against the deformation of the emerging droplet, and it is given by the multiplication of the projected area of the emerging droplet at the end of the filling stage with the Laplace pressure difference between the upstream and downstream ends of the droplet. The curvature of the downstream end is  $k_{down}=2/b_{fill}+2/h$ ; while the upstream curvature is  $k_{up}=1/R_n+2/h$ , and, the projected area is  $A \sim b_{fill}h$ . The resulting capillary force becomes:

$$F_\gamma \approx (-\gamma(\frac{2}{b_{fill}} + \frac{2}{h}) + \gamma(\frac{1}{R_n} + \frac{2}{h}))b_{fill}h \approx -\gamma h \quad (5.15)$$

The viscous force acts on the interface of the droplet to deform the droplet. The viscous force is given by the product of the shear stress acting on the droplet, and the associated area ( $A \sim b_{fill}h$ ) of that stress applies. The shear rate is approximated by the product of the continuous phase viscosity with the average velocity of the continuous phase flowing through the gap  $\tau \approx \mu_c u_{gap}/h$ . The resulting viscous force becomes:

$$F_\tau \approx \frac{\mu_c u_{gap}}{h} b_{fill}h \approx \frac{\mu_c Q_c}{h(w_c - b_{fill})} b_{fill}h \approx \frac{\mu_c Q_c b_{fill}}{(w_c - b_{fill})} \quad (5.16)$$

The pressure force can be approximated by using the lubrication analysis for pressure-driven flow in a thin-gap based on the Hagen-Poiseuille relation [101]. Although this relation is more complicated for non-Newtonian fluids, the current approximation provided enough information to determine the penetration depth at the end of the filling stage accurately. Based on this estimation, the resulting pressure force becomes:

$$F_p \approx \frac{\mu_c Q_c b_{fill}^2}{(w_c - b_{fill})^2} \quad (5.17)$$

Once the balances of these forces were done, a relation was obtained where the penetration depth,  $b_{fill}^*$  scales with the inverse of the capillary number. Christopher et al. have shown the balance of the forces, which is estimated according to [17]:

$$1/Ca \approx \frac{b_{fill}^*}{(1 - b_{fill}^*)^3} \quad (5.18)$$

To analyze the validation of Equation 5.18 to predict the penetration depth, experimental penetration depths of the six cases were substituted into the Equation 5.18. Moreover, the penetration depths at a different capillary number of these six cases were included in the fitting (into Equation 5.18). As shown in Figure 5.6a, fitting the experimental data with the model was satisfactory. Figure 5.6b presents the accuracy of the penetration depth calculations for all experiments under the same flow rate ratios. More than 85% the data falls within  $\pm 10\%$  of the predicted values. Furthermore, there is potential that error came from the measurement of the variables during video analysis.

### Laplace Pressure Balance of the Emerging Droplet:

Van Steijn et al., demonstrated that necking starts once the continuous phase bypassing the emerging droplet reverses direction due to the Laplace pressure difference from the tip and the neck of the droplet [109]. This additional flow speeds up the process, and pinch-off occurs almost immediately. Therefore, to define the critical neck thickness before pinch-off ( $2r_{pinch}^*$ ), we defined the Laplace pressures on both sides of the droplet. Based on the given definition, the Laplace pressures were modified for our system. The pressure at the neck of the droplet was redefined as  $P_{neck} = \gamma(1/R_n + \min(1/r_n, 2/h))$  and the pressure at the tip of the droplet was redefined as  $P_{tip} = \gamma(2/h + 2/w_c)$ . Once the sum of these forces equals zero, the flow reverses direction and the critical neck thickness could be calculated by;

$$2r_{pinch}^* = \frac{h^*}{(1 + h^*)} \quad (5.19)$$

The given expression suggests that the neck thickness was only a function of the aspect ratio ( $h^*$ ). Our experimental data in the previous section presented a similar trend where the neck thickness was a function of only the channel height. Therefore, Equation 5.19 was applied to the experimental data to predict the critical neck thickness. As shown in Figure 5.7, the given expression satisfies the experimental data well, where all data falls within  $\pm 15\%$  of the expected values. Since pinch-off occurs suddenly, there is an error that comes in determining the exact video frame where pinch-off occurs.

### 5.1.5 Validation of the Mathematical Model

Once the  $b_{fill}^*$  and  $2r_{pinch}^*$  were determined, substituting these variables into Equations 5.4, 5.5 and 5.7, the volume contribution of the filling ( $\alpha_{fill}$ ), and the necking stages

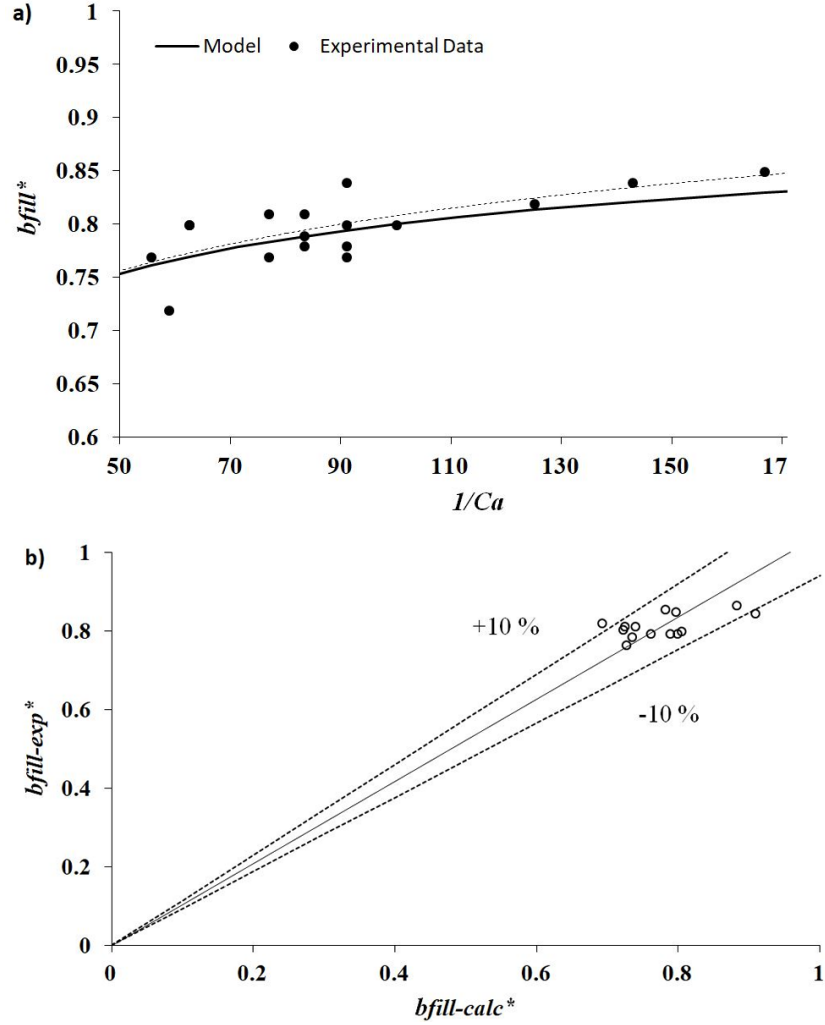


Figure 5.6: Comparison of experimentally measured penetration depth with the theoretical penetration depth using Equation 5.18. a) The experimental data of six cases under different capillary numbers were fitted to the model developed during the force balance analysis. b) Parity plot of the penetration depth for all cases under the same flow rate ratio ( $\varphi \sim 0.04$ ). The solid line represents the perfect parity, and the dashed lines are  $\pm 10\%$ .

$(\beta\varphi)$  can be calculated. For cases where  $\Lambda=0.5$ , the final droplet volume was estimated using Equation 5.1 ( $(V_d^* = \alpha_{lag} + \alpha_{fill} + \beta\varphi)$ ). However, for cases where  $\Lambda=1$ , the final droplet volume was estimated without the contribution of lag phases ( $(V_d^* = \alpha_{fill} + \beta\varphi)$ ).

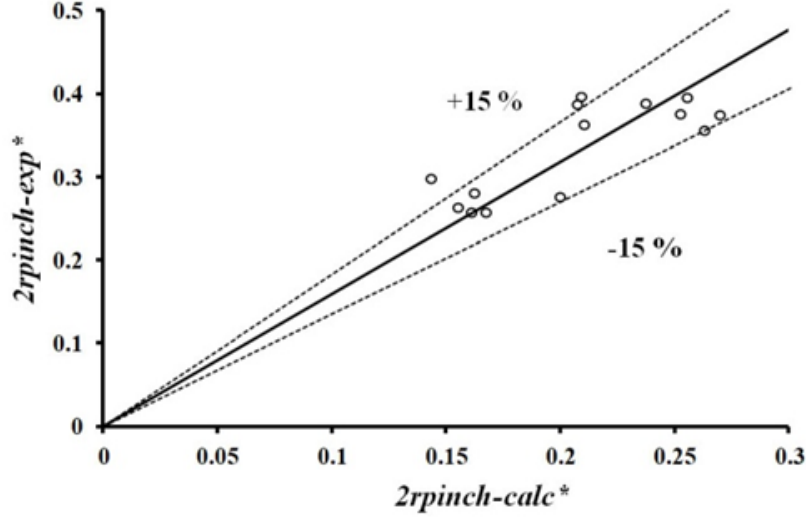


Figure 5.7: Parity plot of the critical neck thickness for all experiments under the flow rate ratio:  $\varphi \sim 0.04$ . The experimental neck thickness data fell within  $\pm 15\%$  of the theoretical neck thickness data using Equation 5.7.

Validation of this theoretical model was analyzed in the parity plot (Figure 5.8a). All the experimental data for T-junctions  $\Lambda=0.5-1$  and  $h^*=0.4-0.6$  under conditions ranging from  $\eta=0.06-1$  and  $Ca=0.001-0.019$  fell within  $\pm 20\%$  of the expected values. This suggests that the performance of the theoretical model developed in this study was successful in predicting the final droplet volume formed in the T-junction generator under the squeezing regime.

The performance of the model was investigated for other operational parameters of the T-junction generator, such as spacing between droplet and generation frequency. The spacing between droplet was estimated assuming that droplet length was proportional to the volume ( $V_d^* \sim L_{drop}^*$ ) and approximated based on the given Equation 5.20 below:

$$\lambda = L_{drop} + L_c \approx \lambda^* = (\alpha_{lag} + \alpha_{fill})\left(\frac{\varphi + 1}{\varphi}\right) + (\varphi + 1)\beta \quad (5.20)$$

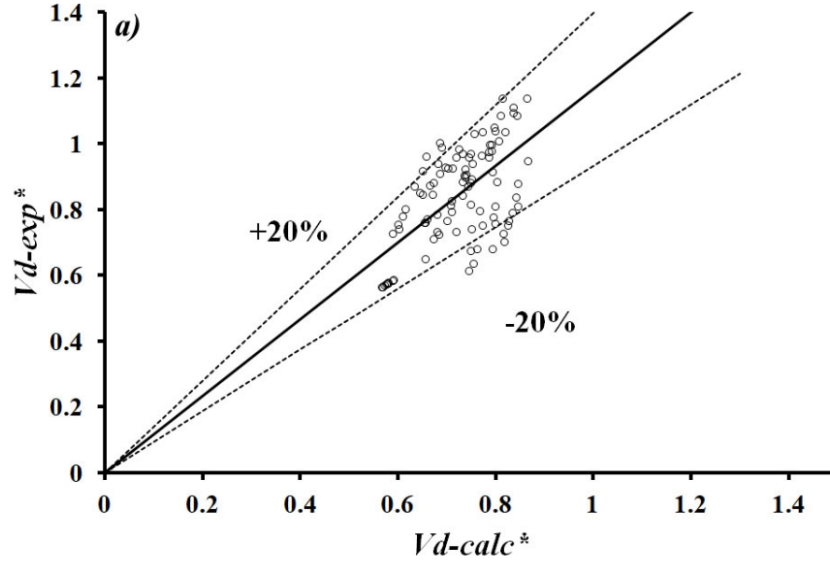
The generation frequency was approximated with the reciprocal of the total generation time, where the total generation time is the sum of the duration of each stage i.e.  $t_{total} = t_{lag} + t_{fill} + t_{neck}$  and in dimensionless form:

$$t_{total}^* = \frac{\alpha_{lag} + \alpha_{fill}}{\varphi} + \beta \quad (5.21)$$

The reciprocal of the dimensionless total time yields the generation frequency:

$$f^* = \frac{\varphi}{\alpha_{lag} + \alpha_{fill} + \beta\varphi} \quad (5.22)$$

As shown in Figure 5.8b and 5.8c, the predictions for droplet spacing and generation frequency were in good correlation with the experimental data. It should be noted that the volume contribution of the lag phase was only included for  $\Lambda=0.5$  cases for both the spacing and the frequency calculations given in Equations 5.21 and 5.22.



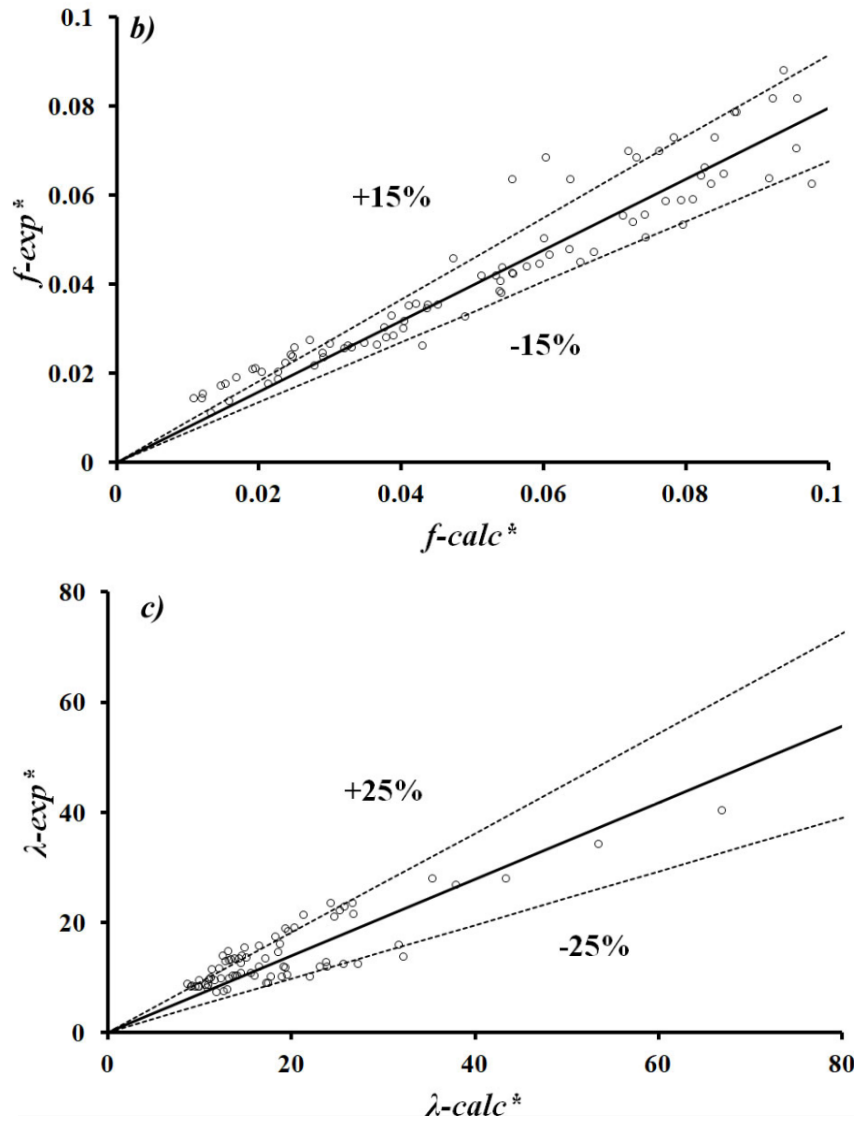


Figure 5.8: Parity plots for model validation for three major dimensionless operational parameters (final droplet volume ( $V_d^*$ ), droplet generation frequency ( $f^*$ ), spacing between droplets ( $\lambda^*$ ) a) Experimental droplet volume data fell within  $\pm 20\%$  of the calculated data b) Experimental droplet generation frequency data fell within  $\pm 15\%$  of the expected values c) Experimental data of the spacing between droplets fell within  $\pm 25\%$  of the expected values.

## 5.2 Conclusion

A mathematical model was presented to define the final droplet volume in a T-junction under the squeezing regime based on channel geometry and flow conditions. The model was constructed and validated in three steps. In the first part, the characteristic shape of the red blood cell droplet at the end of the filling stage and during the necking stage was determined. In the second part, an overall force balance and a Laplace pressure balance were done to define the penetration depth and the pinch-off point, which were substituted into the volume calculations of the droplet at filling and necking stages. Finally, experimental data was compared with the model predictions. It was shown that the model's predictions were in good agreement with the experimental data for various conditions such as different flow rate ratio, viscosity ratio, cell concentration, channel geometries, and capillary number.

### Symbols and Nomenclature

PEO

1D

EDTA

PBS

$w_c$

$w_d$

$h$

$Q_c$

$Q_d$

$V_d$

$\lambda$

$f$

$Q_{drop}$

$L_m$

$n$

$\varphi$

$\wedge$

$h^*$

$b^*$

$El$

$C_{cell}$

$R_{hyd}, R_m, R_c$   
 $u_d$   
 $b_{fill}$   
 $2r_n$   
 $b_{pinch}$   
 $V_d^*$   
 $V_{fill}^*$   
 $t_{total}^*, t_{lag}^*, t_{fill}^*, t_{neck}^*$   
 $\alpha, \beta$   
 $\alpha_{lag}, \alpha_{fill}$   
 $R_n, R_{fill}, R_{pinch}$   
 $L_{lag}^*$   
 $V_{c_{pinch}}^*$   
 $V_{c_{fill}}^*$   
 $A_{gap}^*$   
 $b_{ave}^*$   
 $a^*$   
 $\epsilon^*$



## Chapter 6

# Development of Hemagglutination Assay in Microdroplets to Quantify Influenza Virus

In this project Merve Marcali (Ph.D. candidate, Department of Mechanical and Mechatronics Engineering) designed, fabricated, tested the microfluidic device performance, and conducted all the experiments and data analysis. Mark Bruder (Ph.D. candidate, Department of Chemical Engineering, University of Waterloo), Madhuj Chakraborty (M.Sc. candidate, Department of Chemical Engineering, University of Waterloo), Eduardo Ramirez (M.Sc. candidate, Department of Chemical Engineering, University of Waterloo) assisted in preparing the virus-like particle constructs, insect cell cultures and the virus-like particle stocks. Prof. Carolyn Ren (Department of Mechanical and Mechatronics Engineering, University of Waterloo) and Prof. Marc G. Aucoin (Department of Chemical Engineering, University of Waterloo) supported the project by guiding discussions.

### 6.1 Overview of Previous Works

Infectious diseases are the leading cause of worldwide mortality and morbidity every year [77]. The World Health Organization has been recorded around 500 million cases of Influenza infections during seasonal epidemics [77]. Influenza A virus is one of the most virulent pathogens with a high potential of pandemic outbreak each year. To prevent pandemics, rigorous monitoring is needed, along with effective vaccine manufacturing. Both benefit from the ability to rapidly detect virus.

Virus-Like Particles (VLPs) are protein complexes that are composed of viral structural proteins. These particles mimic the organization of the original virus, but they do not contain any genetic material, as shown in Figure 2.16 in Chapter 2. Therefore, they have no ability to infect the host. Not only can VLPs as vaccines, themselves, but they can act as surrogates for viruses instead of risking infection by the wild-type virus.

The focus of this study was to develop a microfluidic assay to quantify the level of hemagglutination activity of Influenza VLP preparations. Influenza vaccines can be characterized in many ways, but all rely on the assessing the activity of hemagglutinin. There are many different characterization techniques available – and while SRID is used as release criteria, it does not need to be used throughout the manufacturing process and is not well suited for rapid detection. It is important to note that different techniques may be used for different purposes. Virus detection throughout a vaccine manufacturing process is different than detection of virus in a human (or animal). Furthermore, depending on the application, quantifying virus may infer knowing the number of particles or it may infer knowing the number of infectious particles. In the context of this work, there is a desire to quantify the virus i.e. the number of particles, by assessing the activity of HA molecules – which should be proportional to the total number of particles.

Techniques for quantifying virus can be grouped into two major categories: antibody-dependent methods and antibody-independent methods. SRID, ELISA (Enzyme-linked immune sorbent assay) and SPR (Surface Plasmon Resonance) are antibody-dependent methods, which require a strain-specific antibody. SRID, with a detection limit of 3-5  $\mu\text{g}/\text{ml}$  of HA, has been used to detect Influenza VLPs [104], [59]. However, it has been shown that Influenza VLP quantification is challenging in SRID due to the interference of diffusion in agarose gel caused by non-aqueous components of the VLP (lipid envelope) [55]. Furthermore, HA molecules are prone to aggregate in the presence of high virus concentration resulting in improper diffusion of HA and interference in the test output [7]. Another promising technique was developed using reversed-phase high-performance liquid chromatography (RP-HPLC), which showed better sensitivity than SRID where the limit of detection (LOD) was 0.25  $\mu\text{g}/\text{ml}$  of HA [64].

All antibody independent quantification methods are based on the characterization of the viral particle in terms of viral spike proteins or size and shape of the viruses. For example, TEM (transmission electron microscopy) is used to visualize virus particle size and morphology. The major drawback of this method is the elaborate sample preparation before imaging virus samples as well as being highly subjective [103]. Other methods depend on the virus particle size, such as cytometer, dynamic light scattering (DLS), have not been developed for VLP quantification yet. But they have presented promising results for virus quantification [97], [72]. The remaining antibody independent methods include hemagglu-

mination assay (HA Assay), and liquid chromatography-mass spectrometry (LC-MS). These methods utilize the antigen of the viral particle (spike protein) for quantification. Among these methods, Influenza VLP quantification has only been shown using a HA assay. However, promising HA and NA protein quantification in LC-MS has been demonstrated [22], [64]. During the production and purification of Influenza VLPs, the most commonly used quantification method is HA assay. This technique relies on the agglutination activity of the spike protein (HA) of Influenza with red blood cells. Although the assay procedure is most commonly used, this method has a few limitations. For example, dependence to the operator's judgment on the reading, labor-intensive preparation, and lack of sensitivity and standardization [103]. This study aims to eliminate the drawbacks of the standard HA assay by developing a quantification method using a droplet-based microfluidic system.

## 6.2 Introduction and Objective of the Project

The objective of this work is to develop a droplet-based microfluidic system able to quantify Influenza VLPs faster and with greater sensitivity than a standard HA assay that run in 96-well plates. Several research groups have investigated hemagglutination reactions using microfluidic devices. For example, investigation of blood typing sera in microdroplets where related antigens aggregate red blood cells in microdroplets was observed using various detection techniques [58], [91], [67], [69]. Although these techniques have shown promise for hemagglutination assays, there is a significant need to simplify the fabrication and overall testing. For example, most of these studies relied on tedious microfluidic channel surface modifications. In this study, protein absorption on channel walls was eliminated by merely treating the walls with silicone oil, eliminating the need for surfactant.

In this study, Influenza virus-like particles were quantified by running a hemagglutination assay in a droplet-based microfluidic system. Compared to a standard HA assay in well plates, the microfluidic system provided greater sensitivity and faster quantification where a minimal amount of reagents was consumed. To investigate the performance of the microfluidic device, the impact of virus concentration, red blood cell concentration, reagent freshness, virus-like particle type and droplet size on the reaction was analyzed as well as the limit of the detection of the system. The system provided enough information to differentiate the effect of each parameter in detail.

## 6.3 Design of Experiment

### 6.3.1 Materials and Methods

#### Continuous Phase

50 mPa.s silicone oil (DC200, Sigma Aldrich, MO, USA) was used as the continuous phase. In addition, it has been shown that using the silicone oil surface treatment provided good contact angle with red blood cells where non-wetting conditions were achieved [69]. Furthermore, in a previous study (Chapter 4 and 5), it was observed that the higher viscosity of silicone oil (100 and 50 mPas) provided better control in red blood cell droplet formation rather than 10 mPa.s silicone oil. Therefore in this study, only 50 mPa.s silicone oil was used.

#### Dispersed Phase

Red blood cells (Rockland, Chicken RBC %10 washed cell,  $1.20 \times 10^6$  cells/ml, USA) and various dilutions of red blood cell solution with phosphate buffer saline (PBS) were used as the dispersed phase. Red blood cell samples were stored in EDTA (ethylenediaminetetraacetic acid, Additive: K2Edta (Spray Dried), 7.2Mg.) tubes at  $4^\circ\text{C}$  to prevent cell coagulation before red blood cells were diluted. Virus-like particle stocks were used as another dispersed phase.

#### Crude Virus-Like Particle Preparations

Briefly, *Spodoptera frugiperda* clonal isolate 9 (Sf9) cells were maintained in SF-900<sup>TM</sup> III serum-free media (GIBCO, Carlsbad, CA, USA) at  $27^\circ\text{C}$  on an orbital shaker (VBR, Champaign, Illinois, USA) rotating at 130 revolutions per minute (rpm). Cell density was maintained between  $0.5 \times 10^6$  to  $4 \times 10^6$  cells/mL in 125 mL. Cell viability of the cell culture was maintained above 95%. Cell counts were measured using Countess<sup>TM</sup> II (Thermo Fisher). Insect cells were then infected with baculovirus at a density of  $1.5 \times 10^6$  cells/mL in a 30 mL culture with an MOI of 0.1 using P1 stock. From that, P2 stock was amplified, once the viability reaches below 70%, baculovirus was harvested. The infected culture was collected and centrifuged at  $800 \mu\text{g}$  for 10 min, then filtered through a  $0.2 \mu\text{m}$  membrane (VWR International, Mississauga, ON, Canada). Baculovirus stocks were stored at  $4^\circ\text{C}$ . These samples were prepared by Madhuja Chakraborty and Eduardo Ramirez in Prof.

Aucoin's Laboratory. Two types of baculovirus constructs designed and prepared by Mark Bruder in Prof. Aucoin's Laboratory. The first genetic construct included genes for three influenza proteins (HA, M1, and NA). The other construct included genes for a human immunodeficiency virus (HIV) protein, GAG, fused to the gene for green fluorescent protein (GFP) and an Influenza protein, HA. To produce the fluorescent VLP, 100 mL of Sf9 cells at a density of  $2 \times 10^6$  cells/mL were infected at an MOI of 0.1. Then infected cultures were harvested and filtered as described above.

### **Hemagglutination Assay**

HA activity of the harvested bulk supernatants and cell lysates obtained were measured using an HA assay. 50  $\mu\text{L}$  of 1x PBS were added to each well (except the first column) of a 96-well plate. 100  $\mu\text{L}$  of a virus sample was added to the first well, and the virus sample was diluted by serial two-fold dilutions. 50  $\mu\text{L}$  of 0.5% chicken red blood cells were added into all wells. After mixing, the plate was incubated at room temperature overnight. The HA titer of stocks was reported as HAU/50  $\mu\text{L}$  and represents the amount of material that agglutinates the red blood cells.

### **Surfactant**

It has been shown that surfactants interfere with the interaction of the virus with the target cell. Therefore, surfactant was not added to either phase in this project [89], [18].

### **Global Network Design**

In the current project, the microfluidic channel design is presented in Figure 6.1. There were several parameters to consider while designing the final structure of the channel. Droplet formation and mixing of two reagents were the main functions of interest. Therefore, a T-junction was used for the formation of the droplets and serpentine channels were used to insure mixing of the reagents within the droplets. In addition, to combine the two elements of the dispersed phase, a Y-junction was added prior to the T-junction.

Mixing in droplets is governed by molecular diffusion. Therefore, to enhance the mixing, the symmetry of the two reagent streams coming together into droplets needs to be broken. To break this symmetry, serpentine channels were used as initially proposed by Song et al. [93]. As the droplets turn in each curved region of the channels, the symmetry is disrupted,

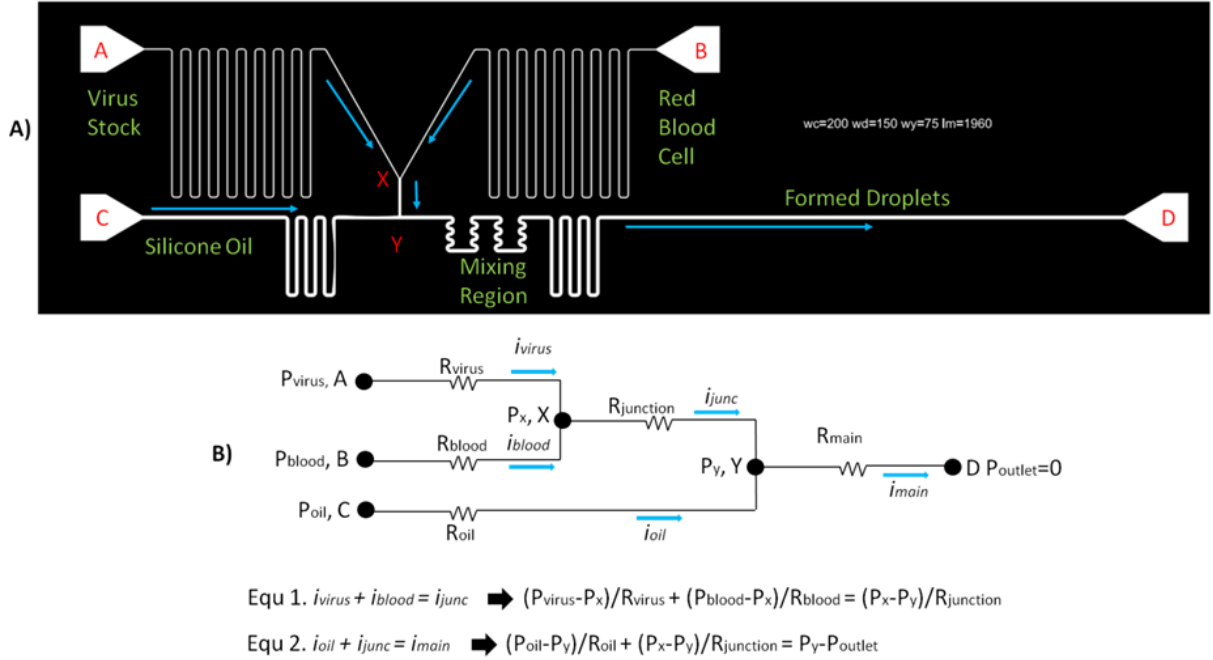


Figure 6.1: a) Schematic of the microfluidic device design. From point A, the virus stock was applied to the system. From point B, the red blood cell solution was applied. Silicone oil was used as a continuous phase (Point C). Droplets were generated at the T-junction (Point Y). Reagents in the droplets were mixed in the serpentine channels and the reaction was recorded from point Y through the end of the last serpentine channel. b) Equivalent electrical circuit of the microfluidic channel. The circuit analysis was done to design the microfluidic device robust enough to eliminate droplet size variations during formation and to achieve sufficient mixing in droplets.

and non-asymmetric vortices in the droplets create chaotic advection. As a result, the two reagents mix in the droplets. The mixing time is approximated by Equation 6.1:

$$t_{mix}, Ca \sim \frac{aw}{u} \log(Pe) \quad (6.1)$$

where  $Pe$  is the Peclet number,  $w$  is the channel width, and  $a$  is the dimensionless length of the droplet. Depending on the flow conditions, it is required to have at least 30 turns in this design when considering a channel width of  $200 \mu m$  and channel height of  $\sim 80 \mu m$  after swelling.

Other channel dimensions were designed by considering several criteria. The first one is the main channel length. The device should contain 50 droplets so that the flow field at the junction is not influenced by the formation or exit of droplets from the channel [36]. The second one is the length of the channel from point X to Y shown in Figure 6.1a. This length should be long enough so that the parallel flow of the two reagents would not be disturbed by the pressure jump at the T-junction. To eliminate this, a long dispersed phase channel were implemented as previously suggested by others [36], [42]. Furthermore, because different combinations of reagents was desired to see the effect of concentration on the reaction, the width and the length of the channel from X to Y was designed in a way that the pressure at point A would not overcome pressure at point B and able to flow under different applied pressures. By considering the analysis in Chapter 4 and 5 and the design criteria mentioned above, the required dimensions were calculated using Equation 4.10 as shown in Figure 6.1b. The calculation is based on the analogy of Kirchoff's current/voltage law, and an equivalent 1-D electrical circuit of the design is given in Figure 6.1b. As a result, the channel width from point X to Y was designed to be 150  $\mu\text{m}$  with a length of 1950  $\mu\text{m}$ . The dispersed phase channel widths were designed as half of the junction channel width, 75  $\mu\text{m}$ . The main channel where droplets were generated was designed to be 200  $\mu\text{m}$  wide.

### 6.3.2 Experimental Setup

The experimental setup consists of three major parts. The first one was the microfluidic chip mounted on the microscope stage, as shown in Figure 6.2. The second one is the pressure system that pumps the reagents into the microfluidic chip, and the third is the microscope where the images of generated droplet were recorded.

### 6.3.3 Experimental Procedure

In this subsection, the experimental procedure is provided. First, the virus stock was collected and purified. While preparing the cell culture, the microfluidic chips were fabricated using the soft lithography method, as described in Chapter 3. Before the experiment, the fabricated microfluidic chips were flushed with the silicone oil (50 mPa.s, Sigma Aldrich, MO, USA) and were baked at 120° C overnight. For the experiments, the chips were mounted onto the microscope stage (Ti. Eclipse, Nikon, Japan), and the silicone oil was flushed into the channels once again to prime the channel surfaces with oil. Then, the dispersed phases were connected to the pressure system (Fluigent, MC-8, Germany), and

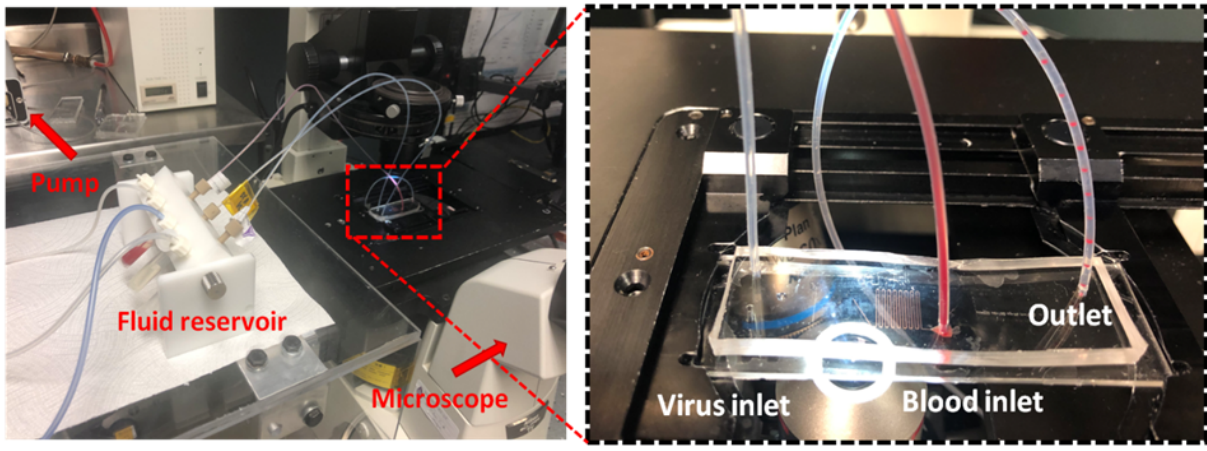


Figure 6.2: Images of the experimental setup and the microfluidic chip (on the left). Image of the microfluidic chip after the experiment was completed, see generated droplets inside the tubing that was connected to the outlet of the channel (on the right).

pressure values were adjusted to form droplets. Formation of droplets was recorded using a monochrome camera (Qimaging, Retiga, 2000R Fast 1394 monochrome CCD camera, Tucson, AZ, USA), and videos were edited to capture 20 droplets. The recorded videos were analyzed using the custom image analysis program implemented in MATLAB (Math-Work, 2018, MA, USA) and Image J (1.52r, WIS, USA). Details of the program are given in the next section. This procedure was repeated for each configuration of the reagents.

### 6.3.4 Image Analysis

Analysis of agglutinated red blood cells was done using ImageJ 1.52r (WIS, USA) and MATLAB (2018, MA, USA). In the analysis, MATLAB was used to extract frames of the videos. Then, a region of interest in each frame was cropped and recorded as an image. Cropped images were filtered to eliminate grey-scale noise in the image so that day to day differences in light exposure were eliminated. Filtered images were turned into a binary image. Threshold binning was applied to eliminate dark spots in the image that resulted from the PDMS defects other than red blood cells. The edge of the droplets was detected, and the agglutinated red blood cells area was calculated within the boundary of the edge, as shown in Figure 6.3.



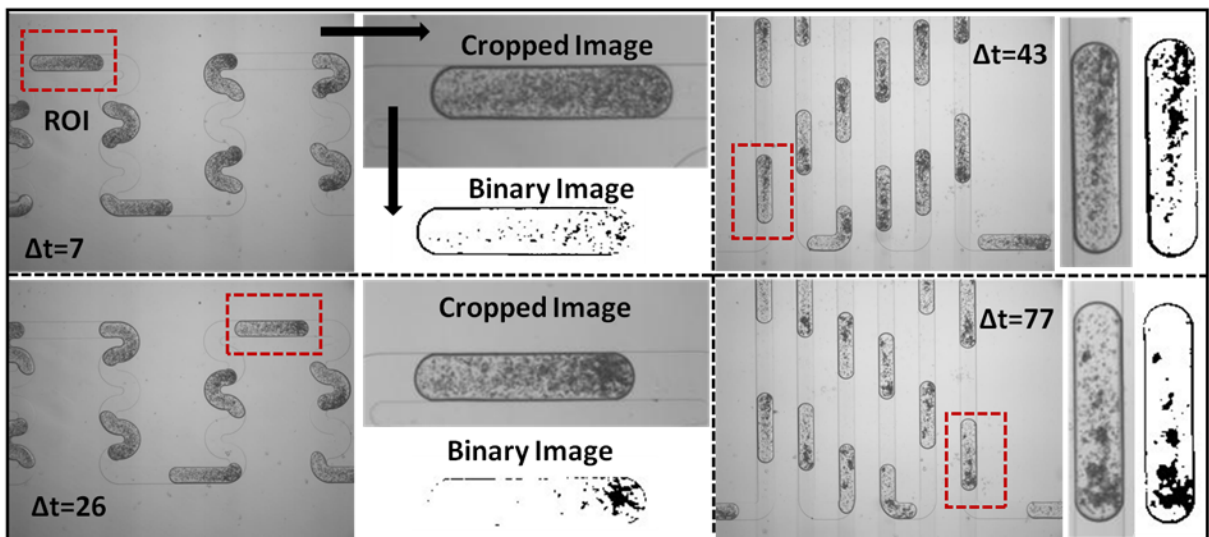


Figure 6.3: Illustration of the image analysis sequence and microscope images of droplets from different locations of the microfluidic channel. Videos of the droplet formation and reaction were recorded. Then each frame was extracted from the videos to be analyzed. Four regions of interests (ROI: 7s, 26s, 43s, 77s - red dashed rectangles) were selected. Then, the droplets passing those regions were analyzed by converting the images into binary images (black and white) to count the agglutinated red blood cells (clumps). The area of black region in the droplets indicated the agglutinated red blood cells. By measuring the clump size change over time in droplets passing through ROI, the end of the reaction was determined. Then, the reaction time was calculated.

## 6.4 Results and Discussions

The microfluidic device had two major components. The first section was the T-junction, where the droplets containing VLP stock and red blood cells were generated under the squeezing regime. These two reagents came in contact at the Y-junction and flowed in parallel before coming to the T-junction (see Figure 6.4a). Control of fluid flow was achieved using a pressure pump. The second section was the serpentine channels where the mixing of the two reagents in droplets occurred (see Figure 6.4b,c). As the HA protein attaches the red blood cells, dispersed red blood cells separated from the buffer solution and formed a clump of red blood cells within the droplet. The reaction started at the beginning of the Y-junction, where the two fluids met and was completed once the red blood cells were agglutinated and formed a lattice (clump) in the droplet, as shown in Figure 6.4c.

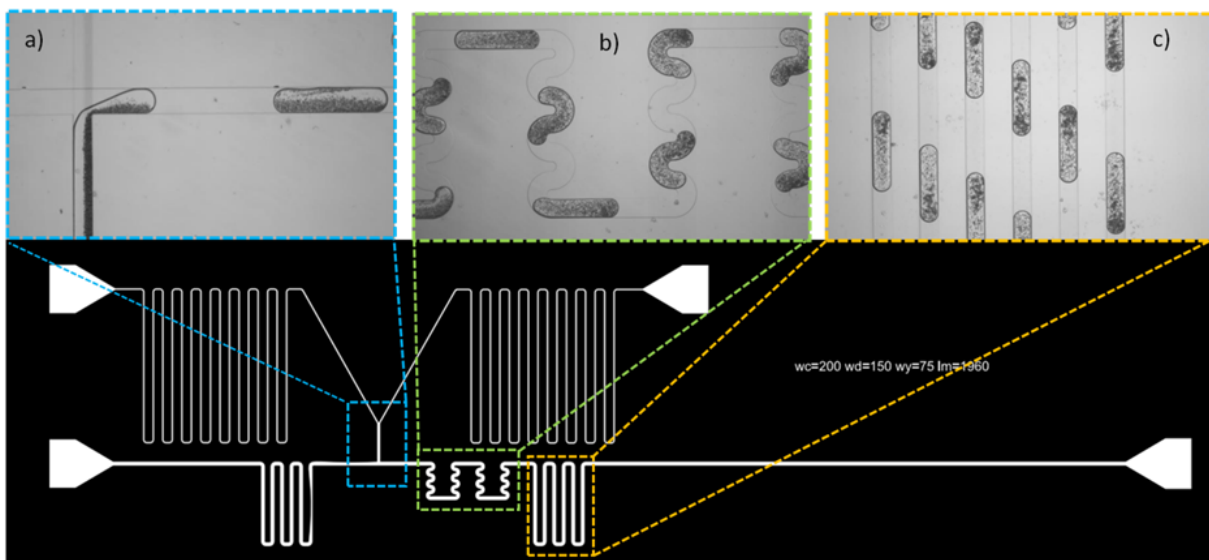


Figure 6.4: Schematic of the microfluidic device and microscope images of droplets in certain sections of the channel a) Two-phases flew in parallel through the Y-junction and droplets were generated at the T-junction (blue dashed rectangle) b, c) Mixing of reagents started at the dense turns and the reaction in droplet was complete as the agglutinated red blood cells (clumps) were formed in the mixing region (yellow and orange rectangles).

To evaluate the evolution of the clump of red blood cells, videos of the droplet flowing through the different locations of the channel were recorded. Each experiment was done using a single chip and in each experiment, 20 droplets were recorded to take the average of the reaction output. Then, individual droplets were analyzed using ImageJ. A minimal agglutinated RBC (clump) pixel size ( $\sim 20 \mu\text{m}$ ) was determined to differentiate the agglutinated from non-agglutinated red blood cells in the droplets. Clumped RBCs gathered at the front of the droplet. However, non-agglutinated RBCs were homogeneously distributed in the droplets under the same flow condition when HA was not present. Therefore, minimal particle size remained the same as the droplet flew through the outlet of the channel (see Figure 6.5 - blue line). However, at the presence of reaction, agglutinated red blood cell size increased over time and reached a plateau where red blood cells no longer combined, as shown in Figure 6.5 - red line. Furthermore, video analysis showed that the reaction was completed in 60 s while it takes around 5 hours in standard 96-well plates [104]. Thus, one can conclude that the reaction time was reduced by utilizing the small diffusion length of the droplet-based microfluidic systems.

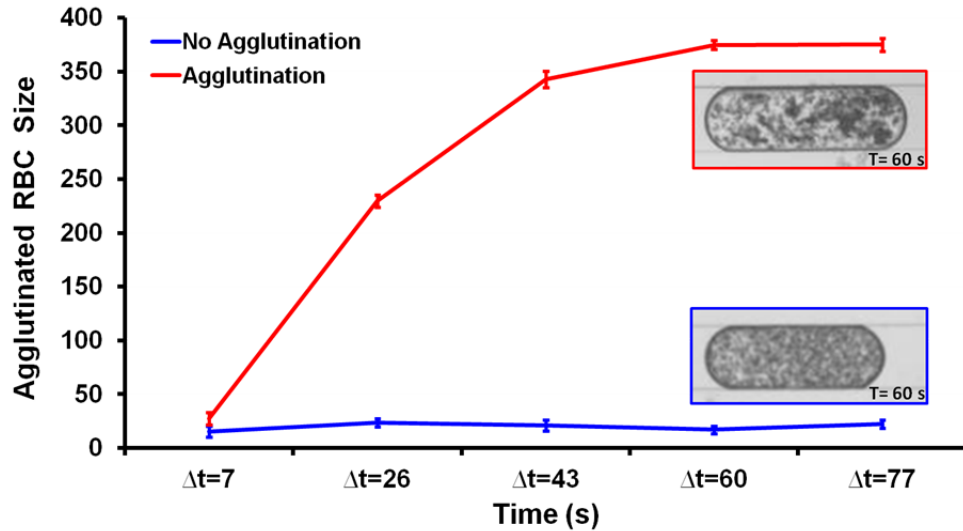


Figure 6.5: Agglutinated red blood cells (RBC) size ( $\mu\text{m}$ ) measurement in droplets over time. The red line indicates the presence of agglutination in droplets (undiluted stock of known HA activity) in one chip (Chip 1); the blue line represents no reaction in droplets ( $12^{\text{th}}$  dilution of stock of known HA activity) in another chip (Chip 2). The applied pressures were the same ( $P_{oil}=300$  mBar,  $P_{RBC}=290$  mBar,  $P_{HA}=290$  mBar) for both experiments.  $N=20$  droplets were recorded for each chip (Chip 1 and 2) in a single run.

### 6.4.1 Effect of Red Blood Cell Concentration on Reaction

To evaluate the effect of red blood cell concentration on reaction dynamics, red blood cells were diluted off-chip with phosphate buffer solution (PBS) to 10% and 50% RBCs. Cells were mixed with the same concentration of VLP stock (VLP containing HA, NA and M1 and having known HA activity) in microdroplets. Under the same flow conditions, VLP stock concentration and droplet size, larger agglutinated RBC sizes were measured for higher RBC concentrations. It is likely that this was due to the increase in available binding sites that were present with the increased number of cells. However, as shown in Figure 6.6 - red line, with lower concentrations of the red blood cells (Figure 6.6 - blue and green lines), clump formation saturated around 43 s resulting in much faster reaction time compared to agglutination of undiluted RBCs (100% - red line).

In standard 96-well plates, a higher concentration of red blood hindered the analysis, as shown in Figure 6.7. However, the microfluidic system was able to use different cell concentrations, all with acceptable linearity ( $R^2=0.9448$  and  $p=0.000179$ ). These experi-

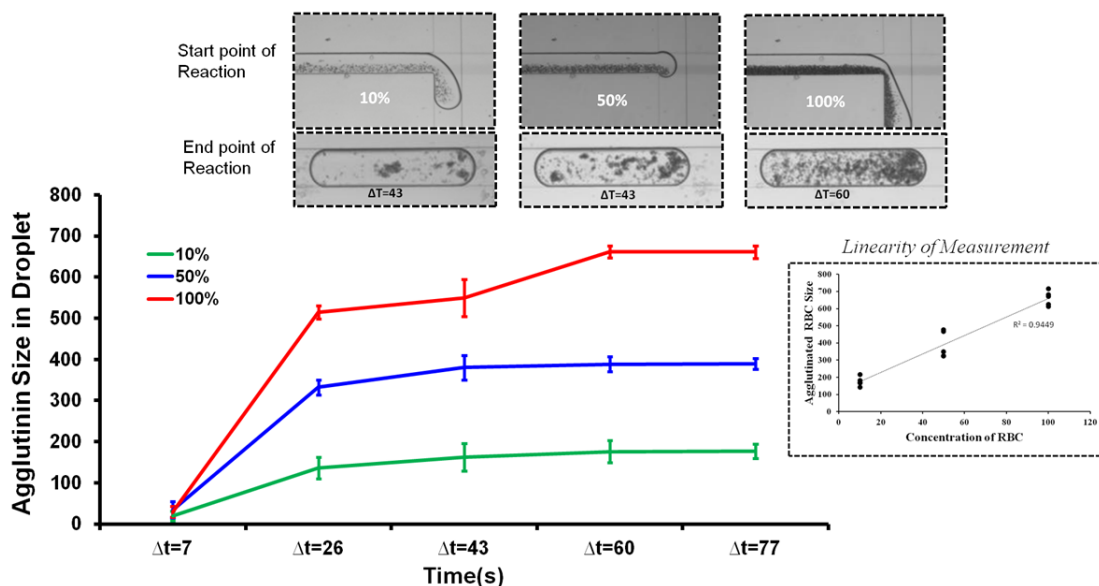


Figure 6.6: Effect of RBC concentration on hemagglutination reaction in microdroplets. The red line shows non-diluted red blood cell concentration in Chip 3, the blue line shows 50% RBC concentration in Chip 4, and the green line shows 10% RBC concentration in Chip 5. Flow conditions were kept the same for all three experiments ( $P_{oil}=300$  mBar,  $P_{RBC}=290$  mBar,  $P_{HA}=290$  mBar). Reaction ended after 43 s for lower concentrations of RBCs due to the excess virus stock per cell. However, the reaction ended after 60 s in undiluted RBC sample. Right graph represents the system linearity of a quantification assay where  $R^2=0.94$ .  $N=20$  droplets were recorded for each chip (Chip 3, 4 and 5) in a single run.

ments were done using three separate microfluidic chips for each concentrations of RBCs (Chip 3 for 100% RBC, Chip 4 for 50%RBC, and Chip 5 for 10%RBC). Then, the reaction was observed and analyzed on 20 different droplets for each set of experiment. Also, a difference in reaction time for various concentrations could not be detected when higher RBC concentration was used in the 96-well plate assay.

### 6.4.2 Effect of Mixing Ratio on Reaction

Previous experiments were completed by mixing an equal volume of the two dispersed phases. In this experiment, the mixing ratio was changed, and the VLP stock volume that

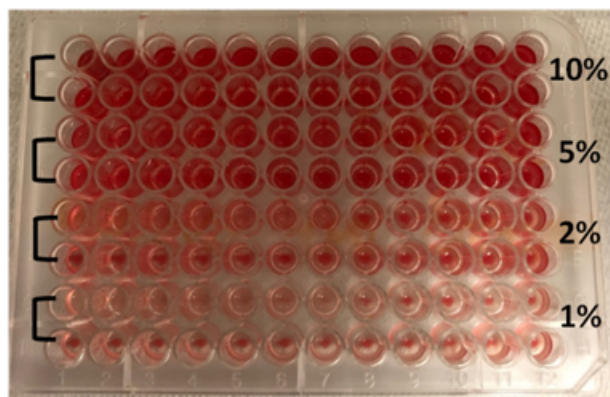


Figure 6.7: Photograph of hemagglutination reaction in 96-well plate for various RBC concentrations (from 1% to 10%). Reaction became undetectable in higher RBC concentration by naked-eye in 96-well plate.

was encapsulated in the droplet was increased (RBC : VLP = 1:3 - Chip 6). To make comparisons with previous experiments that had a 1:1 (RBC : VLP - Chip 1) mixing ratio, pressures of phases were fine-tuned to have similar droplet size and speed. As shown in Figure 6.8, the reaction was completed much faster in droplets where a larger volume of VLP stock was encapsulated ( $\sim 32$  s). Furthermore, smaller agglutinated RBC size was recorded. The amount of HA activity from larger volume fraction of VLP solution (3:1) increased the rate towards a constant agglutinated RBC size ( $\sim 43$  s).

### 6.4.3 Effect of Droplet Size on Reaction

Flow topology of the moving droplet in a rectangular channel is a complex concept, and the flow field inside the droplet depends on various parameters such capillary number, interfacial tension, droplet shape and the viscosity of fluids [44], [65], [57]. Therefore, it was assumed that changing droplet size may affect the RBC flow resulting in variations in the duration of the reaction. To investigate the effect of droplet size on the reaction, larger droplets were formed by increasing the applied pressure to the continuous phase while keeping the dispersed phase pressure constant. As a result, droplets of length  $\sim 900 \mu\text{m}$  and  $\sim 600 \mu\text{m}$  were compared. For both experiments, the same concentration of RBC and VLP stock were used. As shown in Figure 6.9, reaction time did not vary as the droplet size increased; the agglutination was completed around 60 s for both droplet sizes. Larger agglutinated RBC size was measured in the larger droplet likely due to the

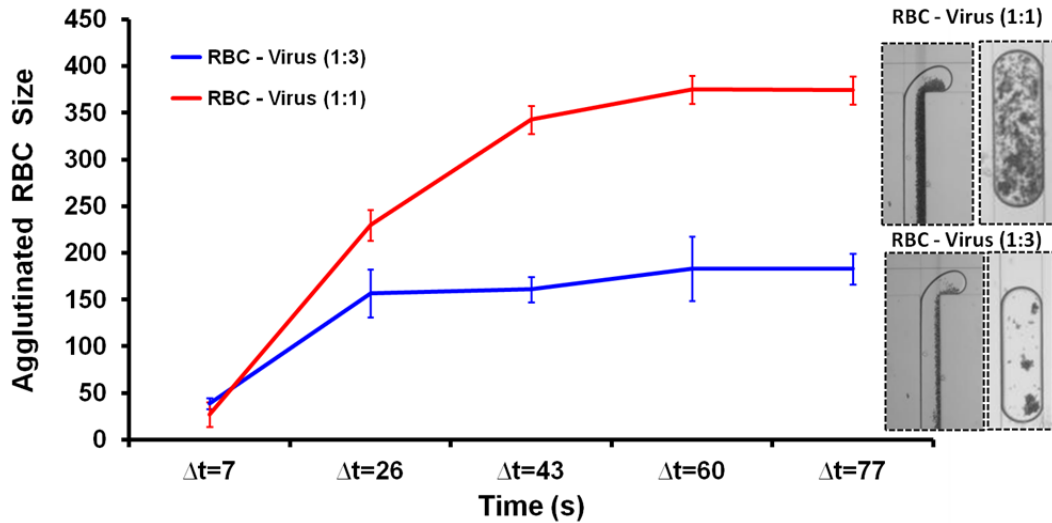


Figure 6.8: Effect of different mixing ratio of the reagents on the reaction. The flow conditions were kept the same for all experiments ( $P_{oil}=300$  mBar,  $P_{RBC}=290$  mBar,  $P_{HA}=290$  mBar and droplets were generated in similar sizes). Blue line indicates the larger virus fraction sample where the reaction ended after 32 s (Chip 1) and red line indicates the droplet encapsulated the equal volume of reagents where the reaction ended after 60 s (Chip 6).  $N=20$  droplets were recorded for each chip (Chip 1 and 6) in a single run.

increased number of cells that were encapsulated in the droplet (Figure 6.9 - red line).

#### 6.4.4 Effect of Red Blood Cell Freshness on Reaction

It has been shown that agglutination varies depending on the freshness of the RBCs [46]. As the red blood cells stored in a EDTA tube, they start to lose their cell integrity, deformability and decay over time. Therefore, available binding sites on the red blood cells surfaces change over time. To test the impact of this factor on the reaction, we tested two different red blood samples. The first sample was freshly collected and tested before its expiration date and the second sample was the red blood sample that was expired and stored in the EDTA tube for a day after its expiration date. The impact of RBC freshness was investigated in different droplet sizes. In a fresh RBC sample, the reaction time did not change in either droplet size; all reactions were completed after 60 s, as shown in Figure

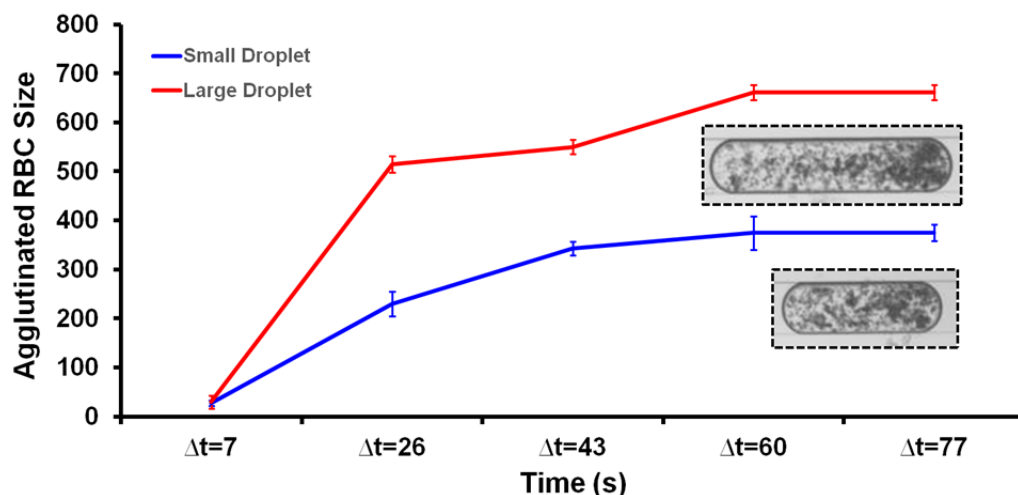


Figure 6.9: The effect of droplet size on the reaction. The red line represents the larger droplet ( $P_{oil}=300$  mBar and  $P_{HA}$ ,  $P_{RBC}=290$  mBar) - Chip 7. The blue line represents the smaller droplet ( $P_{oil}= 310$  mBar  $P_{RBC}$ ,  $P_{HA}= 290$  mBar) - Chip 8. Reaction ended in a similar time for both cases. However, a smaller clump size was measured in small droplets due to number of cells encapsulated in droplets.  $N=20$  droplets were recorded for each chip (Chip 7 and 8) in a single run.

6.10 - red and green lines (Chip 9, 10). However, larger clumps of RBCs were formed in either droplet size due to the more available binding sites of the fresh RBCs.

#### 6.4.5 Effect of Type of Virus-Like Particle Stock on Reaction

Three different preparations having different levels of HA activity were used to see if the differences could be detected by the microfluidic assay. When the different preparations were tested in a droplet-based microfluidic system, similar results were achieved to what was observed from the 96-well assay, as shown in Figure 6.11. As shown in Figure 6.12, a smaller agglutinated RBC size was measured for the HA-NA-M1 preparation than for the GAG-GFP-HA preparation; however, in small droplets, the differences were insignificant. Also, the reaction time for all preparations was similar for all droplet sizes.

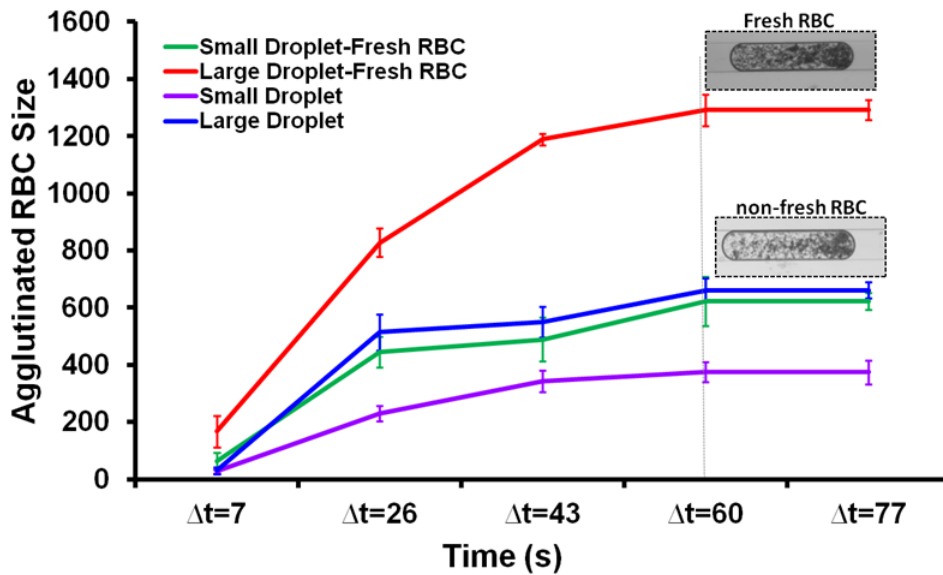


Figure 6.10: Effect of red blood cell freshness on the reaction. Green-red lines indicate the fresh red blood cell samples (1st day of red blood cell collection - Chip 9 and 10) in different droplet sizes. Blue-purple lines indicate the non-fresh red blood cell sample (6th day of the red blood cell collection - Chip 10 and 11) in different sizes of droplets. Reaction ended in 60 s for all cases but the clumps size was bigger in fresh samples.  $N=20$  droplets were recorded for each chip (Chip 9, 10, 11 and 12) in a single run. ( $P_{oil}=300$  mBar and  $P_{HA}, P_{RBC}=290$  mBar).



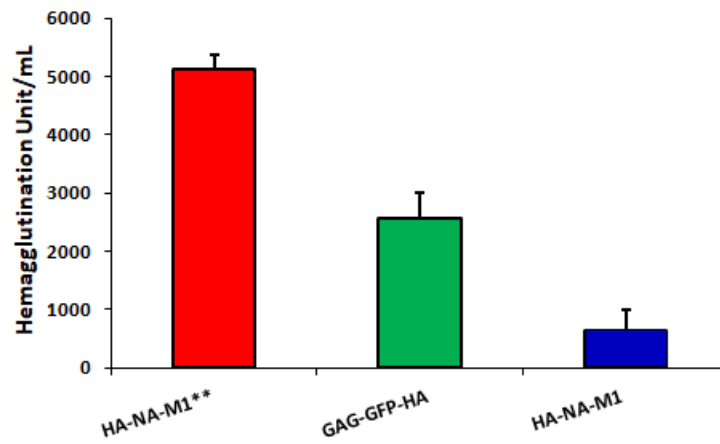


Figure 6.11: HA activity of the three different preparations with 3 replicates in 96-well plates. Three different VLPs were analyzed. Asterisk (\*\*) indicates freshly prepared material, while the HA-NA-M1 VLP was prepared eight months earlier and stored at 4° C. GAG-GFP-HA was another construct of the Virus Like Particle. Highest HA activity was measured in freshly prepared HA-NA-M1\*\* virus stock.

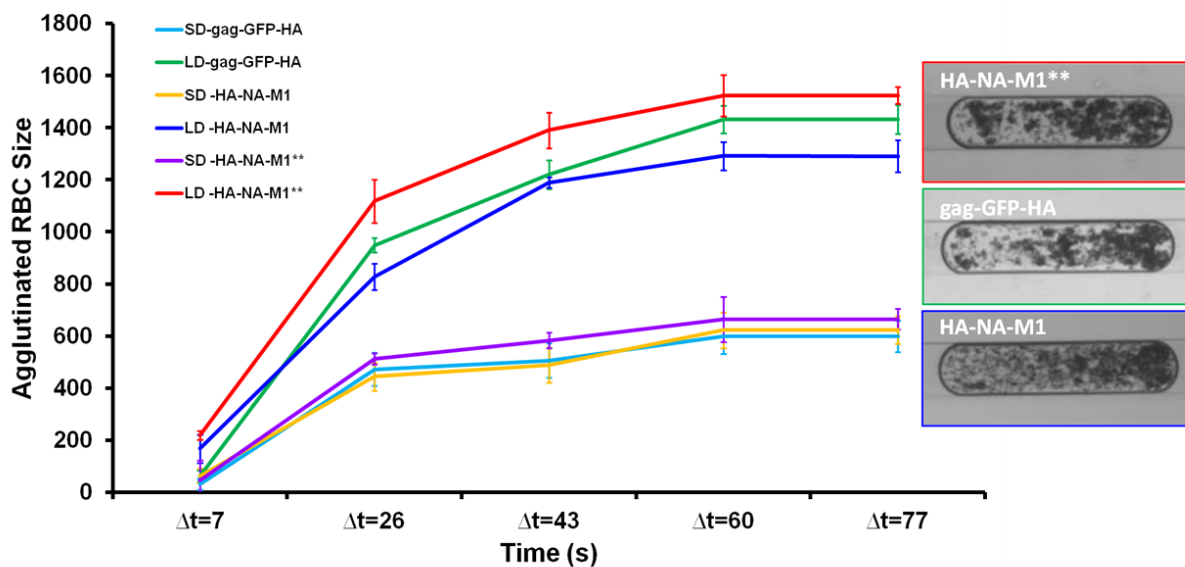


Figure 6.12: Effect of virus type on the reaction for two different droplet sizes for each virus type. Red-green-blue lines represent the larger droplets, while yellow-light blue-purple represent smaller droplets. Reaction was similar in all types and highest HA activity was observed in the freshly prepared HA-NA-M1\*\* virus stock similar to the 96-well plate results. N=20 droplets were recorded for each chip (Chip 13-red line, 14-green line, 15-blue line, 16-purple line, 17-light-blue line, 18-yellow line) in a single run. were used for each virus preparations to prevent cross-contamination. ( $P_{oil}=300$  mBar and  $P_{HA}$ ,  $P_{RBC}=290$  mBar, for larger droplets), ( $P_{oil}= 310$  mBar  $P_{RBC}$ ,  $P_{HA}= 290$  mBar, for smaller droplets).

### 6.4.6 Performance of the Quantification System

A standard 96-well hemagglutination assay limit of detection is approximately 2 HAU/50  $\mu\text{L}$  [46], [104]. For the fresh HA-NA-M1\*\* preparation, the HA activity was 2560 HAU/50  $\mu\text{L}$ . To examine the limit of detection in the microfluidic assay, dilutions of this preparation were used and examined in the device. The minimum concentration of HA activity that could be detected in the microfluidic device was  $1.25 \times 10^{-4}$  HAU/  $\mu\text{L}$  or 0.625 HAU/50  $\mu\text{L}$  (Figure 6.13). It should be noted, however, only 0.004  $\mu\text{L}$  is required at that concentration. Future work should look into the limit of detection by increasing the mixing ratio at low HA concentrations.

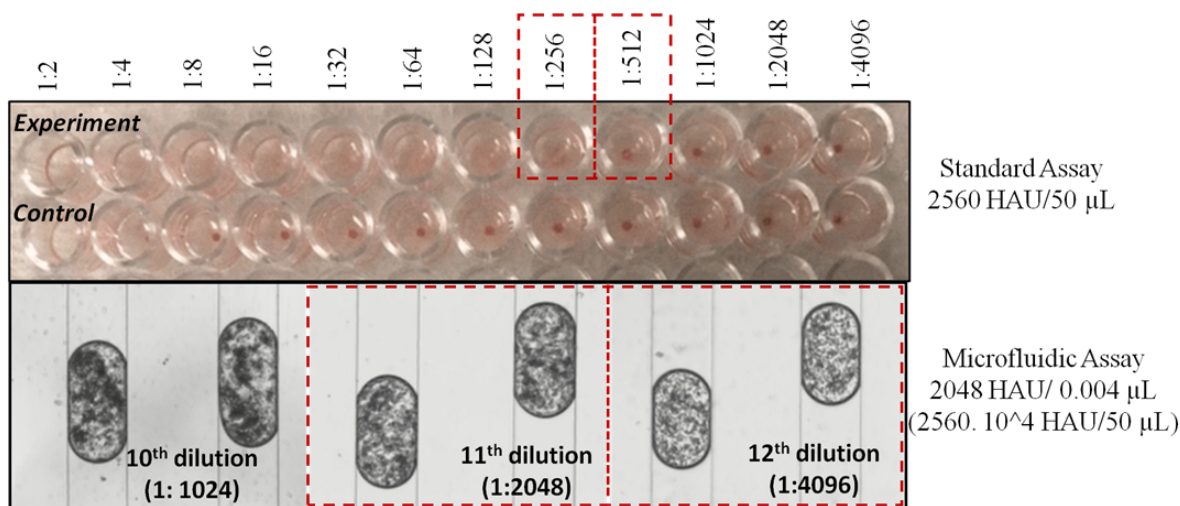


Figure 6.13: Comparison of the standard HA assay with the microfluidic system in terms of the limit of the detection. Top figure represents the HA assay in 96-well plate of a given virus stock (HA-NA-M1\*\*). Agglutination reaction ended at the 8<sup>th</sup> (Chip 19) dilution of the sample. However, when the same samples were transferred into the microfluidic chip, the reaction was still observable at the 11<sup>th</sup> (Chip 22) dilution of the virus stock which proves the greater sensitivity of the droplet based microfluidic system over the standard assay.

## 6.5 Conclusion

In this study, a droplet-based microfluidic device was reported, which can quantify HA activity in different VLP preparations. Droplets that included Influenza virus like particles were mixed with a red blood cell solution to form hemagglutination reactions in droplets. The formation of agglutinated red blood cells was quantified using image analysis. The performance of the quantification method was investigated by analyzing the impact of several parameters which affect the hemagglutination assay such as cell concentration, VLP preparations, and sample freshness. Furthermore, the impact of flow conditions of the fluidic network on the reaction was tested by varying the droplet size. The presented device provides a method that allows quantifying the samples in a robust manner. This study also demonstrates a sensitive label-free method, which makes this method a new candidate for an automated hemagglutination assay.

### Symbols and Nomenclature

PE  
SRID  
ELISA  
RP-HPLC  
TEM  
DLS  
LC-MS  
EDTA  
Sf9  
HAU  
PBS  
MOI  
GFP RFP

# Chapter 7

## Contributions to the Field and Recommendation for Future Studies

### 7.1 Contributions to the Field

Droplet-based microfluidic systems improve biochemical assay performance due to the fast reaction time, increased sensitivity and less reagent consumption. Depending on the application, there are several functions of droplet microfluidics that need to be coupled in a microfluidic network. For example, in this study, droplet generation was coupled with mixing of reagents to develop a more sensitive hemagglutination assay that can be used to evaluate VLP preparations. The ability of microfluidic systems to form monodisperse droplets eliminates variability in repeated reactions, leading to smaller standard deviations in results. One complicating aspect of biological fluids is that they tend to be non-Newtonian. The literature surrounding non-Newtonian fluids in microfluidic channels is sparse. Therefore, we undertook studies to show how to design a microfluidic device that works for these biological non-Newtonian fluids.

This work focused on T-junction droplet generators. Dimensionless parameters that affected formation dynamics were analyzed. Video analysis showed that droplets of RBC in solution formed in three stages (lag, filling and necking stages). The lag stage was only observed for narrower dispersed phase channel designs. The filling stage was affected by the aspect ratio. The necking stage was mostly affected by the fluid viscosities. All these findings were considered in the modeling of each stage. A final model of droplet formation covered all dependencies such as channel geometry, flow rate ratios, fluid properties and capillary number, which is different from Newtonian fluids where only channel geometry is

the governing factor in the squeezing regime. With the optimized experimental condition provided in this study, one can design a generator for monodisperse RBC solution droplets for further biochemical assay applications.

The next phase of research was the development of a droplet-based microfluidic device to quantify the HA activity of virus-like particle preparations. This system required a robust microfluidic device design that coupled generation and mixing modules. By using the model and the analysis in Chapter 4 and 5, an appropriate T-junction geometry was designed to produce droplets of desired size and at a desired frequency. The design consisted of a Y-junction, where two reagents of interest flowed in parallel without diffusing into each other before droplet generation, a T-junction, where droplets formed, and a mixing region, where serpentine channels were located for enhancing mixing of reagents in droplets. As the two reagents mixed, the aggregation reaction started, and the design enabled label-free observation of the evolution of reaction in real-time. To further test the performance of the method, variables affecting aggregation such as red blood cell concentration, VLP preparation, and freshness of samples were investigated. A comparison of the quantification results with the standard methods showed that the droplet-based microfluidic system provides faster and more sensitive quantification. Therefore, this study closes the gap between research and commercial methods and provides a new methodology for advancing the field.

## 7.2 Recommendations for Future Work

In this study, the dynamics of biological non-Newtonian droplets were analyzed, and a mathematical model was developed by this analysis. Although the model presented in this study predicts well the operation parameters, there are several aspects to be furthered studied. For example, the focus of this study was only generation under the squeezing regime. Therefore, other generation regimes should be evaluated to see if RBC solution droplets can be generated. In addition, red blood cell droplet formation dynamics can be evaluated using other droplet generators like flow focusing device. The influence of surfactant on formation dynamics has not been investigated in this study and could play a role in other types of blood analysis.

The method developed for quantification of HA activity of VLP preparations can be further developed by eliminating bulky fluid handling systems and dependence on a large microscope and turning the system into point of care device. By integrating a benchtop pressure pump, a small camera, and a microfluidic chip, the system can be automated. In this study, association and dissociation kinetics have not been studied. However, the

binding kinetics of different virus strains can be analyzed with the help of the system's ability to image reaction in real-time as well as to detect precisely.

# References

- [1] Paul Abbyad, Pierre-Louis Tharaux, Jean-Louis Martin, Charles N Baroud, and Antigoni Alexandrou. Sickling of red blood cells through rapid oxygen exchange in microfluidic drops. *Lab on a Chip*, 10(19):2505–2512, 2010.
- [2] Brian J Adzima and Sachin S Velankar. Pressure drops for droplet flows in microfluidic channels. *Journal of Micromechanics and Microengineering*, 16(8):1504, 2006.
- [3] Vladimir S Ajaev and GM Homsy. Modeling shapes and dynamics of confined bubbles. *Annu. Rev. Fluid Mech.*, 38:277–307, 2006.
- [4] Sarah Al-Roubaie, Espen D Jahnsen, Masud Mohammed, Caitlin Henderson-Toth, and Elizabeth AV Jones. Rheology of embryonic avian blood. *American Journal of Physiology-Heart and Circulatory Physiology*, 301(6):H2473–H2481, 2011.
- [5] Shelley L Anna, Nathalie Bontoux, and Howard A Stone. Formation of dispersions using “flow focusing” in microchannels. *Applied physics letters*, 82(3):364–366, 2003.
- [6] Shelley L Anna and Hans C Mayer. Microscale tipstreaming in a microfluidic flow focusing device. *Physics of Fluids*, 18(12):121512, 2006.
- [7] K Apostolov and B Fishman. Purification and concentration of influenza virus by auto-aggregation. *Nature*, 215(5107):1287–1288, 1967.
- [8] Charles N Baroud, Francois Gallaire, and Rémi Dangla. Dynamics of microfluidic droplets. *Lab on a Chip*, 10(16):2032–2045, 2010.
- [9] Michael Betenbaugh, Manching Yu, Kathleen Kuehl, John White, David Pennock, Kristin Spik, and Connie Schmaljohn. Nucleocapsid-and virus-like particles assemble in cells infected with recombinant baculoviruses or vaccinia viruses expressing the m and the s segments of hantaan virus. *Virus research*, 38(2-3):111–124, 1995.



- [10] Nicolas Bremond, Abdou R Thiam, and Jérôme Bibette. Decompressing emulsion droplets favors coalescence. *Physical review letters*, 100(2):024501, 2008.
- [11] Francis Patton Bretherton. The motion of long bubbles in tubes. *Journal of Fluid Mechanics*, 10(2):166–188, 1961.
- [12] Michelle R Bringer, Cory J Gerdts, Helen Song, Joshua D Tice, and Rustem F Ismagilov. Microfluidic systems for chemical kinetics that rely on chaotic mixing in droplets. *Philosophical Transactions of the Royal Society of London. Series A: Mathematical, Physical and Engineering Sciences*, 362(1818):1087–1104, 2004.
- [13] Henrik Bruus. *Theoretical microfluidics*, volume 18. Oxford university press Oxford, 2008.
- [14] Elena Castro-Hernandez, Venkata Gundabala, Alberto Fernández-Nieves, and Jose Manuel Gordillo. Scaling the drop size in coflow experiments. *New Journal of Physics*, 11(7):075021, 2009.
- [15] Zhuang Zhi Chong, Say Hwa Tan, Alfonso M Gañán-Calvo, Shu Beng Tor, Ngiap Hiang Loh, and Nam-Trung Nguyen. Active droplet generation in microfluidics. *Lab on a Chip*, 16(1):35–58, 2016.
- [16] Gordon F Christopher and Shelly L Anna. Microfluidic methods for generating continuous droplet streams. *Journal of Physics D: Applied Physics*, 40(19):R319, 2007.
- [17] Gordon F Christopher, N Nadia Noharuddin, Joshua A Taylor, and Shelley L Anna. Experimental observations of the squeezing-to-dripping transition in t-shaped microfluidic junctions. *Physical Review E*, 78(3):036317, 2008.
- [18] Lisa M Churgay, Steven Kovacevic, Frank C Tinsley, Cheryl M Kussow, Rohn L Millican, James R Miller, and John E Hale. Purification and characterization of secreted human leptin produced in baculovirus-infected insect cells. *Gene*, 190(1):131–137, 1997.
- [19] Juan A Claver and Agustin IE Quaglia. Comparative morphology, development, and function of blood cells in nonmammalian vertebrates. *Journal of exotic pet medicine*, 18(2):87–97, 2009.
- [20] Ana Letícia Rodrigues Costa, Andresa Gomes, and Rosiane Lopes Cunha. Studies of droplets formation regime and actual flow rate of liquid-liquid flows in flow-focusing microfluidic devices. *Experimental Thermal and Fluid Science*, 85:167–175, 2017.

- [21] Carsten Cramer, Peter Fischer, and Erich J Windhab. Drop formation in a co-flowing ambient fluid. *Chemical Engineering Science*, 59(15):3045–3058, 2004.
- [22] Marybeth C Creskey, Changgui Li, Junzhi Wang, Michel Girard, Barry Lorbetkie, Caroline Gravel, Aaron Farnsworth, Xuguang Li, Daryl GS Smith, and Terry D Cyr. Simultaneous quantification of the viral antigens hemagglutinin and neuraminidase in influenza vaccines by lc–mse. *Vaccine*, 30(32):4762–4770, 2012.
- [23] Rémi Dangla, François Gallaire, and Charles N Baroud. Microchannel deformations due to solvent-induced pdms swelling. *Lab on a Chip*, 10(21):2972–2978, 2010.
- [24] M De Menech, Piotr Garstecki, F Jousse, and Howard A Stone. Transition from squeezing to dripping in a microfluidic t-shaped junction. *journal of fluid mechanics*, 595:141–161, 2008.
- [25] Wei Du, Taotao Fu, Qindan Zhang, Chunying Zhu, Youguang Ma, and Huai Z Li. Breakup dynamics for droplet formation in a flow-focusing device: Rupture position of viscoelastic thread from matrix. *Chemical Engineering Science*, 153:255–269, 2016.
- [26] Jules Dupire, Marius Socol, and Annie Viallat. Full dynamics of a red blood cell in shear flow. *Proceedings of the National Academy of Sciences*, 109(51):20808–20813, 2012.
- [27] Randall M Erb, Dominik Obrist, Philipp W Chen, Julia Studer, and André R Stuard. Predicting sizes of droplets made by microfluidic flow-induced dripping. *Soft Matter*, 7(19):8757–8761, 2011.
- [28] MR Fedde and RF Wideman Jr. Blood viscosity in broilers: influence on pulmonary hypertension syndrome. *Poultry science*, 75(10):1261–1267, 1996.
- [29] Kathryn Diane Fink. *Microfluidic Analysis of Vertebrate Red Blood Cell Characteristics*. PhD thesis, UC Berkeley, 2016.
- [30] Center for Disease Control and Prevention. Antigenic characterization. <https://www.cdc.gov/flu/about/professionals/antigenic.htm>, October 2019.
- [31] Ron AM Fouchier, Vincent Munster, Anders Wallensten, Theo M Bestebroer, Sander Herfst, Derek Smith, Guus F Rimmelzwaan, Björn Olsen, and Albert DME Osterhaus. Characterization of a novel influenza a virus hemagglutinin subtype (h16) obtained from black-headed gulls. *Journal of virology*, 79(5):2814–2822, 2005.

- [32] Michael J Fuerstman, Ann Lai, Meghan E Thurlow, Sergey S Shevkoplyas, Howard A Stone, and George M Whitesides. The pressure drop along rectangular microchannels containing bubbles. *Lab on a Chip*, 7(11):1479–1489, 2007.
- [33] C Joel Funk and Richard A Consigli. Phosphate cycling on the basic protein of plodia interpunctella granulosis virus. *Virology*, 193(1):396–402, 1993.
- [34] Piotr Garstecki, Michael J Fuerstman, Howard A Stone, and George M Whitesides. Formation of droplets and bubbles in a microfluidic t-junction—scaling and mechanism of break-up. *Lab on a Chip*, 6(3):437–446, 2006.
- [35] Steve George. Use and control of co-expression in the baculovirus-insect cell system for the production of multiple proteins and complex biologics. 2016.
- [36] Tomasz Glowinski. Droplet production and transport in microfluidic networks with pressure driven flow control. 2012.
- [37] Elizabeth VL Grgacic and David A Anderson. Virus-like particles: passport to immune recognition. *Methods*, 40(1):60–65, 2006.
- [38] Zhipeng Gu and Jong-Leng Liow. Micro-droplet formation with non-newtonian solutions in microfluidic t-junctions with different inlet angles. In *2012 7th IEEE International Conference on Nano/Micro Engineered and Molecular Systems (NEMS)*, pages 423–428. IEEE, 2012.
- [39] Axel Günther and Klavs F Jensen. Multiphase microfluidics: from flow characteristics to chemical and materials synthesis. *Lab on a Chip*, 6(12):1487–1503, 2006.
- [40] Amit Gupta, SM Sohel Murshed, and Ranganathan Kumar. Droplet formation and stability of flows in a microfluidic t-junction. *Applied physics letters*, 94(16):164107, 2009.
- [41] Gery P Guy Jr, Kun Zhang, Michele K Bohm, Jan Losby, Brian Lewis, Randall Young, Louise B Murphy, and Deborah Dowell. Vital signs: changes in opioid prescribing in the united states, 2006–2015. *MMWR. Morbidity and mortality weekly report*, 66(26):697, 2017.
- [42] Michinao Hashimoto, Piotr Garstecki, Howard A Stone, and George M Whitesides. Interfacial instabilities in a microfluidic hele-shaw cell. *Soft Matter*, 4(7):1403–1413, 2008.

- [43] CM Hawkey, PM Bennett, SC Gascoyne, MG Hart, and JK Kirkwood. Erythrocyte size, number and haemoglobin content in vertebrates. *British journal of haematology*, 77(3):392–397, 1991.
- [44] Michael Hein, Michael Moskopp, and Ralf Seemann. Flow field induced particle accumulation inside droplets in rectangular channels. *Lab on a Chip*, 15(13):2879–2886, 2015.
- [45] Frank S Heldt, Sascha Y Kupke, Sebastian Dörl, Udo Reichl, and Timo Frensing. Single-cell analysis and stochastic modelling unveil large cell-to-cell variability in influenza a virus infection. *Nature communications*, 6(1):1–12, 2015.
- [46] George K Hirst. The quantitative determination of influenza virus and antibodies by means of red cell agglutination. *The Journal of experimental medicine*, 75(1):49, 1942.
- [47] SR Hodges, OE Jensen, and JM Rallison. The motion of a viscous drop through a cylindrical tube. *Journal of fluid mechanics*, 501:279–301, 2004.
- [48] C Holtze, AC Rowat, JJ Agresti, JB Hutchison, FE Angile, CHJ Schmitz, Sarah Köster, H Duan, KJ Humphry, RA Scanga, et al. Biocompatible surfactants for water-in-fluorocarbon emulsions. *Lab on a Chip*, 8(10):1632–1639, 2008.
- [49] Joeska Husny and Justin J Cooper-White. The effect of elasticity on drop creation in t-shaped microchannels. *Journal of non-newtonian fluid mechanics*, 137(1-3):121–136, 2006.
- [50] L Ikonomou, Y-J Schneider, and SN Agathos. Insect cell culture for industrial production of recombinant proteins. *Applied microbiology and biotechnology*, 62(1):1–20, 2003.
- [51] Sławomir Jakiela, Sylwia Makulska, Piotr M Korczyk, and Piotr Garstecki. Speed of flow of individual droplets in microfluidic channels as a function of the capillary number, volume of droplets and contrast of viscosities. *Lab on a Chip*, 11(21):3603–3608, 2011.
- [52] Bert E Johansson, James T Matthews, and Edwin D Kilbourne. Supplementation of conventional influenza a vaccine with purified viral neuraminidase results in a balanced and broadened immune response. *Vaccine*, 16(9-10):1009–1015, 1998.

- [53] Hasnaa Jorio, Rosa Tran, and Amine Kamen. Stability of serum-free and purified baculovirus stocks under various storage conditions. *Biotechnology progress*, 22(1):319–325, 2006.
- [54] Bernd Kalbfuss, Anne Knöchlein, Tina Kröber, and Udo Reichl. Monitoring influenza virus content in vaccine production: precise assays for the quantitation of hemagglutination and neuraminidase activity. *Biologicals*, 36(3):145–161, 2008.
- [55] JC Kapteyn, AM Porre, EJP De Rond, WB Hessels, MA Tijms, H Kessen, AME Slotboom, MA Oerlemans, D Smit, J Van der Linden, et al. Hplc-based quantification of haemagglutinin in the production of egg-and mdck cell-derived influenza virus seasonal and pandemic vaccines. *Vaccine*, 27(9):1468–1477, 2009.
- [56] T Kawakatsu, G Trägårdh, Ch Trägårdh, M Nakajima, N Oda, and T Yonemoto. The effect of the hydrophobicity of microchannels and components in water and oil phases on droplet formation in microchannel water-in-oil emulsification. *Colloids and Surfaces A: Physicochemical and Engineering Aspects*, 179(1):29–37, 2001.
- [57] Haruyuki Kinoshita, Shohei Kaneda, Teruo Fujii, and Marie Oshima. Three-dimensional measurement and visualization of internal flow of a moving droplet using confocal micro-piv. *Lab on a Chip*, 7(3):338–346, 2007.
- [58] Timothy R Kline, Matthew K Runyon, Mohammad Pothiwala, and Rustem F Ismagilov. Abo, d blood typing and subtyping using plug-based microfluidics. *Analytical chemistry*, 80(16):6190–6197, 2008.
- [59] Laura R Kuck, Michelle Sorensen, Erin Matthews, Indresh Srivastava, Manon MJ Cox, and Kathy L Rowlen. Titer on chip: new analytical tool for influenza vaccine potency determination. *PLoS One*, 9(10):e109616, 2014.
- [60] Vincent Labrot, Michael Schindler, Pierre Guillot, Annie Colin, and Mathieu Joanicot. Extracting the hydrodynamic resistance of droplets from their behavior in microchannel networks. *Biomicrofluidics*, 3(1):012804, 2009.
- [61] Wingki Lee, Lynn M Walker, and Shelley L Anna. Role of geometry and fluid properties in droplet and thread formation processes in planar flow focusing. *Physics of Fluids*, 21(3):032103, 2009.
- [62] Kang-Yi Lien, Lien-Yu Hung, Tze-Bin Huang, Yi-Che Tsai, Huan-Yao Lei, and Gwo-Bin Lee. Rapid detection of influenza a virus infection utilizing an immunomagnetic

- bead-based microfluidic system. *Biosensors and Bioelectronics*, 26(9):3900–3907, 2011.
- [63] DR Link, Shelley L Anna, DA Weitz, and Howard A Stone. Geometrically mediated breakup of drops in microfluidic devices. *Physical review letters*, 92(5):054503, 2004.
- [64] Barry Lorbetskie, Jun Wang, Caroline Gravel, Cynthia Allen, Mike Walsh, Aline Rinfret, Xuguang Li, and Michel Girard. Optimization and qualification of a quantitative reversed-phase hplc method for hemagglutinin in influenza preparations and its comparative evaluation with biochemical assays. *Vaccine*, 29(18):3377–3389, 2011.
- [65] Shaohua Ma, Joseph M Sherwood, Wilhelm TS Huck, and Stavroula Balabani. On the flow topology inside droplets moving in rectangular microchannels. *Lab on a Chip*, 14(18):3611–3620, 2014.
- [66] Honest Makamba, Jin Ho Kim, Kwanseop Lim, Nokyoung Park, and Jong Hoon Hahn. Surface modification of poly (dimethylsiloxane) microchannels. *Electrophoresis*, 24(21):3607–3619, 2003.
- [67] Sylwia Makulska, Slawomir Jakiela, and Piotr Garstecki. A micro-rheological method for determination of blood type. *Lab on a Chip*, 13(14):2796–2801, 2013.
- [68] Carl-Fredrik Mandenius, Ronghui Wang, Anna Aldén, Gunnar Bergström, Sabine Thébault, Charles Lutsch, and Sten Ohlson. Monitoring of influenza virus hemagglutinin in process samples using weak affinity ligands and surface plasmon resonance. *Analytica chimica acta*, 623(1):66–75, 2008.
- [69] Merve Marcali and Caglar Elbuken. Impedimetric detection and lumped element modelling of a hemagglutination assay in microdroplets. *Lab on a Chip*, 16(13):2494–2503, 2016.
- [70] Daniel Mark, Stefan Haeberle, Günter Roth, Felix Von Stetten, and Roland Zengerle. Microfluidic lab-on-a-chip platforms: requirements, characteristics and applications. In *Microfluidics based microsystems*, pages 305–376. Springer, 2010.
- [71] Linas Mazutis, Ali Fallah Araghi, Oliver J Miller, Jean-Christophe Baret, Lucas Frenz, Agnes Janoshazi, Valérie Taly, Benjamin J Miller, J Brian Hutchison, Darren Link, et al. Droplet-based microfluidic systems for high-throughput single dna molecule isothermal amplification and analysis. *Analytical chemistry*, 81(12):4813–4821, 2009.

- [72] Matt McEvoy, Vladimir Razinkov, Ziping Wei, Jose R Casas-Finet, Guillermo I Tous, and Mark A Schenerman. Improved particle counting and size distribution determination of aggregated virus populations by asymmetric flow field-flow fractionation and multiangle light scattering techniques. *Biotechnology progress*, 27(2):547–554, 2011.
- [73] Ulrich Miessner, Ralph Lindken, and Jerry Westerweel. Velocity measurements in microscopic two-phase flows by means of micro piv. In *International Conference on Nanochannels, Microchannels, and Minichannels*, volume 48345, pages 1111–1118, 2008.
- [74] Metin Muradoglu and Howard A Stone. Mixing in a drop moving through a serpentine channel: A computational study. *Physics of Fluids*, 17(7):073305, 2005.
- [75] Gabriele Neumann, Takeshi Noda, and Yoshihiro Kawaoka. Emergence and pandemic potential of swine-origin h1n1 influenza virus. *Nature*, 459(7249):931–939, 2009.
- [76] Xize Niu, Shelly Gulati, Joshua B Edel, and Andrew J demello. Pillar-induced droplet merging in microfluidic circuits. *Lab on a Chip*, 8(11):1837–1841, 2008.
- [77] World Health Organization. Influenza. [https://www.who.int/news-room/fact-sheets/detail/influenza-\(seasonal\)](https://www.who.int/news-room/fact-sheets/detail/influenza-(seasonal)), November 2018.
- [78] Peter Pushko, Terrence M Tumpey, Fang Bu, John Knell, Robin Robinson, and Gale Smith. Influenza virus-like particles comprised of the ha, na, and m1 proteins of h9n2 influenza virus induce protective immune responses in balb/c mice. *Vaccine*, 23(50):5751–5759, 2005.
- [79] Armand J Quick and Lenore Clesceri. Influence of acetylsalicylic acid and salicylamide on the coagulation of blood. *Journal of Pharmacology and Experimental Therapeutics*, 128(1):95–98, 1960.
- [80] Eduardo Ramirez. Generation and characterization of dual-fluorescent influenza virus-like particles (vlps) in insect cells. Master’s thesis, University of Waterloo, 2019.
- [81] L Spencer Roach, Helen Song, and Rustem F Ismagilov. Controlling nonspecific protein adsorption in a plug-based microfluidic system by controlling interfacial chemistry using fluoruous-phase surfactants. *Analytical chemistry*, 77(3):785–796, 2005.
- [82] George F Rohrmann. *Baculovirus molecular biology*. 2013.

- [83] Behnam Rostami and Gian Luca Morini. Experimental characterization of a micro cross-junction as generator of newtonian and non-newtonian droplets in silicone oil flow at low capillary numbers. *Experimental Thermal and Fluid Science*, 103:191–200, 2019.
- [84] Amar Safdar and Manon MJ Cox. Baculovirus-expressed influenza vaccine: a novel technology for safe and expeditious vaccine production for human use. *Expert opinion on investigational drugs*, 16(7):927–934, 2007.
- [85] Long Sang, Yiping Hong, and Fujun Wang. Investigation of viscosity effect on droplet formation in t-shaped microchannels by numerical and analytical methods. *Microfluidics and Nanofluidics*, 6(5):621–635, 2009.
- [86] Michael Schindler and Armand Ajdari. Droplet traffic in microfluidic networks: A simple model for understanding and designing. *Physical Review Letters*, 100(4):044501, 2008.
- [87] DA Sessoms, Malika Belloul, Wilfried Engl, M Roche, L Courbin, and P Panizza. Droplet motion in microfluidic networks: Hydrodynamic interactions and pressure-drop measurements. *Physical Review E*, 80(1):016317, 2009.
- [88] Lingling Shui, Albert Van Den Berg, and Jan CT Eijkel. Interfacial tension controlled w/o and o/w 2-phase flows in microchannel. *Lab on a Chip*, 9(6):795–801, 2009.
- [89] Ajay Singh, Jonathan D Van Hamme, and Owen P Ward. Surfactants in microbiology and biotechnology: Part 2. application aspects. *Biotechnology advances*, 25(1):99–121, 2007.
- [90] Helen Song, Michelle R Bringer, Joshua D Tice, Cory J Gerdts, and Rustem F Ismagilov. Experimental test of scaling of mixing by chaotic advection in droplets moving through microfluidic channels. *Applied Physics Letters*, 83(22):4664–4666, 2003.
- [91] Helen Song, Hung-Wing Li, Matthew S Munson, Thuong G Van Ha, and Rustem F Ismagilov. On-chip titration of an anticoagulant argatroban and determination of the clotting time within whole blood or plasma using a plug-based microfluidic system. *Analytical chemistry*, 78(14):4839–4849, 2006.
- [92] Mira Song, Da-Young Park, Youngkwan Kim, Kyung-Jin Lee, Zhe Lu, Kinarm Ko, Young Kug Choo, Yeon Soo Han, Mi-Hyun Ahn, Doo-Byoung Oh, et al. Characterization of n-glycan structures and biofunction of anti-colorectal cancer monoclonal



- antibody co17-1a produced in baculovirus-insect cell expression system. *Journal of bioscience and bioengineering*, 110(2):135–140, 2010.
- [93] Yang Song, Alban Sauret, and Ho Cheung Shum. All-aqueous multiphase microfluidics. *Biomicrofluidics*, 7(6):061301, 2013.
- [94] Todd M Squires and Stephen R Quake. Microfluidics: Fluid physics at the nanoliter scale. *Reviews of modern physics*, 77(3):977, 2005.
- [95] Kathleen J Stebe, Shi-Yow Lin, and Charles Maldarelli. Remobilizing surfactant retarded fluid particle interfaces. i. stress-free conditions at the interfaces of micellar solutions of surfactants with fast sorption kinetics. *Physics of Fluids A: Fluid Dynamics*, 3(1):3–20, 1991.
- [96] Maartje LJ Steegmans, Anja Warmerdam, Karin GPH Schroen, and Remko M Boom. Dynamic interfacial tension measurements with microfluidic y-junctions. *Langmuir*, 25(17):9751–9758, 2009.
- [97] Patricia C Stepp, Kirk A Ranno, Erica D Dawson, Kathy L Rowlen, and Matthew M Ferris. Comparing h1n1 virus quantification with a unique flow cytometer and quantitative pcr. *Bioprocess I*, 9:50–56, 2011.
- [98] Wentao Su, Xinghua Gao, Lei Jiang, and Jianhua Qin. Microfluidic platform towards point-of-care diagnostics in infectious diseases. *Journal of Chromatography A*, 1377:13–26, 2015.
- [99] Xin Sun, Chunying Zhu, Taotao Fu, Youguang Ma, and Huai Z Li. Breakup dynamics of elastic droplet and stretching of polymeric filament in a t-junction. *Chemical Engineering Science*, 206:212–223, 2019.
- [100] Yung-Chieh Tan, Yao Li Ho, and Abraham Phillip Lee. Microfluidic sorting of droplets by size. *Microfluidics and Nanofluidics*, 4(4):343, 2008.
- [101] SW Tchikanda, RH Nilson, and SK Griffiths. Modeling of pressure and shear-driven flows in open rectangular microchannels. *International journal of heat and mass transfer*, 47(3):527–538, 2004.
- [102] Shia-Yen Teh, Robert Lin, Lung-Hsin Hung, and Abraham P Lee. Droplet microfluidics. *Lab on a Chip*, 8(2):198–220, 2008.

- [103] Christine M Thompson, Emma Petiot, Alexandre Lennaertz, Olivier Henry, and Amine A Kamen. Analytical technologies for influenza virus-like particle candidate vaccines: challenges and emerging approaches. *Virology journal*, 10(1):141, 2013.
- [104] Christine Marie Thompson. *Development of a Production Process for a Virus Like Particle Based Vaccine in Cell Culture*. PhD thesis, École Polytechnique de Montréal, 2013.
- [105] Todd Thorsen, Richard W Roberts, Frances H Arnold, and Stephen R Quake. Dynamic pattern formation in a vesicle-generating microfluidic device. *Physical review letters*, 86(18):4163, 2001.
- [106] Jihong Tong, Mitsutoshi Nakajima, Hiroshi Nabetani, and Yuji Kikuchi. Surfactant effect on production of monodispersed microspheres by microchannel emulsification method. *Journal of Surfactants and Detergents*, 3(3):285–293, 2000.
- [107] Simon Trowitzsch, Martin Klumpp, Ralf Thoma, Jean-Philippe Carralot, and Imre Berger. Light it up: highly efficient multigene delivery in mammalian cells. *Bioessays*, 33(12):946–955, 2011.
- [108] PB Umbanhowar, V Prasad, and David A Weitz. Monodisperse emulsion generation via drop break off in a coflowing stream. *Langmuir*, 16(2):347–351, 2000.
- [109] Volkert van Steijn, Chris R Kleijn, and Michiel T Kreutzer. Predictive model for the size of bubbles and droplets created in microfluidic t-junctions. *Lab on a Chip*, 10(19):2513–2518, 2010.
- [110] Siva A Vanapalli, Arun G Banpurkar, Dirk van den Ende, Michel HG Duits, and Frieder Mugele. Hydrodynamic resistance of single confined moving drops in rectangular microchannels. *Lab on a Chip*, 9(7):982–990, 2009.
- [111] K Wang, YC Lu, JH Xu, and GS Luo. Determination of dynamic interfacial tension and its effect on droplet formation in the t-shaped microdispersion process. *Langmuir*, 25(4):2153–2158, 2009.
- [112] Philip Wagli, Yu-Chi Chang, Kerstin Hans, Alexandra Homsy, Lubos Hvozدارa, Hans Peter Herzig, Markus Sigrist, and Nico F de Rooij. Correction to microfluidic droplet-based liquid–liquid extraction and on-chip ir-spectroscopy detection of cocaine in human saliva. *Analytical chemistry*, 86(3):1924–1924, 2014.

- [113] Jonathan D Wehking, Michael Gabany, Larry Chew, and Ranganathan Kumar. Effects of viscosity, interfacial tension, and flow geometry on droplet formation in a microfluidic t-junction. *Microfluidics and nanofluidics*, 16(3):441–453, 2014.
- [114] George M Whitesides. The origins and the future of microfluidics. *Nature*, 442(7101):368–373, 2006.
- [115] Harris Wong, CJ Radke, and S Morris. The motion of long bubbles in polygonal capillaries. part 2. drag, fluid pressure and fluid flow. *Journal of Fluid Mechanics*, 292:95–110, 1995.
- [116] Yvonne W Wu, Larry A Bauer, Roberta A Ballard, Donna M Ferriero, David V Glidden, Dennis E Mayock, Taeun Chang, David J Durand, Dongli Song, Sonia L Bonifacio, et al. Erythropoietin for neuroprotection in neonatal encephalopathy: safety and pharmacokinetics. *Pediatrics*, 130(4):683–691, 2012.
- [117] JH Xu, PF Dong, H Zhao, CP Tostado, and GS Luo. The dynamic effects of surfactants on droplet formation in coaxial microfluidic devices. *Langmuir*, 28(25):9250–9258, 2012.
- [118] Huidan Zhang, Shelley K Cockrell, Abimbola O Kolawole, Assaf Rotem, Adrian WR Serohijos, Connie B Chang, Ye Tao, Thomas S Mehoke, Yulong Han, Jeffrey S Lin, et al. Isolation and analysis of rare norovirus recombinants from coinfecting mice using drop-based microfluidics. *Journal of virology*, 89(15):7722–7734, 2015.
- [119] Qindan Zhang, Chunying Zhu, Wei Du, Cai Liu, Taotao Fu, Youguang Ma, and Huai Z Li. Formation dynamics of elastic droplets in a microfluidic t-junction. *Chemical Engineering Research and Design*, 139:188–196, 2018.
- [120] Rui-Qiao Zhang, Shao-Li Hong, Cong-Ying Wen, Dai-Wen Pang, and Zhi-Ling Zhang. Rapid detection and subtyping of multiple influenza viruses on a microfluidic chip integrated with controllable micro-magnetic field. *Biosensors and Bioelectronics*, 100:348–354, 2018.
- [121] Pingan Zhu, Tiantian Kong, Leyan Lei, Xiaowei Tian, Zhanxiao Kang, and Liquiu Wang. Droplet breakup in expansion-contraction microchannels. *Scientific reports*, 6:21527, 2016.
- [122] Pingan Zhu and Liquiu Wang. Passive and active droplet generation with microfluidics: a review. *Lab on a Chip*, 17(1):34–75, 2017.

- [123] Ying Zhu, Jay W Warrick, Kathryn Haubert, David J Beebe, and John Yin. Infection on a chip: a microscale platform for simple and sensitive cell-based virus assays. *Biomedical microdevices*, 11(3):565–570, 2009.

# APPENDICES

# Appendix A

## Image and Video Analysis Codes

### A.1 Extraction of Frames from Videos - Matlab Code

This code is for extracting frames from the videos.

```
v=VideoReader('at the junction 1.avi');
get(v);
nFrames=v.NumberOfFrames;
for img=1:nFrames
filename=strcat('frame',num2str(img),'.jpg');
b=read(v,img);
imwrite(b,filename);
end
```

### A.2 Converting Gray Scale Image into Binary Image - Matlab Code

This code is for turning each gray scale frame of droplet videos into binary for further analysis.

```
asd = VideoReader('V1.avi');
nFrames=asd.NumberOfFrames
firstframe=read(asd,1);
```

```

movLength = nFrames;
for i=1:movLength
K=read(asd,i);
median=medfilt2(K, [10 10]);
k=wiener2(median, [5 5]);
H = fspecial('unsharp');
sharp=imfilter(k,H,'replicate');
level = graythresh(median);
BWW = imbinarize(median,level);
bw2=1-BWW;
threshold=0.9;
edgemedian = edge(bw2, 'Canny', threshold);
binimagefill= imfill(edgemedian, 'holes');
subplot(1,9,8), imshow(binimagefill)
labeledImage = bwlabel(binimagefill, 4);
end
disp 'image labeling complete'

```

### A.3 Channel Height Calculation - Matlab Code

This code is used to calculate the channel height by using flow sensor data.

```

Vis10cst=10*(10-3);
Vis50cst=50*(10-3);
Vis100cst=100*(10-3);
W=100*(10-6);
Lc=10000*(10-6);
Lm=50000*(106);
Ltot=Lm+Lc;
Qc=1.86997E-11;
Pc=50000
H10=((Qc*12*Vis10cst*Ltot)/(Pc*W))1/3;
H10=H10*(106);
H50=((Qc*12*Vis50cst*Ltot)/(Pc*W))1/3;
H50=H50*(106);
H100=((Qc*12*Vis100cst*Ltot)/(Pc*W))1/3

```

$$H_{100} = H_{100} * (10^6);$$



# Appendix B

## Fluid Property Measurements

### B.1 Flow Sensor Calibration for Oil Viscosity Measurements

Inlet of the flow sensor was connected to the pressure system (Fluigent, Germany) and the output of the flow sensor was connected to the microfluidic chip. As the fluid flows inside the capillary channel of the flow sensor, flow rate of the fluid is measured by using thermal anemometry principles. Therefore, fluid property, for example, fluid viscosity, becomes an essential parameter for the sensor. If the thermal properties of the fluids change, the sensor must be calibrated. Since three different silicone oil were used in this study, calibration of each oil was required (see, Figure B.1). Sensor outputs as ‘tick counts’ (Figure B.1). To calculate the flow rate of the fluids while running an experiment, these tick counts were substitute into the calibration curve of each oil type (see Figure B.1).

### B.2 Viscosity Measurements of Red Blood Cells

To be able to design a microfluidic channel, it is essential to measure the properties of the target fluids. Specifically, viscosity and interfacial tension of fluids are needed to be known. In this study, silicone oil was mainly used as carrier oil where its viscosities are given by the producer, as shown in Table B.1. Red blood cells exhibit non-Newtonian fluid behavior and the viscosity of the red blood cell varies under the shear rate. The viscosity range of chicken red blood cells for a range of shear rates was adopted from the literature,

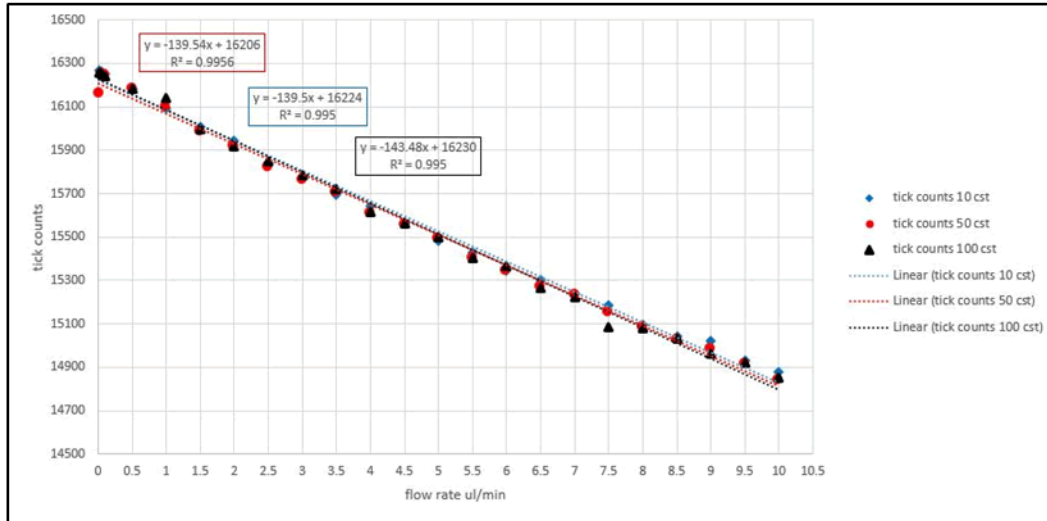


Figure B.1: Calibration curves of the flow sensor for three different silicone oil viscosities.

as shown in Figure B.1 [29]. Since the channel width of the microfluidic chip was used in Chapters 4 and 5 was  $100 \mu\text{m}$ , viscosities given in Figure B.2 was adopted from the plot where the channel width was  $102 \mu\text{m}$ .

Continuous Phase		Dispersed Phase	
Silicone Oil	Viscosity (mPa.s)	Chicken-Red Blood Cell Concentration	Effective Viscosity (mPa.s)
	100	100 %	~ 8-10
	50	45 %	~ 6-9
Interfacial Tension (mN/m)		15.117 ± 0.01	

Table B.1: Physical properties of the dispersed and the continuous phases.

### B.3 Interfacial Tension Measurement of Fluids

The equilibrium interfacial tension for red blood cell/silicone oil and virus stock/silicone oil combinations were measured using a Wilhemy plate Tensiometer (Data Physics, DCAT 11, Germany). Based on the measurements, the blood/oil interfacial tension was  $15.117 \text{ mN/m}$  and virus stock/oil was  $16.913 \text{ mN/m}$ .

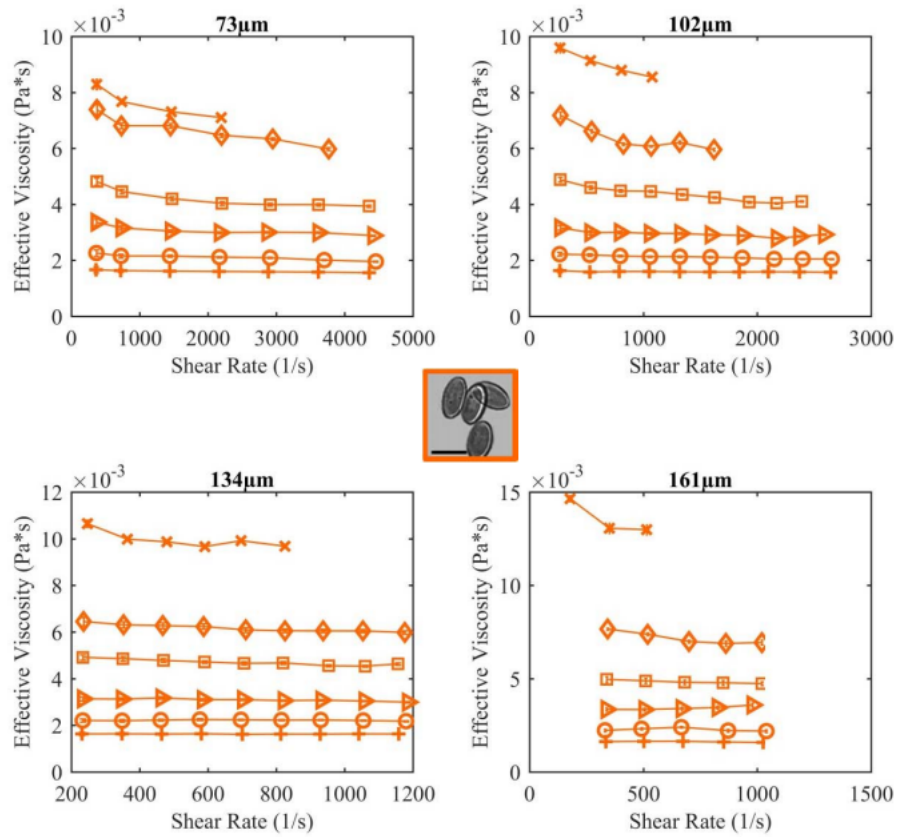


Figure B.2: Viscosity measurements of the chicken red blood cells for various cell concentrations under the range of shear rate from 1-3000 1/s in the microfluidic channels (cross, 100% RBC), (parallelogram, 45% RBC), (cube, 30% RBC), (triangle, 20% RBC), (circle, 10% RBC), (plus, Plasma) [29].